LBNL-47949
CBP Tech Note-231
LCC 0072

Oct. 2001

RF cavity R&D at LBNL for the NLC Damping Rings, FY2000/2001

R.A. Rimmer, D. Atkinson, J.N. Corlett, G. Koehler, D. Li,
N. Hartman, J. Rasson, T. Saleh, R. Weidenbach

LBNL, 1 Cyclotron Rd., Berkeley, CA 94720

Abstract

This report contains a summary of the R&D activities at LBNL on RF cavities for the NLC damping rings during fiscal years 2000/2001. This work is a continuation of the NLC RF system R&D of the previous year [1]. These activities include the further optimization and fine tuning of the RF cavity design for both efficiency and damping of higher-order modes (HOMs). The cavity wall surface heating and stresses were reduced at the same time as the HOM damping was improved over previous designs. Final frequency tuning was performed using the high frequency electromagnetic analysis capability in ANSYS. The mechanical design and fabrication methods have been developed with the goals of lower stresses, fewer parts and simpler assembly compared to previous designs. This should result in substantial cost savings. The cavity ancillary components including the RF window, coupling box, HOM loads, and tuners have been studied in more detail. Other cavity options are discussed which might be desirable to either further lower the HOM impedance or increase the stored energy for reduced transient response. Superconducting designs and the use of external "energy storage" cavities are discussed. A section is included in which the calculation method is sumarized and its accuracy assessed by comparisons with the laboratory measurements of the PEP-II cavity, including errors, and with the beam-sampled spectrum.

Contents

Introduction
1 Calculation of RF properties and HOMs
1.1 Frequency tuning
1.2 Coupling iris
1.3 Coupling waveguide options
1.4 Window placement
1.5 Summary of proposed NLC cavity RF design
2 Cavity thermal and stress analysis
2.1 ANSYS analysis
2.1 Internal vs. external cooling channels
3 Cavity fabrication and assembly
3.1 General fabrication approach
3.2 Assembly, mounting and installation
4 HOM waveguides and loads
5 Window and coupler
5.1 Window analysis in MAFIA
5.2 Cold-test measurements
5.3 Window analysis in ANSYS
5.4 Fabrication
5.5 First prototype tests
6 Tuners
6.1 Tuning range
6.2 Spring finger placement
6.3 Wall currents
7 Options and future work
7.1 Lower HOM options
7.2 Energy storage cavities
7.2.1 A simple 2-cavity model
7.2.2 Measurements on ALS third harmonic cavity
7.3 Superconducting option
7.4 Future work
8 Conclusions
9 References
Appendix A. Cost estimates of materials, fabrication, procurements and engineering.

Introduction

In order to provide the required accelerating voltage, momentum acceptance and stable beam at high currents the cavities for the NLC damping rings must have strong HOM damping, a high gradient and accomodate heavy beam loading. Table 1 shows some parameters of the damping ring and pre-damping ring RF systems, some of which have changed significantly since the previous report. The total voltage and beam power can be delivered by three copper cavities in each of the main damping rings but seven cavities are now required to produce the desired voltage in the positron pre-damping ring. The maximum bunch frequency is now the same as the RF frequency of 714 MHz, previously only every other bucket was filled giving a 357 MHz bunch rate. The power density and stresses in the NLC cavity are comparable to the current PEP-II operating conditions (taking the scaled PEP-II design as the baseline). Means of reducing the stress without sacrificing the good HOM damping properties and accelerating mode efficiency have been implemented. Simplifications of the mechanical design and fabrication have also been adopted.

The PEP-II RF cavity is among the first designs with strong damping of the higher order modes (HOMs), which are now seeing operation in the high-current e+ e- factories around the world [2,3]. This design has already proven to be very successful in the reduction of coupled-bunch instability growth rates, contributing to the rapid commissioning of the rings and the early attainment of high luminosity. The technology developed for PEP-II has already been put to further use for the 1.5 GHz ALS third harmonic cavity upgrade [4], and is a natural candidate for future projects such as light sources, storage ring based colliders and linear collider damping rings [5]. Many lessons learned during the design, manufacture and commissioning of these cavities were applied to the new design. The availability of better analysis tools and faster computers also now allows more detailed study of some aspects of the design.

Table 1. Damping ring RF parameters.

	Pre-damping ring	Damping ring
Energy	1.98	1.98 GeV
Circumference	218	299.8m
RF Frequency	714	714 MHz
Harmonic Number	520	714
Bunch Spacing	1.4 ns	1.4 ns
Beam Current	0.80 A	0.75 A
σ_ε	0.09	0.09 %
σ_z	7.2 mm	3.6 mm
α	0.00705	0.000295
$U_{s.r.}$	288 keV/turn	247 keV/turn
$U_{wiggler}$	273 keV/turn	530 keV/turn
$U_{HOM's}$	19.8 keV/turn	8.5 keV/turn
$U_{parasitic}$	17 keV/turn	17 keV/turn
V_{RF}	3.4 MV	1.07 MV
Number of Cavities	7	3
Number of Klystrons	1	1
Cavity Wall Dissipation	39.3 kW/cavity	22.4 kW/cavity
Beam Power	478 kW	602 kW
Klystron Power	1 MW	1 MW
Shunt Impedance	3.0 MΩ/cavity	3.0 MΩ/cavity
Unloaded Q	25500	25500
Coupling Factor	2.7	10
Synchronous Phase Angle	10°	48°
Synchrotron Frequency	43 kHz	3.5 kHz
Loaded Q	6846	2273
Energy Acceptance	± 1.5 %	± 1.5 %

1 Calculation of RF properties and HOMs

The method used to optimize the HOM damping involves a simulation in the time domain, in which the structure is excited by a short bunch passing through it, either on axis (for the longitudinal modes) or off axis (for the deflecting modes). The HOM waveguides, beam pipes and other openings are modelled with broadband absorbing boundary conditions. The long range wakefield is computed and recorded for many meters behind the bunch. This time record contains the amplitude of excitation and time constant of decay of all of the modes. A Fourier transform of this signal, normalized to the bunch spectrum, reveals the broad-band impedance spectrum of the cavity. The frequency resolution is determined by the length of the wakefield recorded, limited only by computer time and possibly by the onset of numerical instabilities in the simulation. Any mode still ringing with appreciable amplitude at the end of the recorded time will be truncated and artificially broadened in the spectrum, so care must be taken in interpreting the results.

In order to check the validity of these tools the PEP-II cavity geometry was modeled and the results compared with the known cavity properties [6]. There is good agreement between the simulation and measurement in the distribution, structure and relative amplitudes of the modes. Figure 1 shows the calculated impedance spectra using this method for the PEP-II geometry, including a simplified model of the coupler, compared with the values estimated from the measurements of the real cavity. Figure 2 shows the calculated HOM signals reaching the load and those measured in a cavity in PEP-II. The close correlation of these results between the calculated and measured mode strengths gives confidence in the broadband simulation method as a useful tool for optimizing the overall geometry.

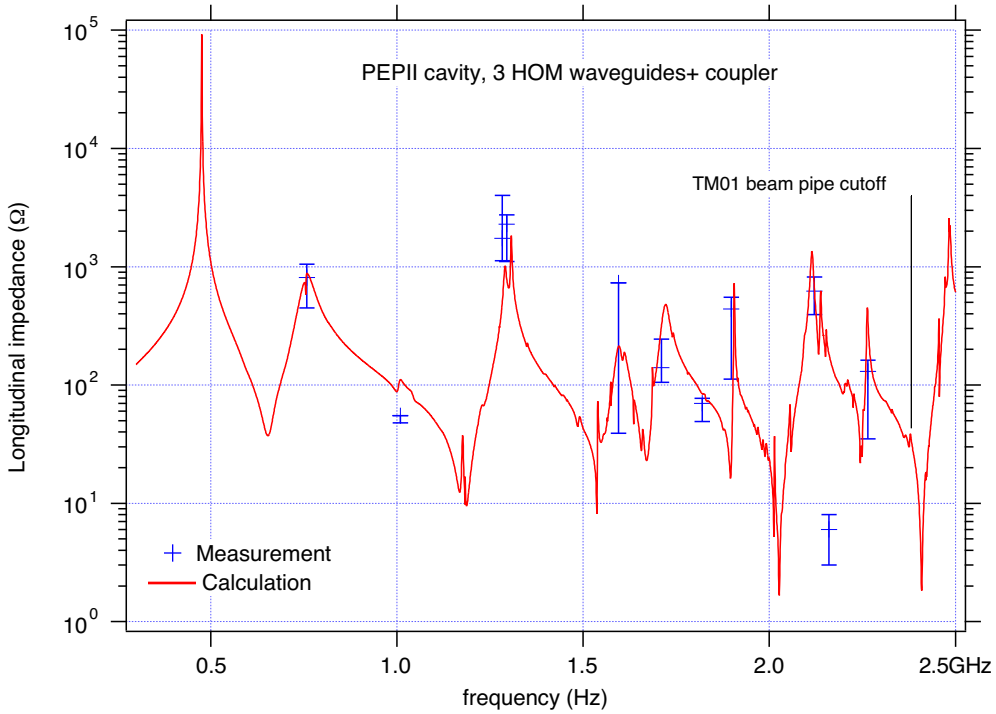

Figure 1. Calculated and measured impedance spectra of PEP-II cavity.

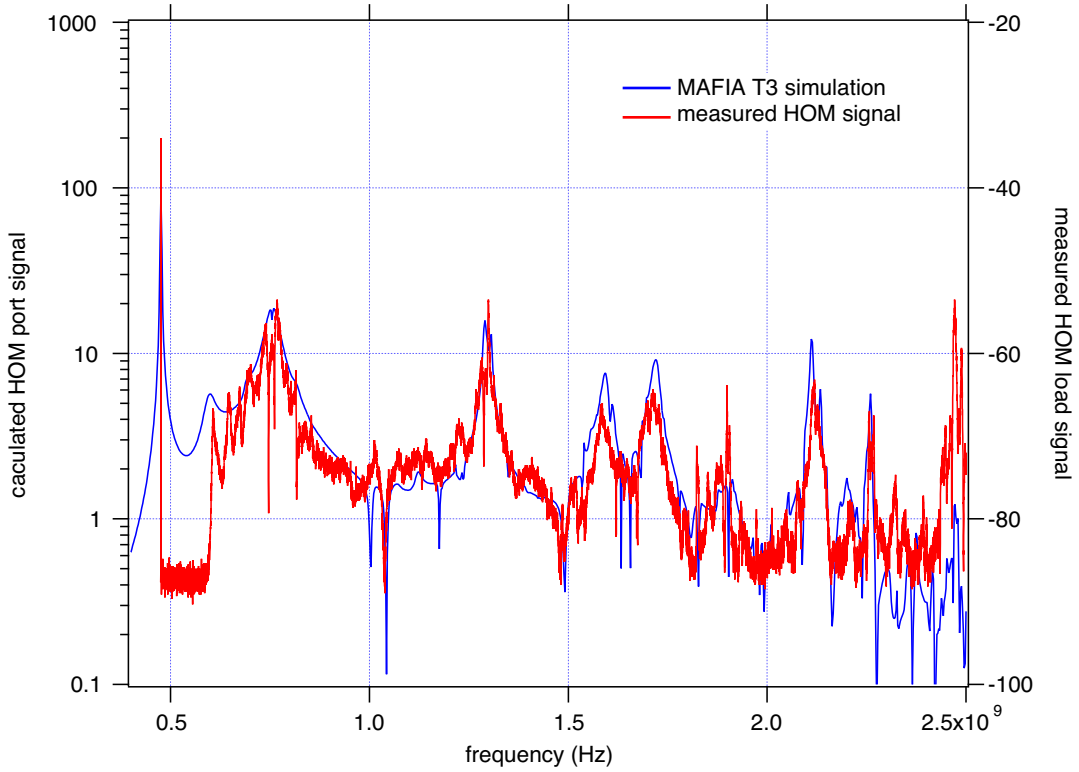

Figure 2. Calculated and measured signals reaching the HOM loads.

1.1 Frequency tuning

The cavity profile is changed very little from the previous version, being adjusted only to fine tune the frequency. The frequency in the MAFIA model was slightly off due to the addition of the various ports. Because of the relatively coarse mesh size in the 3D model and the rectangular brick approximation of the surface the frequency from MAFIA is not as accurate as from other methods. ANSYS was used to make the fine adjustments. Its finite element representation of the surface and variable element size should provide a better fit to the geometry and give a more accurate frequency. The frequency adjustment was performed iteratively. The cavity profile, i.e. the cross section of the axisymmetric part of the body, was scaled linearly according to the frequency error. However the HOM ports, tuner port and coupler were unchanged in their cross sections (though moved to keep their relative positions on the cavity walls). This was done to keep the cut-off frequencies of the HOM ports and coupler port fixed, but resulted in a small residual frequency offset after the first correction. A second scaling of the 2D profile brought the frequency within 1 MHz of the operating frequency, which is sufficiently accurate for this stage of the design. Table 2 shows the frequency perturbations from the various cavity ports calculated by MAFIA. The two tuners have a combined range of almost 2 MHz down in frequency (i.e. out of the cavity), and at least as much upwards in frequency (i.e. moving into the cavity). Addition of the tuner ports has very little effect on the shunt impedance or Q of the cavity. The largest perturbation to the frequency and shunt impedance comes from the three HOM waveguides. These drop the frequency by 2.4% and the Q by about 14%. The R/Q changes very little so the shunt impedance is also lowered by 14%. The next largest perturbation is from the coupling port which lowers the frequency about 1.6% and the shunt impedance by about 9%. Note that the shunt impedance of the full cavity configuration is perturbed by less than the sum of the individual perturbations (19% vs. 23.5%). This is because the larger apertures tend to disrupt the fields and currents over a significant area and the placement of another port in an area with already depleted field has less effect.

On the real cavity a mechanical tuning operation will be included before final welding. The nosecones will be left oversize until the cavity is nearly finished and will then be tuned to give the correct frequency by removing an appropriate amount of material. The uncertainty in the frequency from the ANSYS calculations is well within range of the mechanical tuning.

Table 2. Perturbations from various ports in MAFIA (before tuning).

	Freq. (MHz)	Δ f (MHz)	Rs (MΩ)	Δ Rs (%)	Qo	Δ Q (%)	R/Q (Ω)	ΔR/Q (%)
bare cavity	738.049		4.629		39026		118.6	
2 tuner ports*	736.186	-1.863	4.620	-0.2	38935	-0.2	118.7	0.0
coupling port	733.173	-4.876	4.202	-9.2	35872	-8.1	117.1	-1.2
3 HOM ports	725.954	-12.095	3.975	-14.1	33672	-13.7	118.1	-0.5
full cavity	720.273	-17.776	3.750	-19.0	31976	-18.1	117.3	-1.1

* both tuner ports included with tuners fully out

1.2 Coupling iris

The previous version of the NLC cavity design used a scaled version of the PEP-II type coupling slot, figure 3a. Further studies have shown that it is not possible to achieve the desired coupling factor without having either a very short or very wide iris. In the first case it becomes difficult to include a flange pair in the length of the iris (useful to allow the coupling box to be demountable), in the second case the flange has to be rather large to accomodate the wide slot. A simple remedy is to use the same slightly ridged "dumbbell" cross section as the HOM ports, figure 3b. This has a lower cut-off frequency than the simple slot for a given width so the port can be acceptably long and sufficiently narrow. This option has the added bonus that the coupling port flanges are identical to the HOM port flanges, eliminating several parts and drawings.

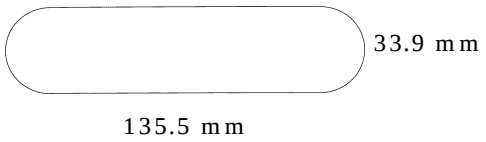

Figure 3a. Scaled PEP-II coupler.

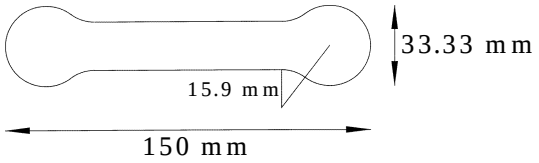

Figure 3b. "Dumbbell" coupler.

1.3 Coupling waveguide options

The feed waveguide can be magnetically coupled to the cavity in two ways, either through the end wall like PEP-II or through the side wall like the ALS. Depending on the ratio of operating frequency to waveguide cut-off frequency one or other of these may have stronger coupling for a given aperture size. At 714 MHz in WR1500 the end coupling is slightly stronger, because the transverse magnetic field at the end wall is stronger than the longitudinal field at the side wall. Either end- or side-wall coupling could be used for the NLC damping ring cavities with appropriate adjustment of the

length of the coupling iris, however note that with a simple scaled PEP-II type slot coupler the iris must be impractically short to reach the new maximum desired coupling factor of 10, see figure 4.

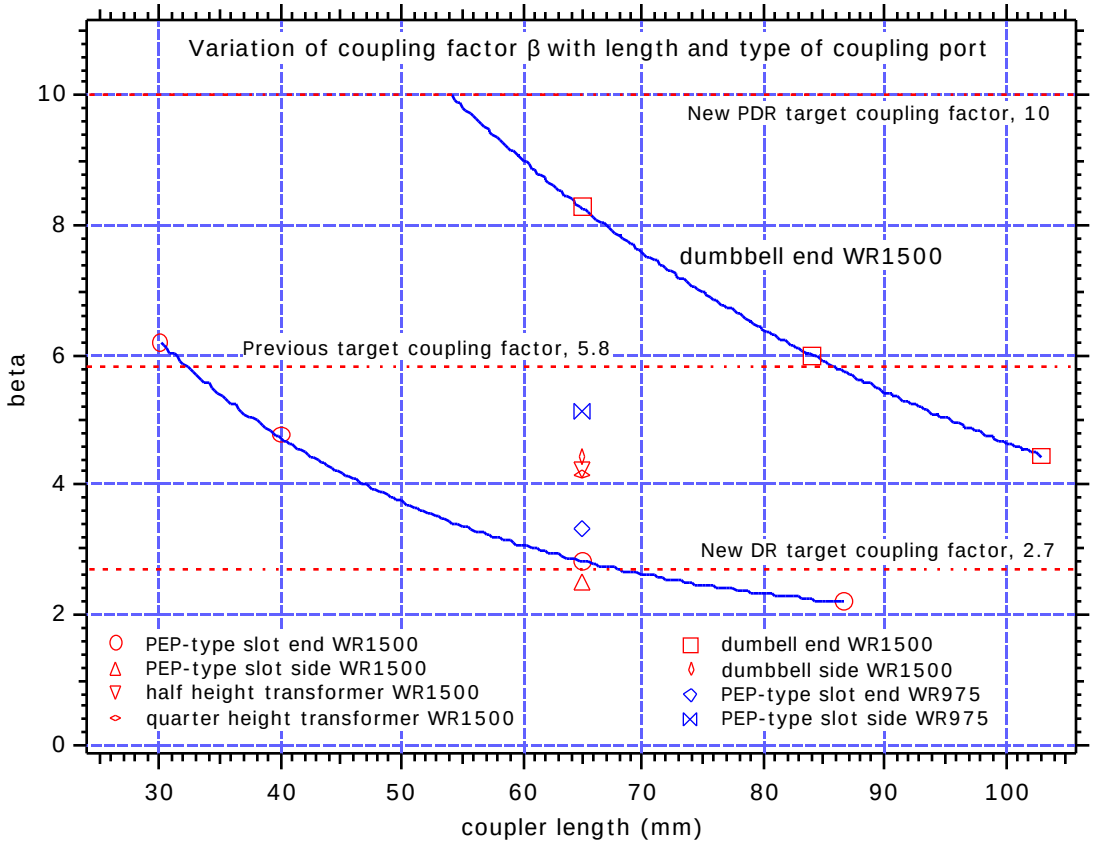

Figure 4. Variation of coupling factor for different irises and lengths.

Various waveguide transformers and switching to WR975 waveguide were tried in order to increase the coupling at the previous nominal length (65mm) but none brought the coupling up to the desired value. Simply changing the iris cross section to the same dumbell profile as the HOM ports, which has a lower cutoff frequency, gave a dramatic increase in coupling, allowing the original target value of 5.8 to be achieved with an 85 mm long iris. The new maximum coupling factor (10) can be achieved with an iris length of approximately 54.2 mm.

Note that in the most recent configuration the two rings are substantially different with the main damping rings having a lower coupling factor (2.7) and the pre-damping ring needing a higher coupling factor (10). This is a result of the different voltage requirements and number of cavities in the two types of rings. The same hardware configuration might still be used for both rings with the addition of a matching stub to adjust the coupling over a suitable

range. Even higher coupling is possible using the new coupler with WR 975 waveguide.

In the case of the PEP-II type coupler a 90° bend in the waveguide is included to eliminate line-of-sight from the beam to the window. In PEP-II this was also required to route the waveguide down the tunnel to the nearest penetration from the surface building. This type of waveguide layout with a 90° bend is again proposed for the NLC damping rings and has been studied in some detail.

The feeder waveguide and window assembly must be matched at the operating frequency of 714 MHz. The window assembly is designed to be self-matched without the need for posts or irises. The 90° waveguide bend can be matched by adjusting the dimensions of the mitre. The window is not well matched at HOM frequencies however, and some HOM power will be extracted from the cavity through the coupling iris. In order for this to be reasonably well absorbed an additional HOM load is added to the coupling box. Again following the practice of PEP-II this is placed on the mitre of the waveguide bend and takes the form of a smaller waveguide that is below cut-off at 714 MHz (f_c=900 MHz), and is terminated in a planar load of ferrite or resistive tiles. It was not possible to completely match the combined bend and HOM load assembly at 714 MHz by only adjusting the mitre offset, so small inductive irises were added in the waveguide to match the remaining reactive component. Figure 5 shows the variation of the reflection and transmission coefficients with mitre offset without the use of matching irises. Note that the minimum reflection coefficient is not quite zero. (Sbal is a parameter in the MAFIA simulation that indicates the energy balance between incoming and outgoing waves and should equal unity for a good simulation result). Figure 6 shows how the match can be improved by a 3 cm x 2 cm capacitive matching bar on one side of the waveguide at various positions. In practice it is more convenient to use inductive matching elements closer to the bend, see figure 7. Figures 8 and 9 show the transmission and reflection coefficients of the bend with HOM load and inductive irises as a function of frequency. The match is optimised at 714 MHz. Above about 780 MHz the waveguide becomes overmoded and some mode conversion into higher modes takes place. Figure 10 shows the transmission to the HOM load. There is quite strong coupling at higher frequencies into several propagating modes. The exact coupling strength will be different when the window is included since it will reflect some of the high frequency power which in this

model propagates away in the waveguide. However since this is an auxiliary HOM load an exact match is not required.

The match at the operating frequency of 714 MHz has been roughly optimized in MAFIA. The exact size and position of the irises will be fine tuned by cold-tests before the coupling boxes are put into production. The full MAFIA model is shown in figure 11

The coupling box will be a welded sheet metal construction with a flange for the window on one end and a circular flange to mate to the cavity coupling iris on the other end. The inside surfaces will be copper plated for low RF losses and water cooling may be used in some places, such as the matching irises or bend if necessary. The HOM waveguide will be joined to the mitre bend and the load material will be attached to the end using a weld eyelet such that it may be detached for repair if necessary.

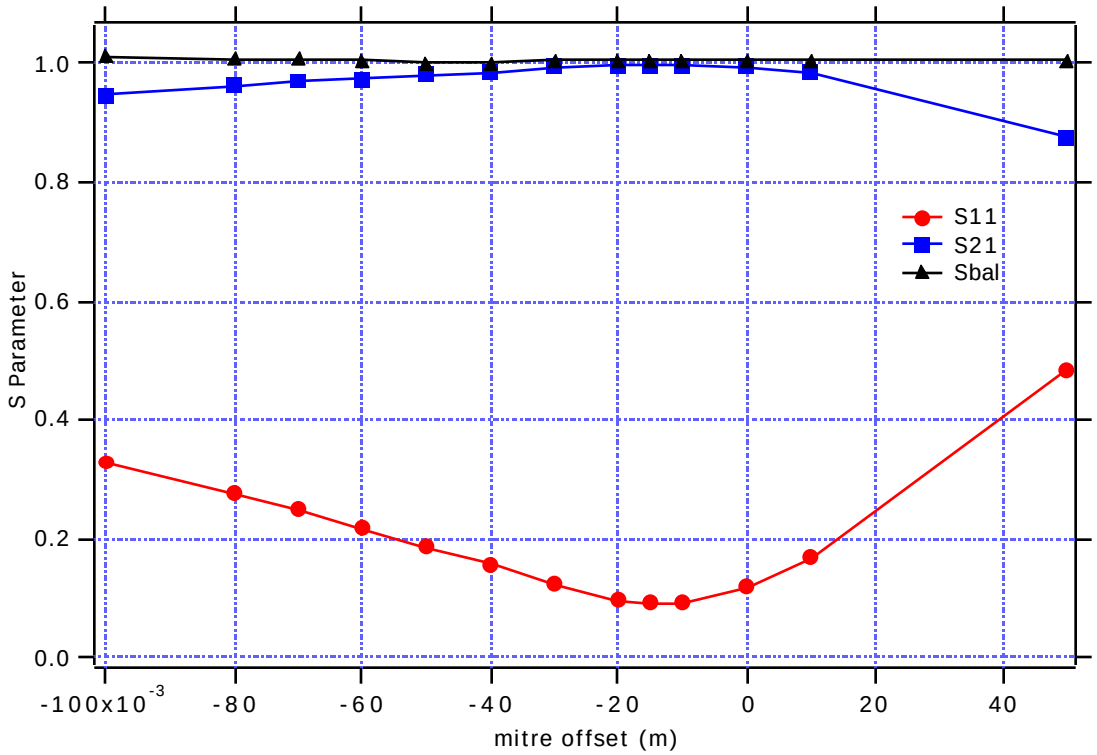

Figure 5. Reflection and transmission coefficients at 714 MHz of bend plus HOM load as a function of mitre offset (0 offset = full 45° mitre).

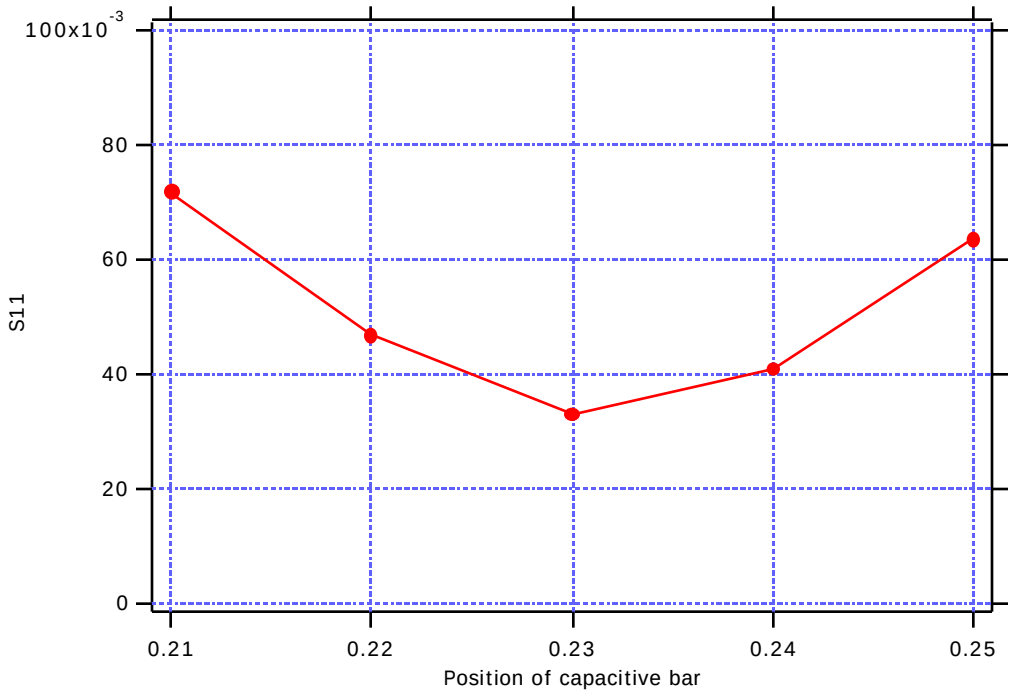

Figure 6. Match vs position of a 3 cm x 2 cm capacitive bar in waveguide. Note that the match could be further fine tuned by adjusting the dimensions of the bar but this was limited by the mesh resolution in this MAFIA model.

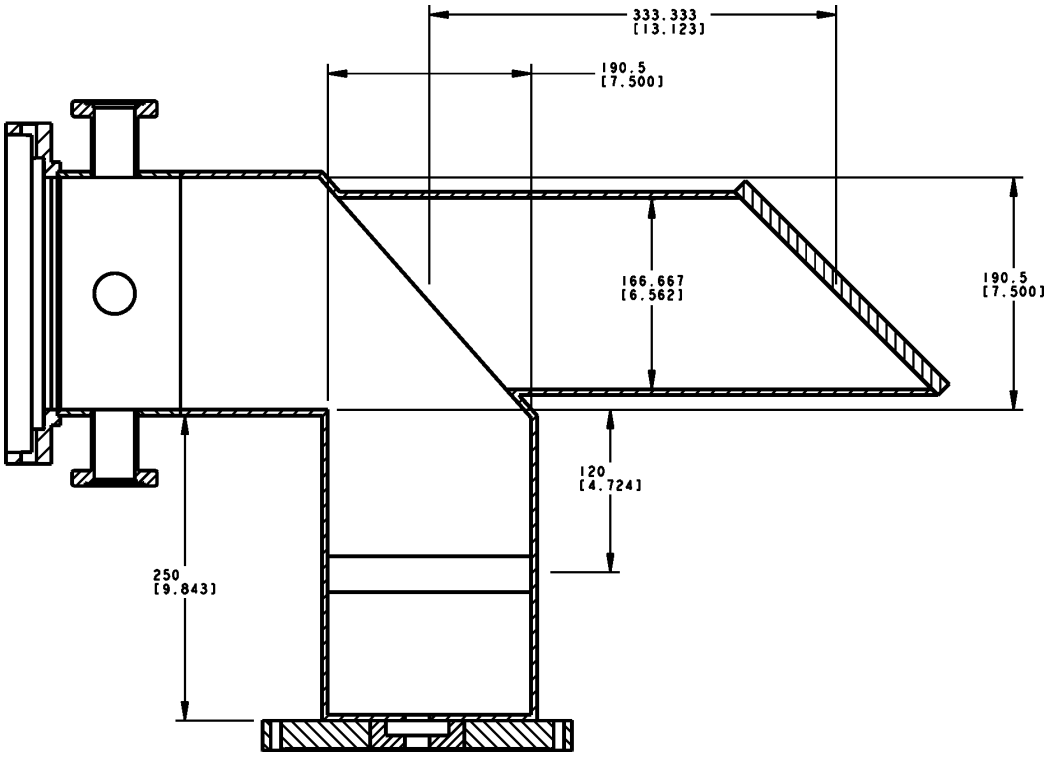

Figure 7. Coupling box dimensions.

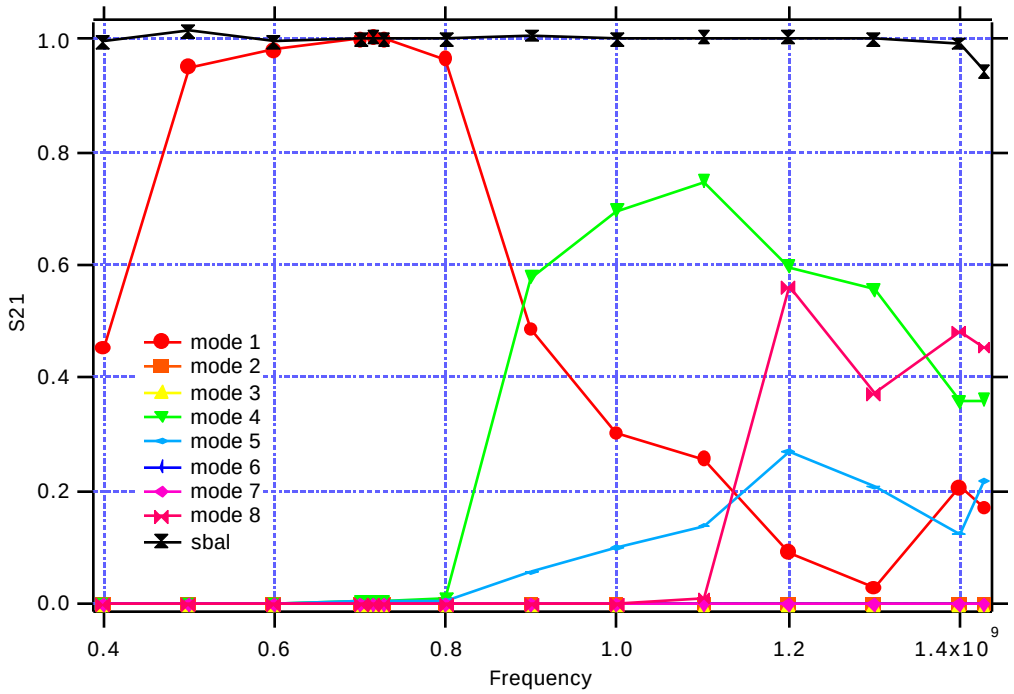

Figure 8. Transmission through coupler bend + HOM load and irises. Note that the WR1500 waveguide becomes overmoded at 787.4 MHz and there is some mode conversion into higher modes.

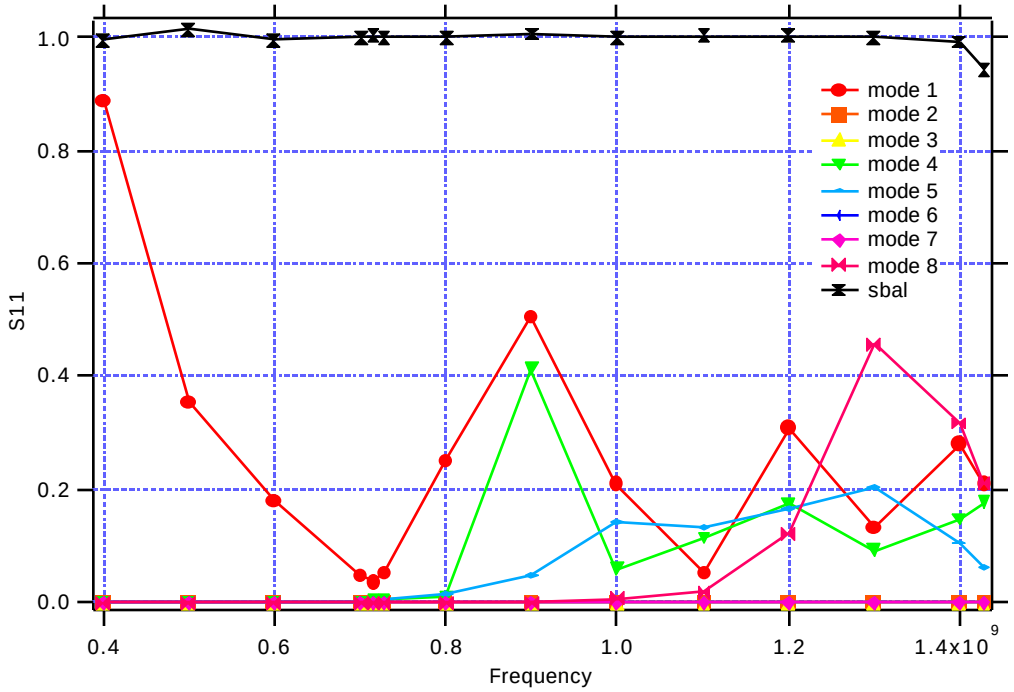

Figure 9. Reflection coefficient of coupler box with bend, HOM load and inductive irises. Model is excited in mode 1 and minimum reflection coefficient is about 714 MHz. Above 787.4 MHz there is some mode conversion into higher modes.

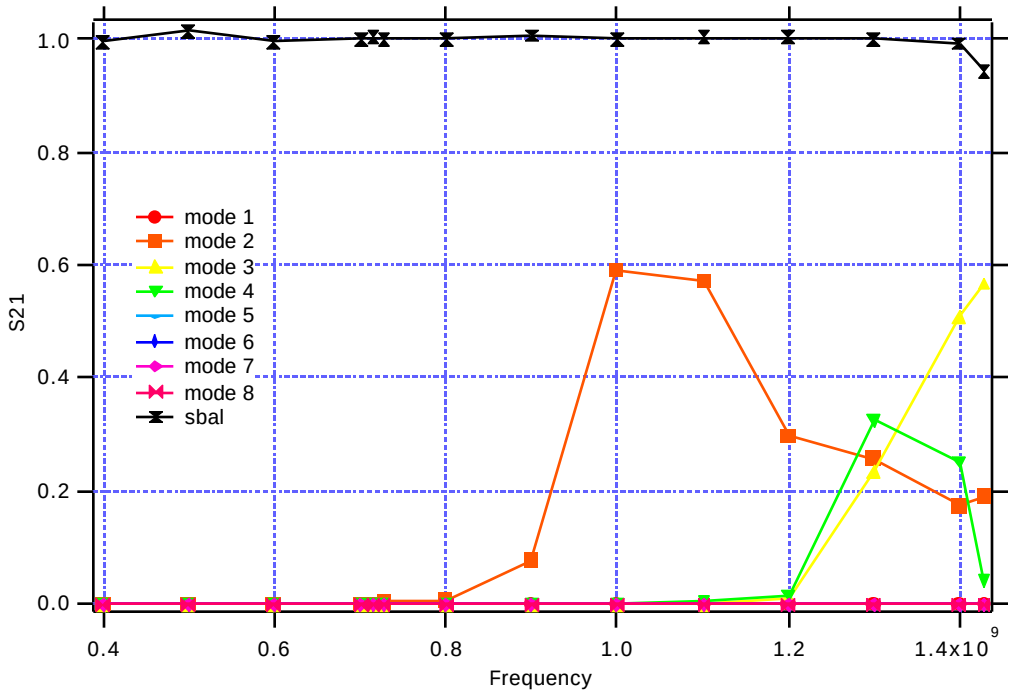

Figure 10. Transmission to HOM load. There is quite strong coupling into the HOM waveguide fundamental mode above 900 MHz. The HOM waveguide becomes overmoded above 1273 MHz.

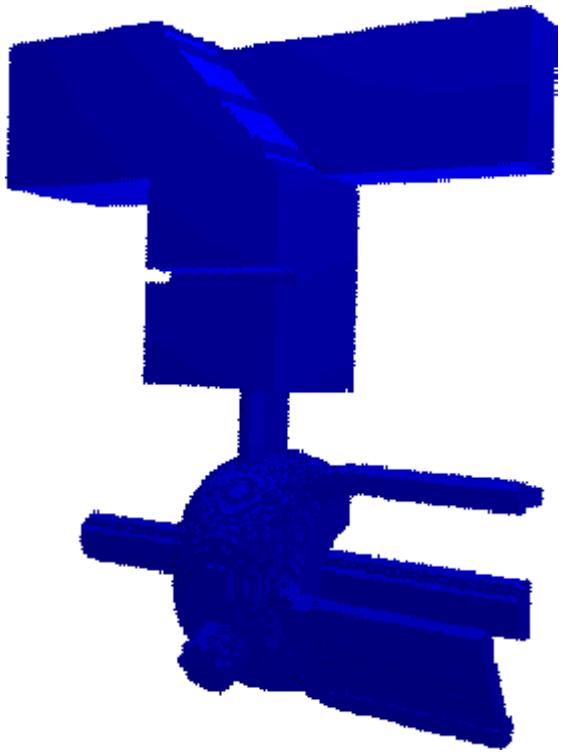

Figure 11 MAFIA model of cavity plus HOM waveguides and coupler.

1.4 Window placement

The position of the window in the feeder waveguide is important in terms of expected reliability. As in PEP-II it is proposed to locate the window at a detuned-short position away from the coupling iris. In this location the electric field is fixed relative to that in the cavity regardless of beam loading. This has the advantage that the voltage across the window and power loss in the ceramic and window coating are fairly constant and don't undergo large transients after a sudden beam loss. This is thought to be helpful for window reliability and long operational life. It is also believed to be advantageous for there to be no line of sight from the beam to the ceramic window because of the possibility of scattered particles or radiation from the beam reaching the ceramic, so it is proposed to place the window around a 90° bend in the waveguide. The window is also placed vertically to minimize the possibility of dust or debris settling on the ceramic, which might cause sparking. Arc detector ports will be included to monitor both sides of the window for visible light indicating an arc or multipactoring. The arc detectors will probably be remotely sited, coupled to the waveguides by optical fibers, and shielded in order to minimize the number of false trips due to radiation from the beam.

The detuned-short position was determined by running a MAFIA model with the cavity off frequency and with the waveguide input excited in the fundamental mode. The resulting standing wave in the coupler box has zeros in the electric field at the detuned-short positions. Figure 12 shows a two dimensional slice through the 3D MAFIA model. The input waveguide is at the top left while the HOM waveguide exits to the right. Lower in the picture the coupling iris joins the waveguide to the cavity. Two reversals are visible in the electric field, one in the input waveguide and one in the mitre bend. The former is a suitable place for the window. Figure 13 shows a 1D plot of the electric field along a line down the center of the input waveguide all the way to the end of the HOM load. The zero in the waveguide electric field is located at z=-20cm (i.e.: 20 cm from the cavity center towards the klystron).

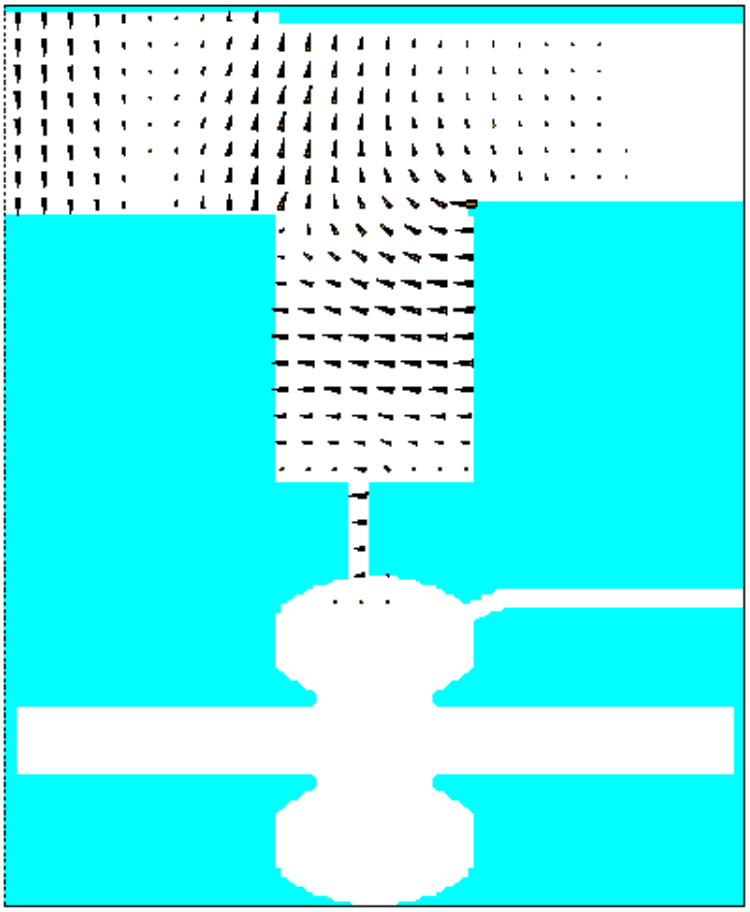

Figure 12. 2D plot of the electric field of the standing wave in the coupler with the cavity detuned, waveguide driven (top left).

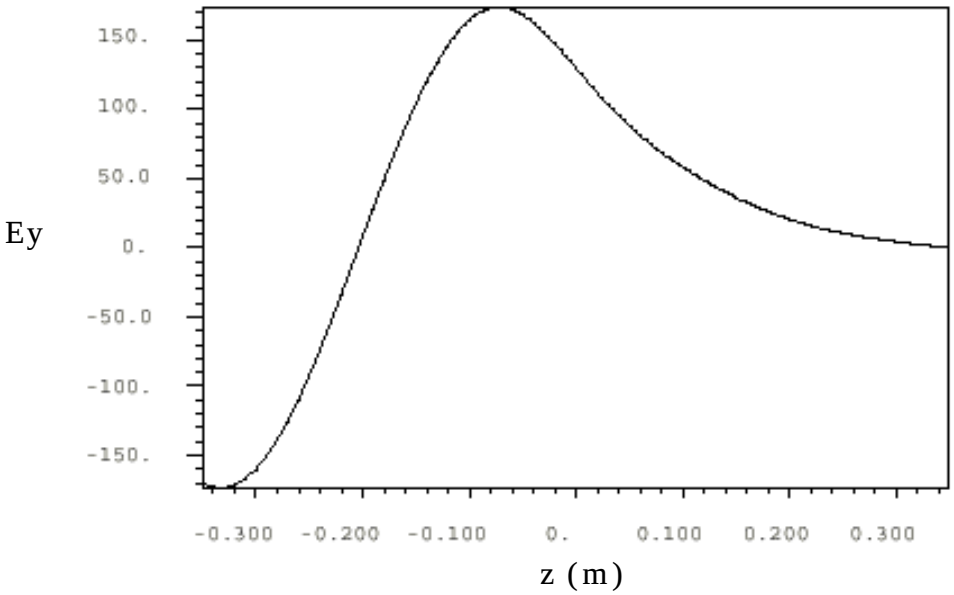

Figure 13. Ey vs z along waveguide (top of figure X) at y=0.601m (input to left, HOM load to right).

1.5 Summary of proposed NLC cavity RF design

The proposed NLC damping ring cavity, see figure 14, bears a strong resemblance to the PEP-II cavity on which it is based. Modifications to the shape have been made to improve the HOM damping, lower the mechanical stresses and simplify the construction. The cavity body has been adapted from the traditional toroid to a shape with a spherical mid section and a generous blend to the end wall. Simulations of many combinations show that a profile with spherical section ±30° from the mid-plane and a blend radius of ~39 mm to the end wall has a good distribution of HOMs, a high shunt impedance and fits well with proposed fabrication methods.

The nosecone angle has been studied with regard to the effect on HOM damping and the 30° angle chosen for PEP-II was found to be about optimum and will be used again. The beam pipe radius at the cavity is chosen to be in approximately the same proportion to the cavity as for PEP-II. Reducing the diameter would increase the shunt impedance but would also increase the transverse loss parameter which is thought to be unacceptable.

The HOM waveguides have a slightly ridged "dumbbell" profile which gives a smaller width for the desired cutoff frequency and a large radius at the ends of the slots. This, combined with a generous blend into the cavity wall, results in significantly lower peak currents, temperatures and stresses than the PEP-II shape. The position of the HOM ports on the cavity body has been extensively studied and the optimum location has the waveguides exiting at a 30° angle to the beam axis, normal to the surface on the 39 mm blend part of the profile. A dumbell-shaped port is used to couple to the main waveguide, which gives significantly more coupling than the simple PEP-type slot. The coupler is offset from the mid-plane to give some additional coupling to the antisymmetric modes (which have no magnetic field on the mid-plane for the simple cavity). A circular coupler could be used but with reduced coupling and some penalty to the strongest remaining HOMs.

Table 3 gives some of the relevant parameters for this profile. For comparison the parameters of the 3D MAFIA model are shown, including the HOM damping waveguides, coupler and tuner ports. The Q is about 14% lower than a MAFIA calculation with no apertures, which is part of the 70% factor applied to the 2D calculation (the factor commonly applied to the MAFIA result is ~80%). We used the more conservative estimate (3.0 MΩ, 41.7 kW),

for the thermal and stress analysis. Note also that because the 3D mesh is coarser and uses bricks instead of triangles the peak electric field on the surface is not as well resolved. The frequency of the 3D model is lower because of the extra volume of the apertures. The present parameters for the damping rings and positron pre-damping ring are shown in table 4. Tables 5 and 6 show the modes below cut-off for the simple 2D cavity shape, calculated by URMEL, and the estimates of the strengths of the remaining modes in the 3D damped cavity with coupler, calculated by MAFIA in the time domain (including five peaks above cut-off).

Figure 15 shows how the longitudinal coupled bunch instability threshold varies with frequency. The cavity impedance is within acceptable limits for the damping rings even without longitudinal feedback. For the present pre-damping ring parameters however, there are a few peaks are above threshold. Stability could be maintained by using a feedback system, increasing the number of HOM ports on the cavities or using superconducting cavities. The dipole mode spectrum is better than the PEP-II design but still above the threshold for transverse coupled-bunch instabilities, see figure 16, however the growth rates are small compared to the resistive wall modes [7]. The beam can be stabilized with a transverse feedback system which will be needed to suppress resistive wall modes and those driven by ion effects, electron clouds, etc.

The approximate thresholds are calculated assuming a single resonant impedance driving each coupled-bunch mode. If the growth rate is equal to the damping rate then:

$$Z_{thresh} = \frac{2.E.Q_s}{I.\alpha.\tau_d}.\frac{1}{f}, \quad Q_s = \frac{f_s}{f_{rev}}$$

where E is the energy (in eV), α is the momentum compaction factor, f_s is the synchrotron frequency, f_{rev} is the revolution (orbit) frequency, τ_d is the longitudinal damping time. Similarly the approximate transverse threshold is:

$$Z_{thresh} = \frac{2.E.}{I.f_{rev}.\beta.\tau_d}$$

where β is the beta function at the cavity (assumed ~10 m), and τ_d is the transverse damping time (both of which may be different for x and y planes). In practice the real aliased impedance spectrum and details of the bunch filling pattern are important.

The cavity will have two tuner ports, one of which will have a motorized tuner to dynamically compensate for beam loading and

temperature changes. The other will be a fixed plunger which will be adjusted to fine tune the cavity frequency after fabrication. The proposed design has three small ports, one opposite each tuner and one opposite the coupler. One of these will be used for the RF pickup loop (most likely the one opposite the coupler), while the other two may house an arc detector or a viewport so that a TV camera can be used to observe the tuners during cavity conditioning. This is very useful, especially if spring fingers are incorporated in the tuner design, as the TV camera can be used to monitor them remotely to watch for sparking.

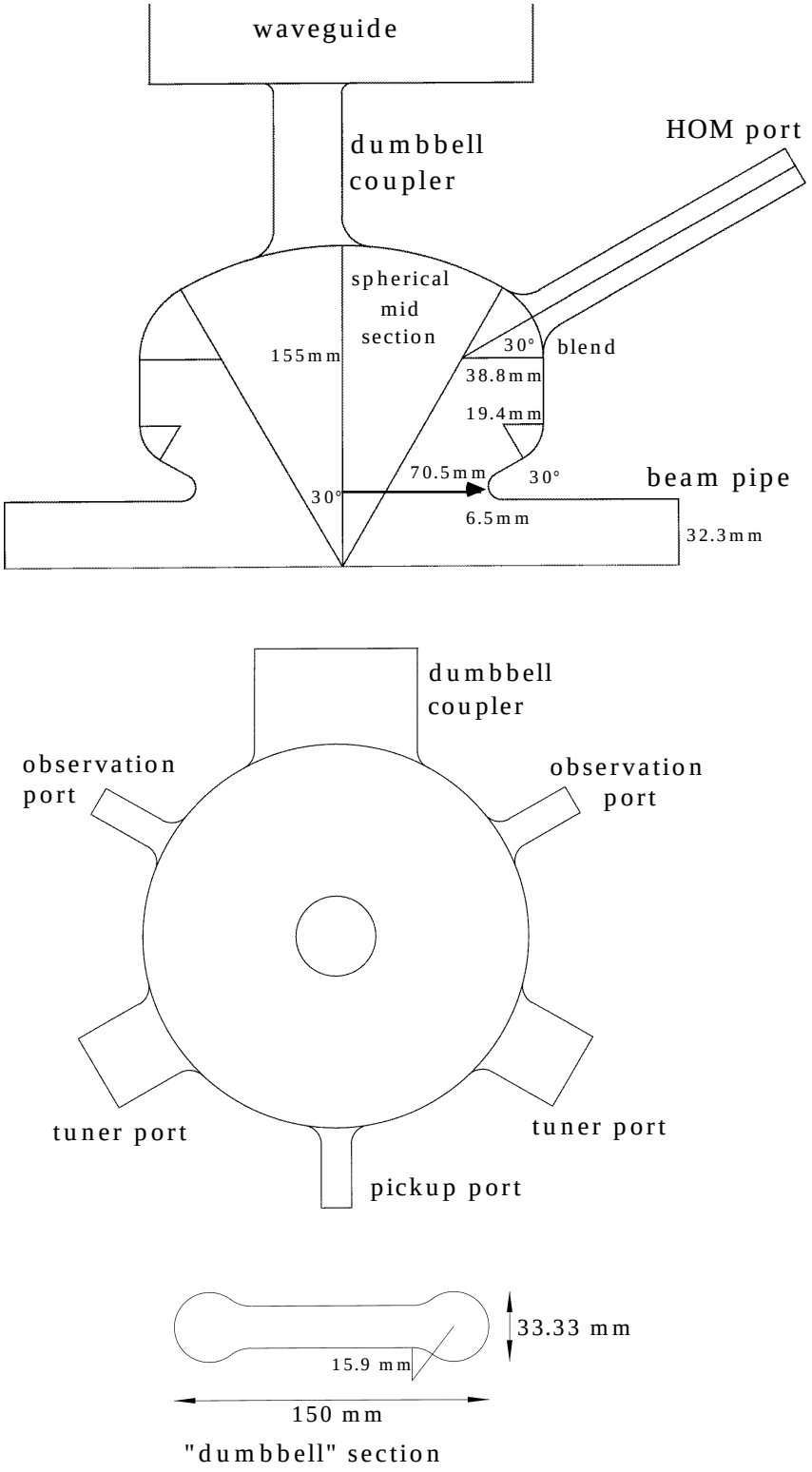

Figure 14. Proposed NLC cavity geometry.

Table 3. Basic parameters for profile 714q.

parameter	2D (URMEL)	3D (MAFIA)
RF frequency, MHz	714	704*
R/Q, Ω	118	117
Qo	36182	34609
Rs (V^2/2P), MΩ	4.27	4.064
Est. attainable Rs, MΩ	3.0 (70%)	3.25 (80%)
Voltage, kV	486	486
Power (est), kW	39.3	36.3
Pk surf. E field,MV/m	9.15	7.86
Kilpatric, MV/m	25	25

* no tuners

Table 4. Damping and pre-damping ring parameters.

parameter	Damping ring	Pre-damping ring
RF frequency	714 MHz	714 MHz
Current	750 mA	800 mA
Energy	1.98 GeV	1.98 GeV
fo	1.013 MHz	1.373 MHz
fs	3.6kHz	43 kHz
alpha	2.94e-4	7.05e-3
trans. damp. time	5.03 ms	5.13 ms
energy damp. time	2.5 ms	2.5 ms
threshold Zlong	~2.5e13/f Ω	~0.76e13/f Ω
threshold Ztrans	~100 kΩ/m*	~70 kΩ/m*
# cavities	3	7

* assume β ~10 m

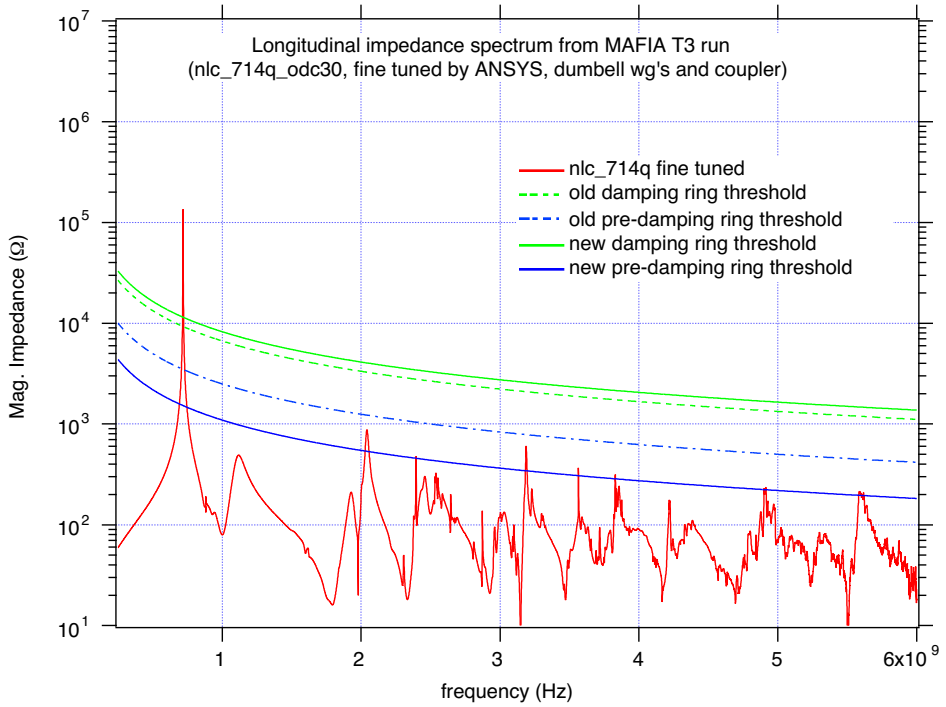

Figure 15a. Longitudinal impedance spectrum with thresholds (3 cavs DR, 7 cavs PDR, 400m calculated wake sigma=3cm).

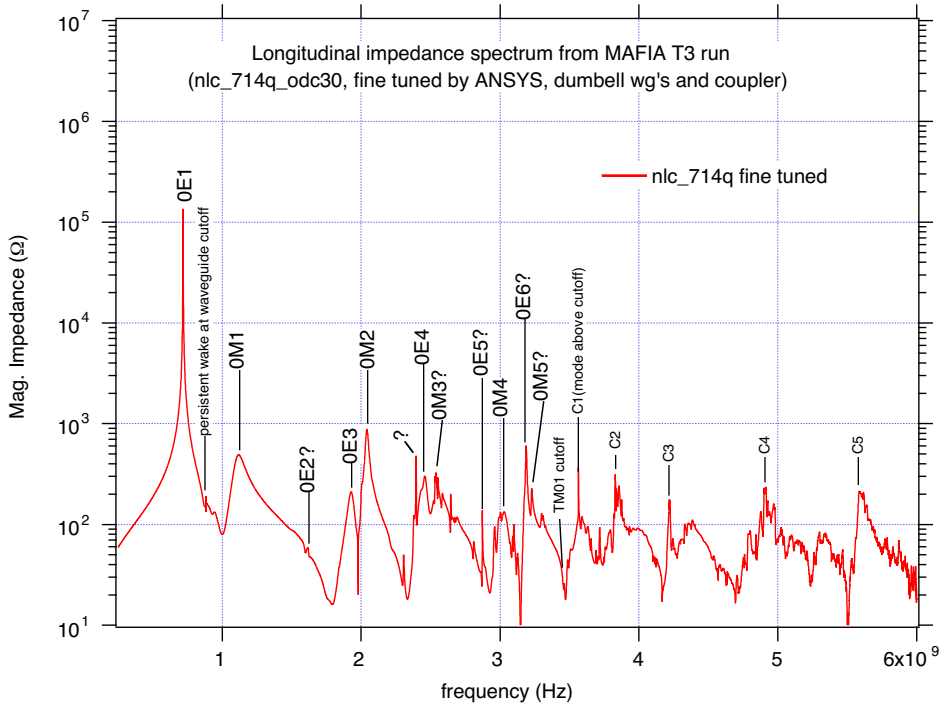

Figure 15b. Longitudinal spectrum labeled with 2D modes (400m wake sigma=3cm).

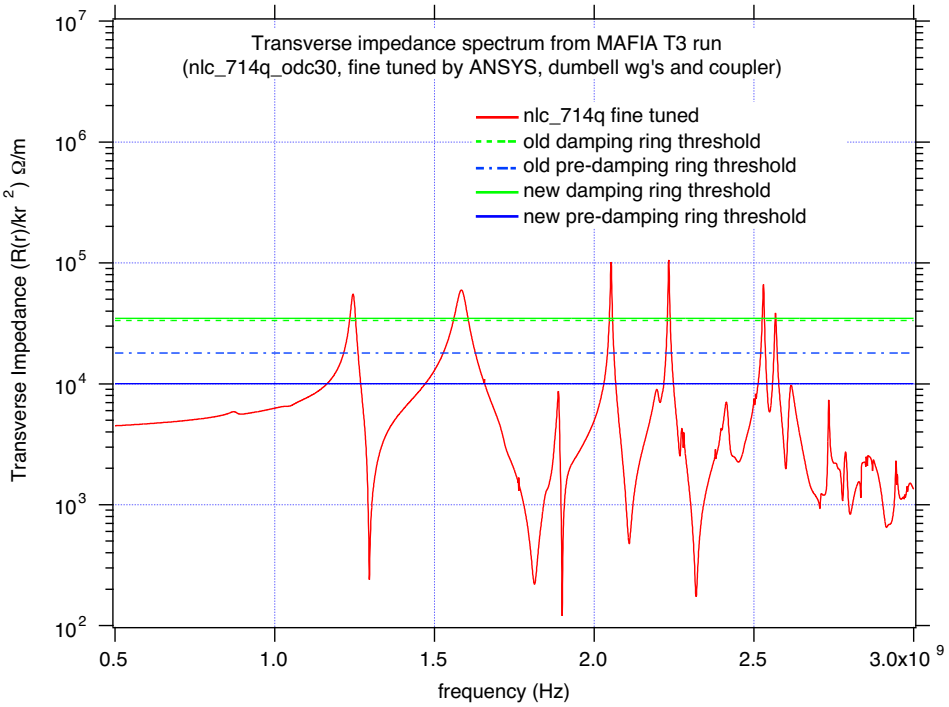

Figure 16a. Transverse impedance spectrum with thresholds (3 cavs DR, 7 cavs PDR, 400m calculated wake sigma=3cm).

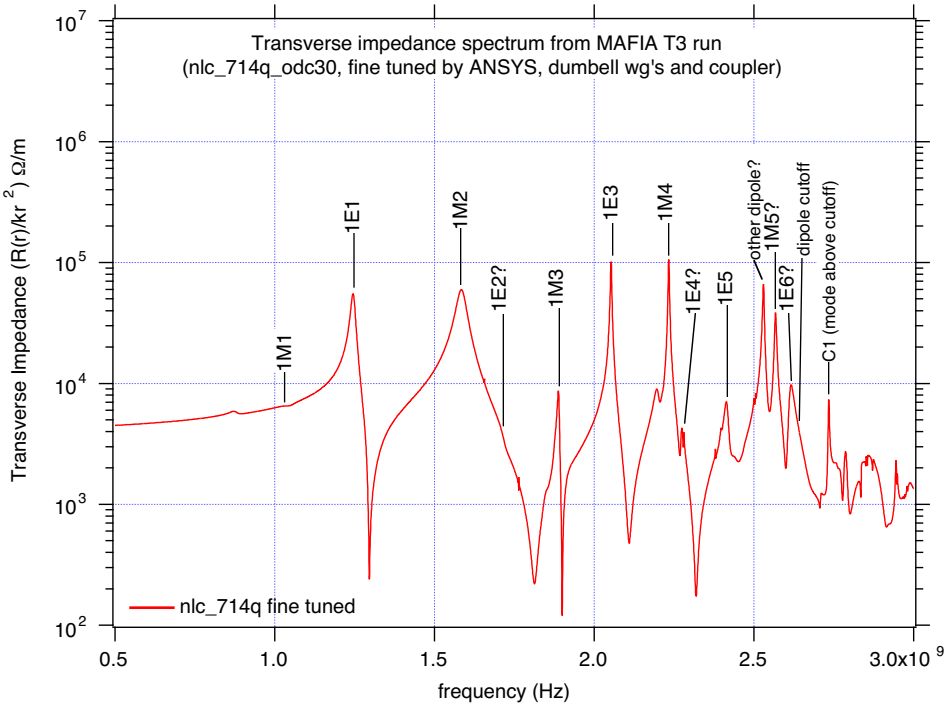

Figure 16b. Transverse spectrum labeled with 2D modes (400m wake sigma=3cm).

Table 5. Calculated monopole HOMs , 2D and 3D.

mode type	Freq. 2D	R/Q 2D	Qo 2D	Rs †2D	MAFIA T3*	MAFIA T3
(URMEL)	(MHz)	(Ω)		MΩ	freq.(MHz)	Rs damp(Ω)
0-E-1	736††	117.69	35539	4.1825	716	3.0e6‡
Pers.					883	184
0-M-1	1102	34.52	30113	1.0394	1118	491
0-E-2	1620	0.09	33513	0.0029	1616	58.9
0-E-3	1909	4.56	72518	0.3305	1928	210
0-M-2	2026	8.48	33224	0.2816	2042	876
new?					2396	476
0-E-4	2474	6.28	33221	0.2085	2459	303
0-M-3	2502	4.39	54939	0.2413	2538	326
0-E-5	2827	0.11	102257	0.0111	2873	136
0-M-4	3007	2.06	35018	0.0721	3030	134
0-E-6	3166	3.77	52321	0.1970	3189	604
0-M-5	3198	0.003	80997	0.0002	3228	227
C1**					3565	366
C2**					3830	315
C3**					4222	174
C4**					4914	235
C5**					5586	214

TM_{01} cutoff 3446 MHz, †Rs=$V^2/2P$, *model nlc_714q_odc30, ††2D model using profile of tuned 3D model from ANSYS. ‡estimate based on frequency domain calculation and realistic loss of Q. ** peaks above cut-off.
Note that the 2D frequency is high because the model uses the dimensions of the 3D cavity tuned in ANSYS.

Table 6. Calculated dipole HOMs , 2D and 3D.

MODE TYPE	Freq. 2D	R/Q 2D	Q_0 2D	R †2D	MAFIA T3*	MAFIA T3
	(MHz)	(Ω AT R0)		MΩ/m	freq.(MHz)	R (kΩ/m)
1-M-1	1036	0.29	36665	0.474	1036	6.516
1-E-1	1250	13.09	50783	24.308	1245	55.19
1-M-2	1583	34.53	37904	37.788	1584	59.67
1-E-2	1711	0.28	38051	0.284	n.v.	n.v.
1-M-3	1886	0.62	71929	1.083	1888	8.663
1-E-3	2067	9.26	38464	7.873	2053	101.5
1-M-4	2219	7.37	31090	4.718	2233	105.1
1-E-4	2309	0.01	66157	0.010	2274?	4.273
1-E-5	2405	1.31	54409	1.351	2414?	7.057
new?					2530	66.23
1-M-5	2580	0.62	40597	0.443	2568	38.33
1-E-6	2618	15.70	32841	9.001	2616	9.760

TE_{11} cutoff 2638 MHz, †R =$R(r)/kr^2$, *nlc_714q_odc30, n.v = not visible.

2 Cavity thermal and stress analysis

The cavity power requirement has been lowered slightly due to a small reduction in voltage per cell with the updated lattices. The maximum is now 39.3 kW in the pre-damping ring vs. 42 kW previously. The damping ring specification with three cavities is only 22.4 kW per cell but would increase if the ring had to be run with one cavity detuned for any reason. To be conservative, and since the lattice design may evolve further, we have chosen to keep the original 42 kW power specification for the time being.

2.1 ANSYS analysis

ANSYS was used to calculate the final frequency corrections as the finite element mesh should be a more accurate approximation of the surface shape than the MAFIA brick mesh. The basic cooling scheme and channel layout has not changed since the previous report. Figure 17 shows the surface heating distribution calculated by ANSYS. The maximum value at the hot spot is about 55 W/cm^2, significantly lower than the scaled PEP-II geometry (77 W/cm^2). Figure 18 shows the resulting temperature distribution. The temperature at the HOM port hot spot is less than 30°C above the water temperature. (compared with 42°C rise for the PEP-II cavity at it's normal operating power of 103 kW). Figure 19 shows the calculated stresses. The Von Mises stress at the hot spot is about 35 MPa (about 5000 Psi) which is well within the fatigue limit for 10,000 cycles of about 18,000 Psi. This stress can be compared with approximately 10,900 Psi (75 MPa), estimated for the PEP-II cavities at 150 kW.

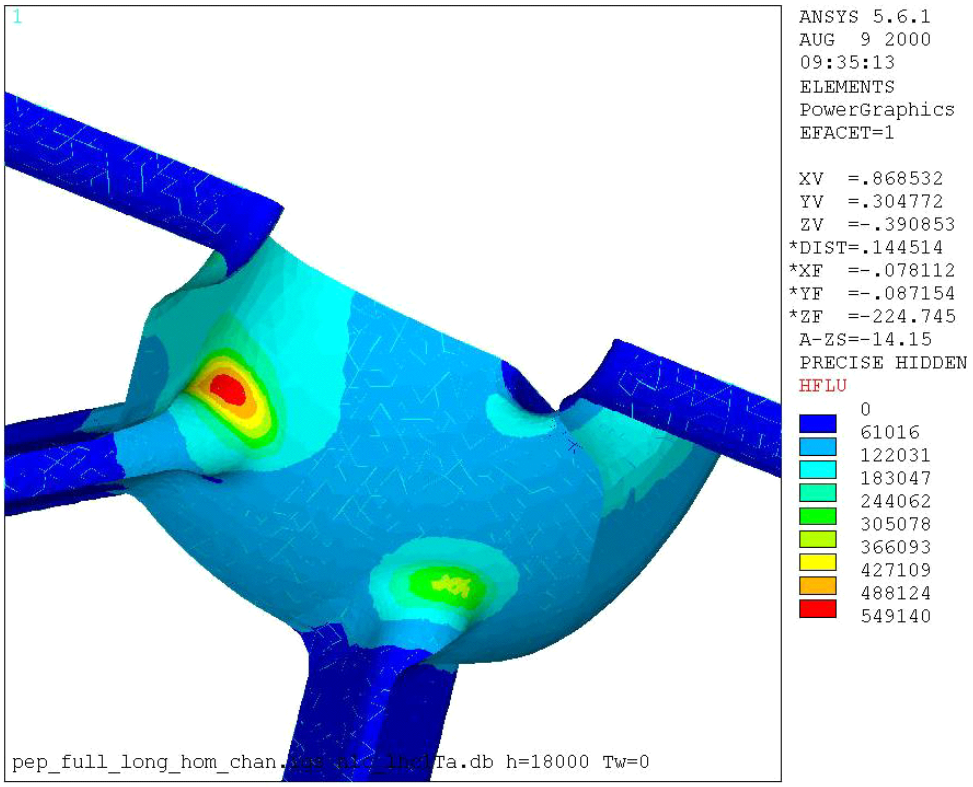

Figure 17. Inner surface heat distribution. Maximum is ~55W/cm^2.

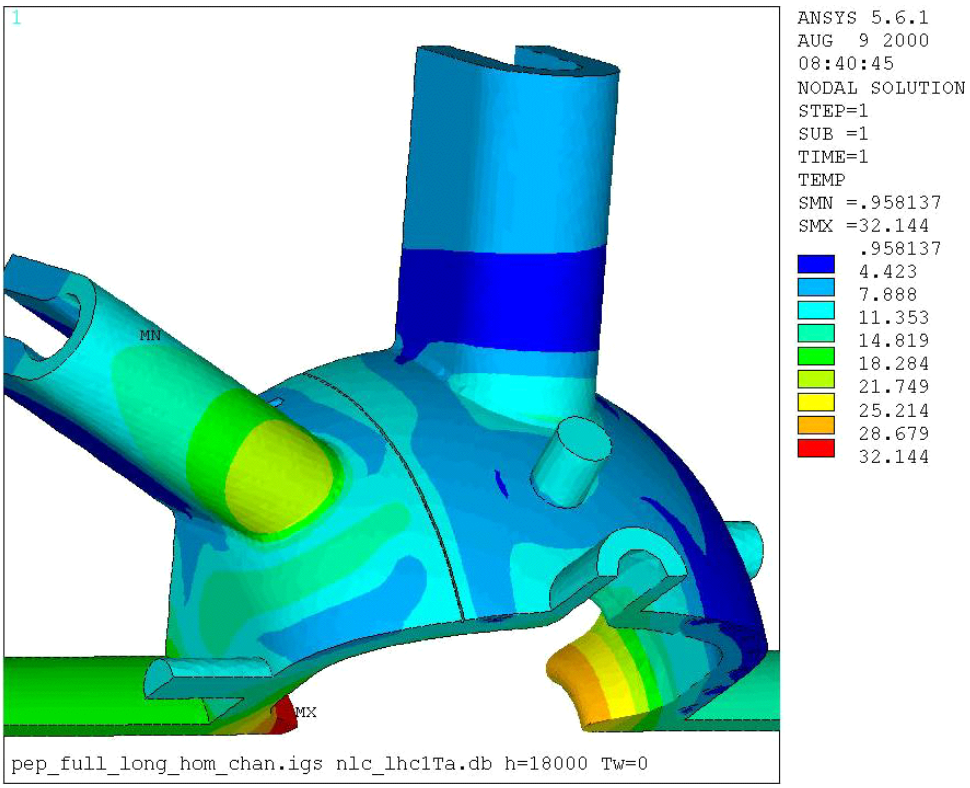

Figure 18. Temperature solution, internal cooling passages. Maximum is ~32°C above ambient water temperature.

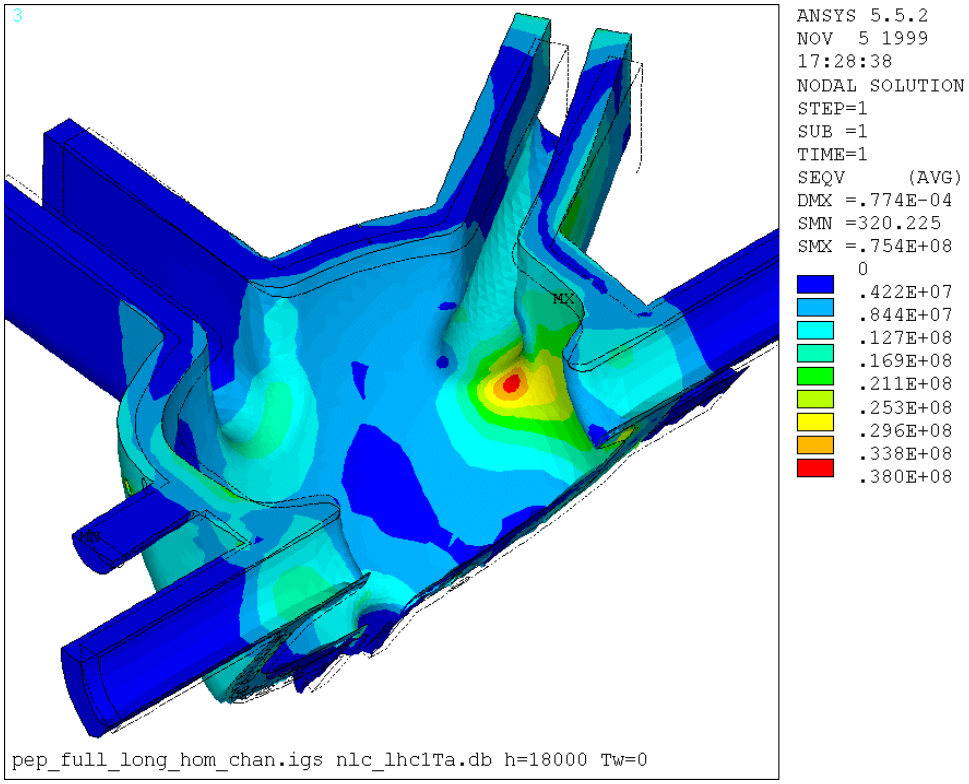

Figure 19. Von Mises stress at 42 kW.
Maximum in the hot spot is about 35 MPa.

2.2 Internal vs. external cooling channels

One possible simplification to the mechanical design of the cavity would be to consider external cooling tubes rather than the internal passages in the current design. These could be formed and torch brazed or soldered onto the outside of the cavity. The hand forming and joining of the tubes would be labor intensive but might be cheaper than the five-axis machining and plating required for the internal passages, especially if the cavity is produced in a region or country with low labor rates. In order to evaluate the effectiveness of external cooling the ANSYS model was adapted by replacing the internal passages with external cooling stripes approximating the application of brazed-on tubes The width and heat transfer properties of the stripe were estimated by comparing a 2D model of a typical cooling tube with that of an equivalent surface patch. Figure 20 shows the 2D model with internal heat transfer properties of the tube and uniform heat loading on the lower surface, representing the inside of the cavity. A typical fillet is assumed between the tube and the bulk surface. Figure 21 shows the temperature distribution that results. Figure 22 shows the mesh of the equivalent surface area. A thermal conducting boundary condition is applied to the central stripe and the heat transfer coefficient is adjusted to achieve approximatley the same bulk temperature distribution, see figure 23. A similar stripe was then applied to the 3D model following the same path as the internal cooling passages, see figure 24. The thermal analysis was re-run with the new external boundary conditions. The temperature increase with the external cooling is modest but significant. The overall temperature profile, figure 25, is similar but the externally cooled case has approximately 40% higher temperture rise than the internal passages. The stresses would likely increase in proportion making this method impractical for the NLC cavity as designed. The temperature increase could perhaps be reduced by using thinner cavity walls and/or more cooling channels and this method may be viable for other applications or frequencies, e.g. for light sources where larger, lower power density structures may be suitable.

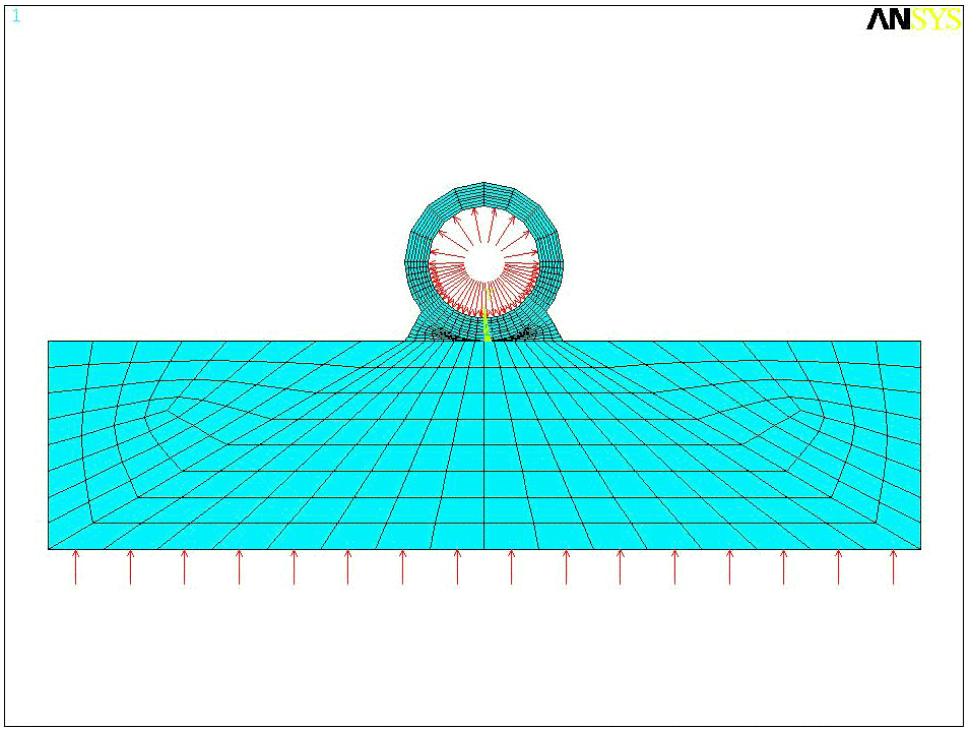

Figure 20. Finite element model of external cooling tube.

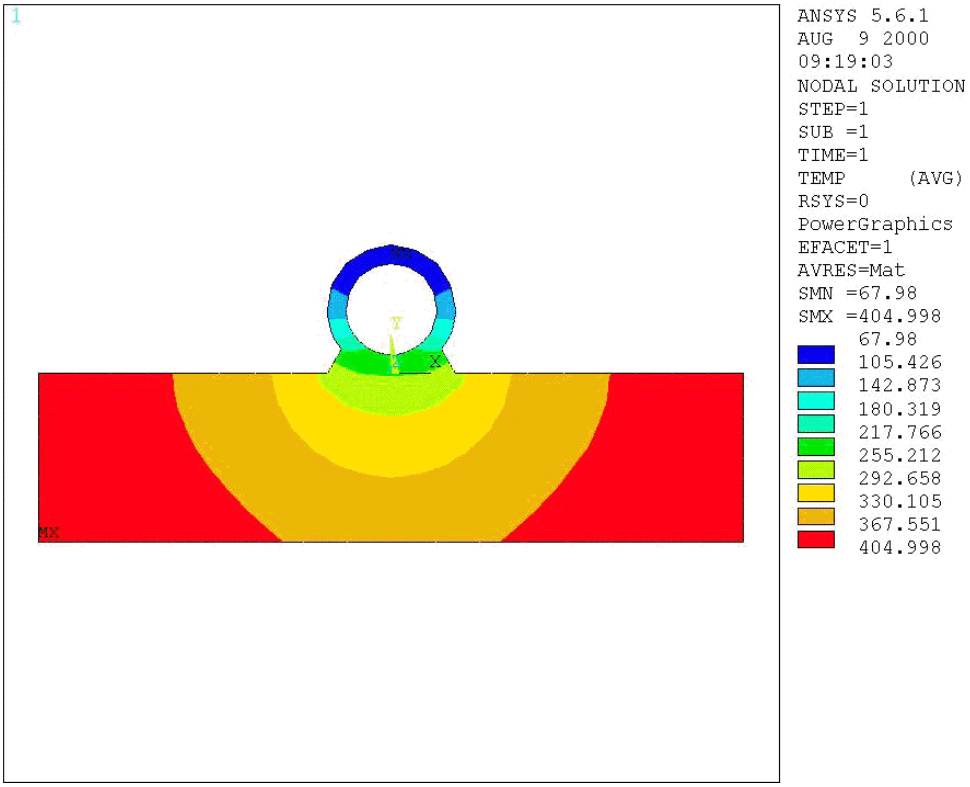

Figure 21. temperature solution for uniform inner surface heating and cooling via external tube (arbitrary units).

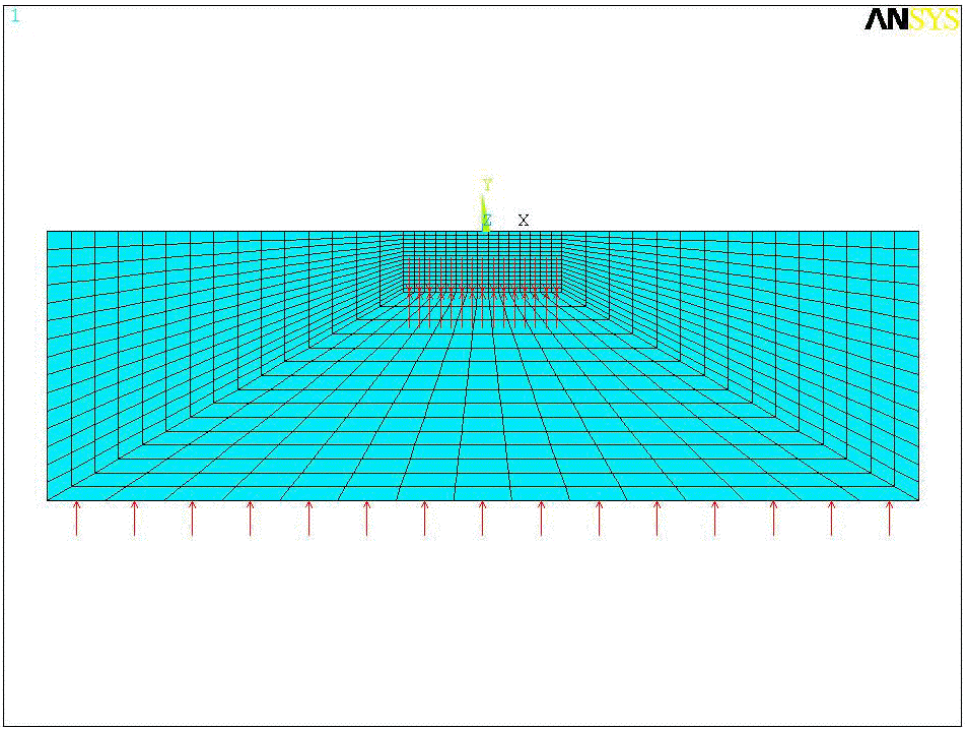

Figure 22. Finite element model of equivalent surface cooling area.

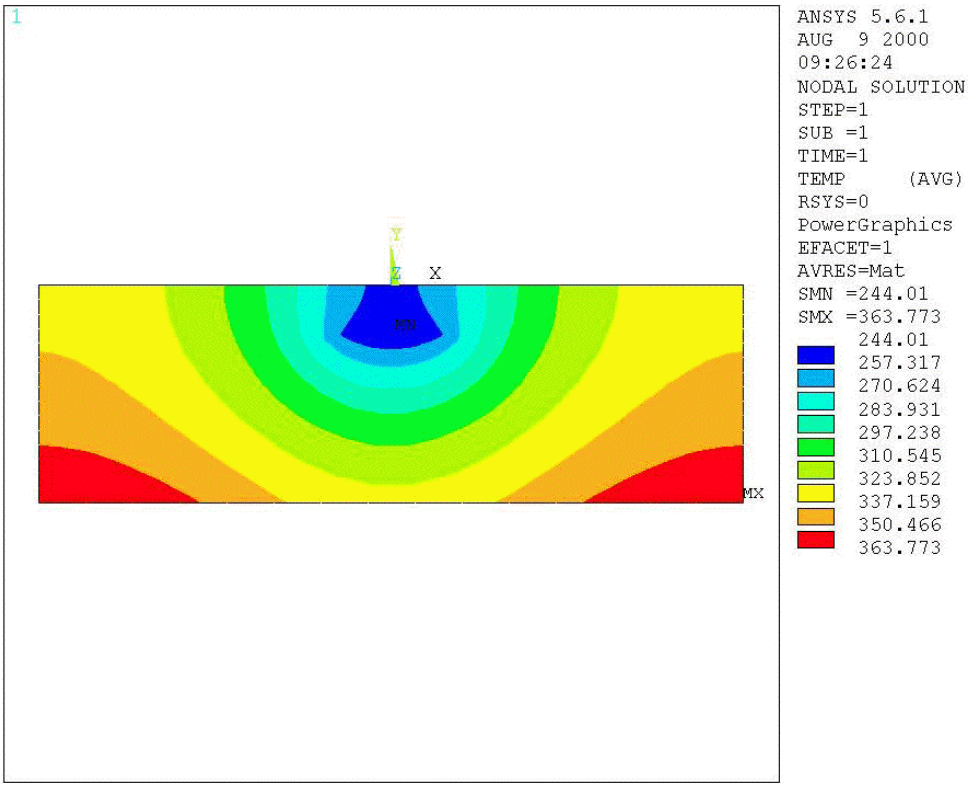

Figure 23. temperature solution for uniform inner surface heating and cooling via equivalent external area (arbitrary units).

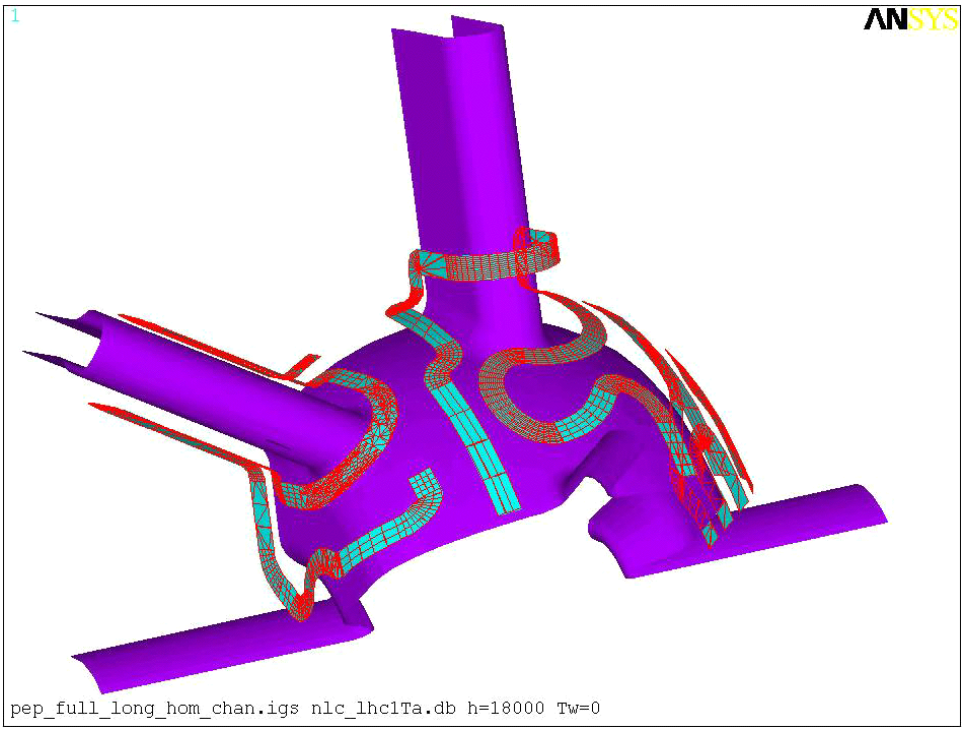

Figure 24. Surface stripes used to approximate external cooling tubes.

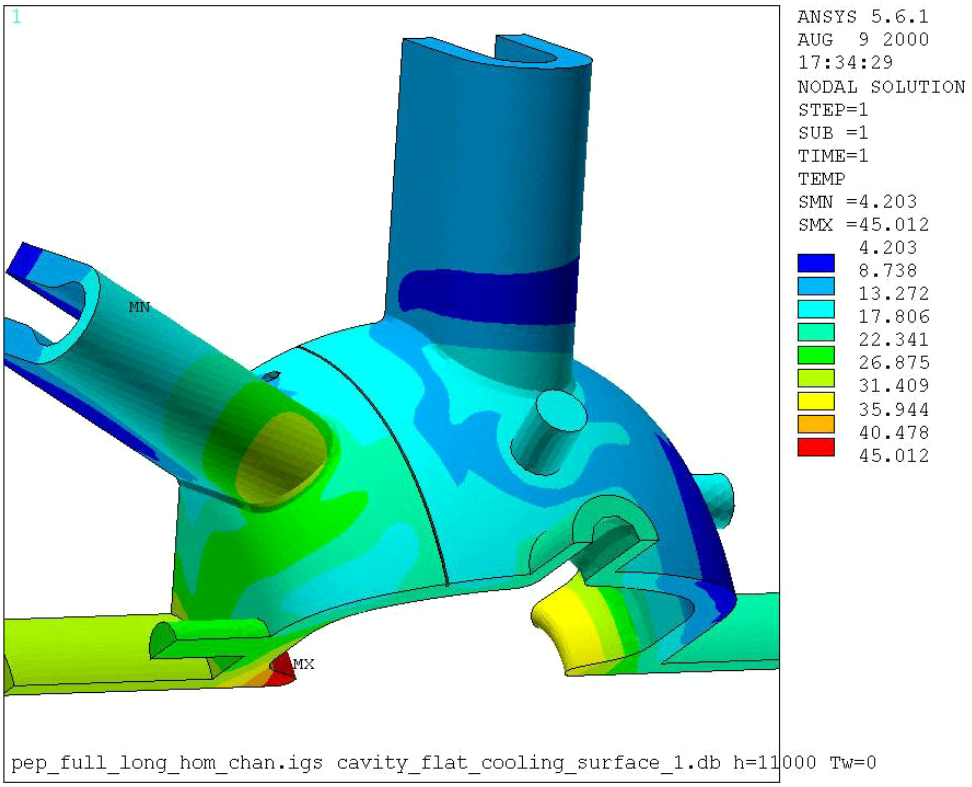

Figure 25. Temperature solution for 3D model, external cooling tubes. Maximum is ~ 45°C above ambient water temperature.

3 Cavity fabrication and assembly

The proposed cavity system broadly follows the layout used for PEP-II. Modifications have been made to simplify the mechanical design, reduce the part count and substitute cheaper fabrication methods or operations where possible. This has been achieved without compromising the RF performance and in fact the HOM damping, thermal and stress performance have all been improved compared to the baseline of a scaled PEP-II design.

3.1 General fabrication approach

We propose to make the cavity body from only two main parts. The bulk of the cavity, including one nose cone, the RF power port, tuner ports and pickup/observation ports, will be machined from a single forging, figure 26. Because of the relatively small size of the cavity compared to PEP-II, a forging is ecconomically preferable to a fabricated assembly. A custom forging can be obtained at close to final dimensions to minimize the material cost and the amount of machining required, figure 27a. The remainder of the cavity, including the other nosecone and the three HOM ports, will be made from a second forging, figure 27b. This second smaller forging forms a "lid" to close off the "bowl" of the main body. All the ports are integral to one or other of the forgings and are created by simple turning or by a combination of wire- and plunge-EDM or conventional machining, figures 28, 29. This scheme eliminates many of the joining or machining operations of the PEP-II fabrication method. A single joint, formed by E-beam welding, attaches the lid to the body. The components can be held and manipulated by mounting bosses on the forgings. These can also derve as datum points during machining and mounting points for the finished cavity. For more details on the fabrication process see [1].

The cooling channels will be formed by five-axis machining on the outside of the body and lid, see figure 30. They will be closed by conventional electroforming using standard "brightening" additives to facilitate plating into the recesses. The stainless steel water fittings will be incorporated during this stage. Preliminary evaluation indicates that brazed-on external cooling lines, though potentially cheaper, would not provide adequate cooling for this application. In the final stage flanges will be attached by e-beam or TIG welding. Circular flanges will be used on all ports to minimize costs. This is feasible because of the modest size of the cavity and the compact nature of the dumbbell port cross section.

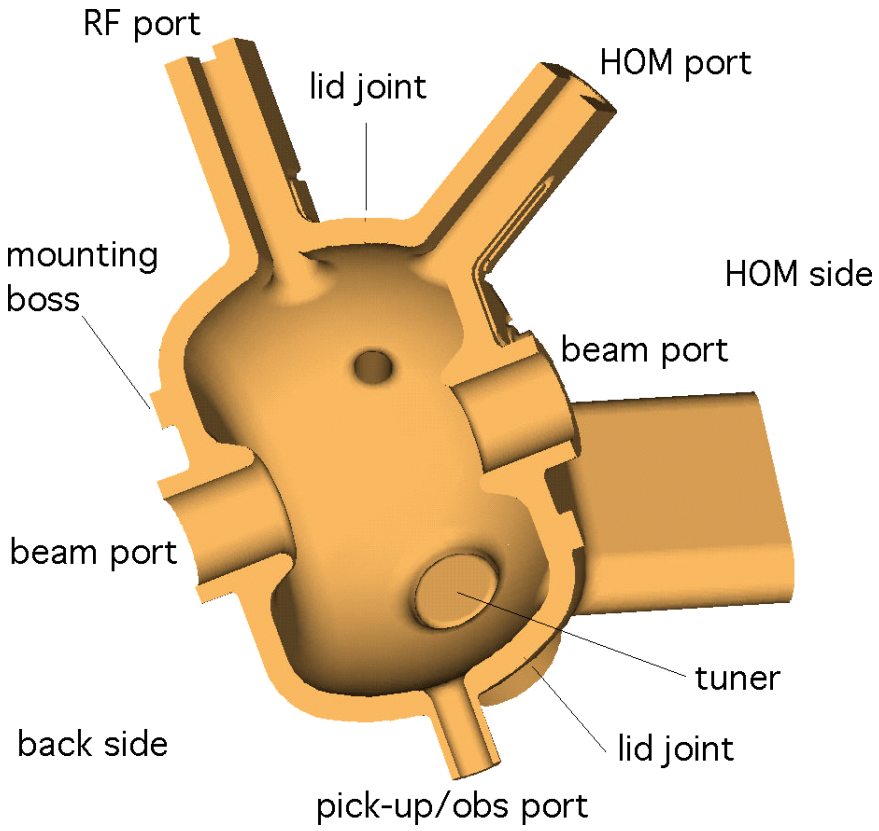

Figure 26. Section through two main pieces of cavity.

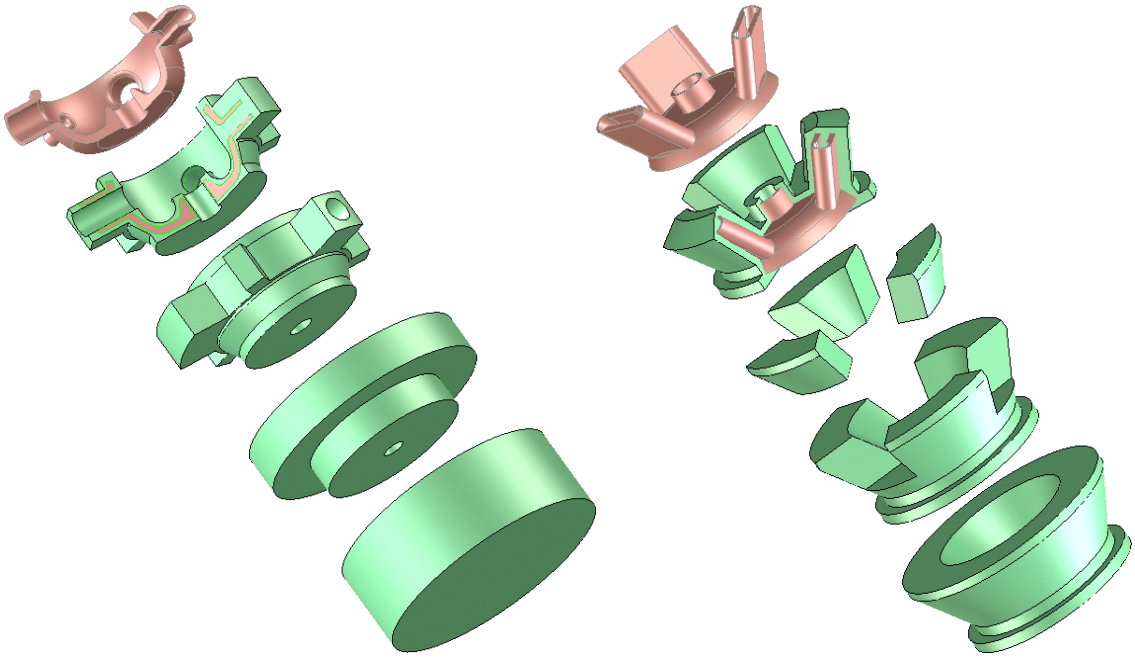

a. Body B. "lid"

Figure 27. Development of body and lid from forgings.

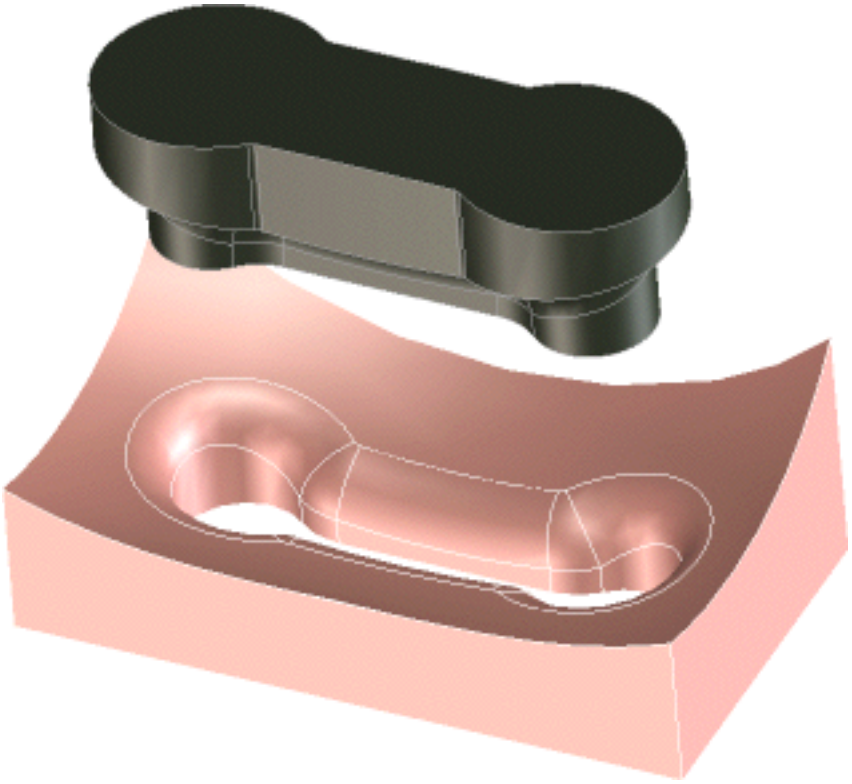

Figure 28. CAD model of EDM sample with graphite electrode.

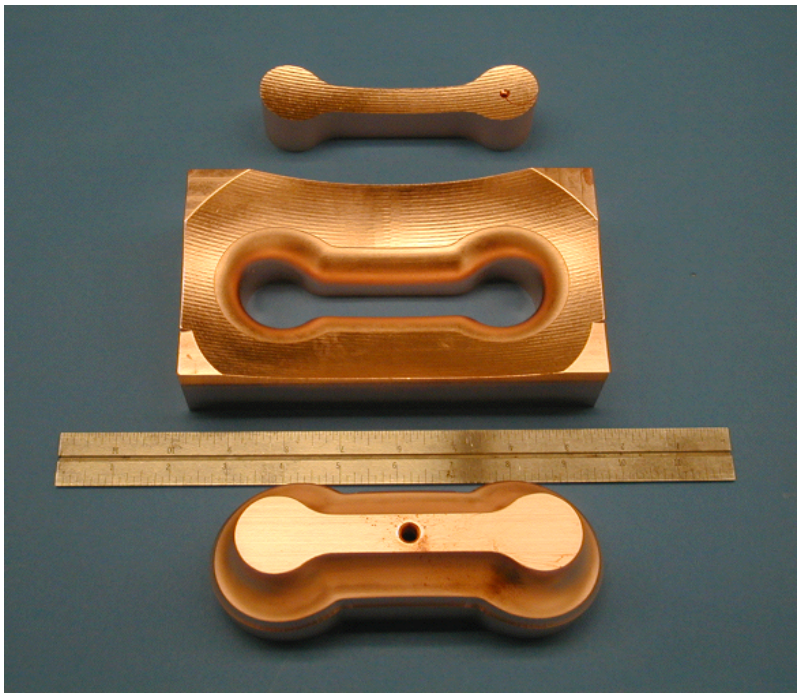

Figure 29. EDM sample with tellurium copper electrode (bottom) and wire burnout (top).

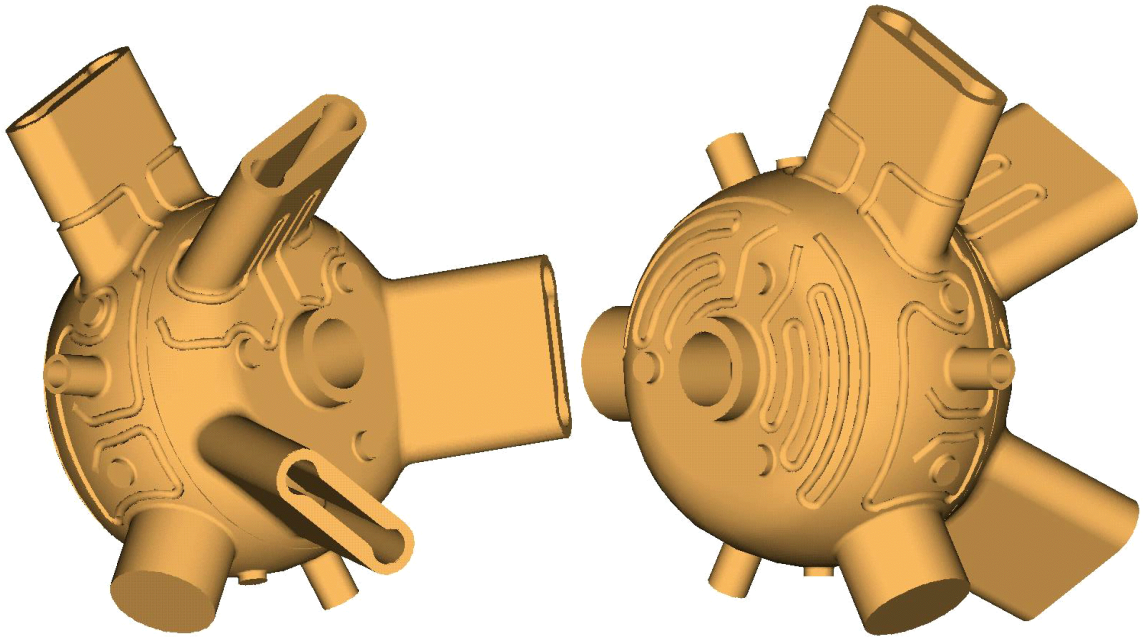

Figure 30. Outside of cavity with partial channels (plating not shown).

3.2 Assembly, mounting and installation

Figures 31, 32 and 33 show views of the conceptual assembly, though this layout could be modified if necessary depending upon tunnel dimensions, etc. Each cavity has three demountable HOM loads which are shown folded for compactness. The first part of the HOM load is a taper from the dumbbell cross section to a simple rectangle. The end part of the load contains wedges of RF absorbing material similar to those used in PEP-II. Each load has a small viewport through which the absorbing material can be inspected if necessary. One port can be used for a pickup antenna to monitor HOM signals if desired. Each cavity has one fixed and one motorized tuner. The fixed tuner will be set to accomodate any production tolerances while the moving one will be used to compensate for beam loading, temperature changes etc.

Each cavity will have a coupling box containing the RF window, a HOM load and a pumping port. The coupling box shown in the figures is based on the PEP-II design and incorporates a 90° bend to shield the window from line-of-sight to the beam. The cavities can be mounted with the coupling port vertical or horizontal, whichever is most convenient. The waveguide is shown coupling end-on to the cavity but it could also be mounted to couple through the side wall if desired. A photon mask can be incorporated in the upstream beam pipe within the region of the HOM loads.

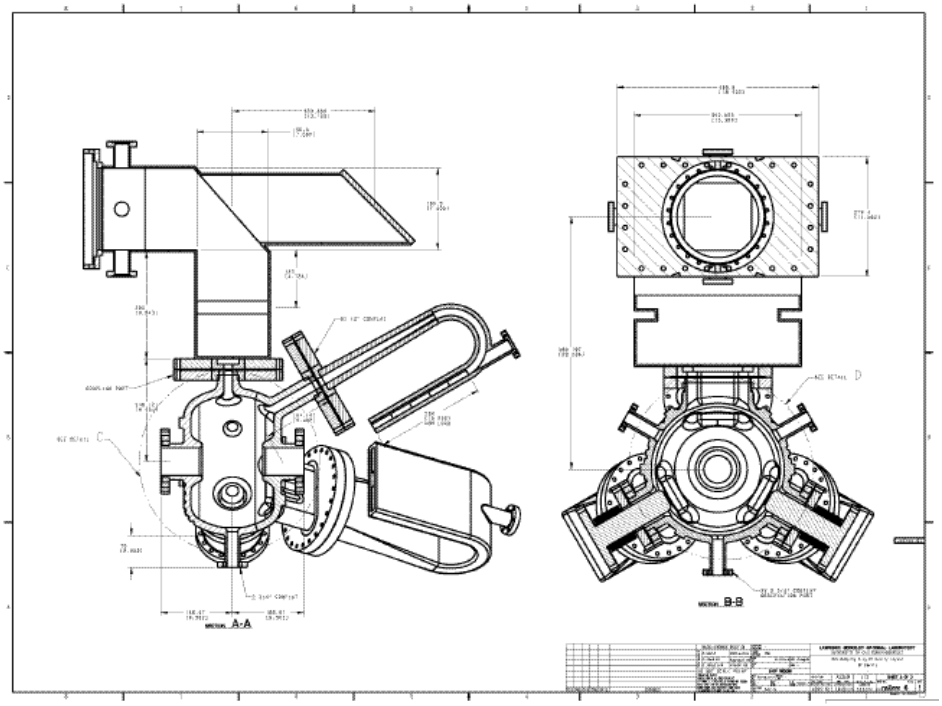

Figure 31. Partial assembly drawing of cavity system.

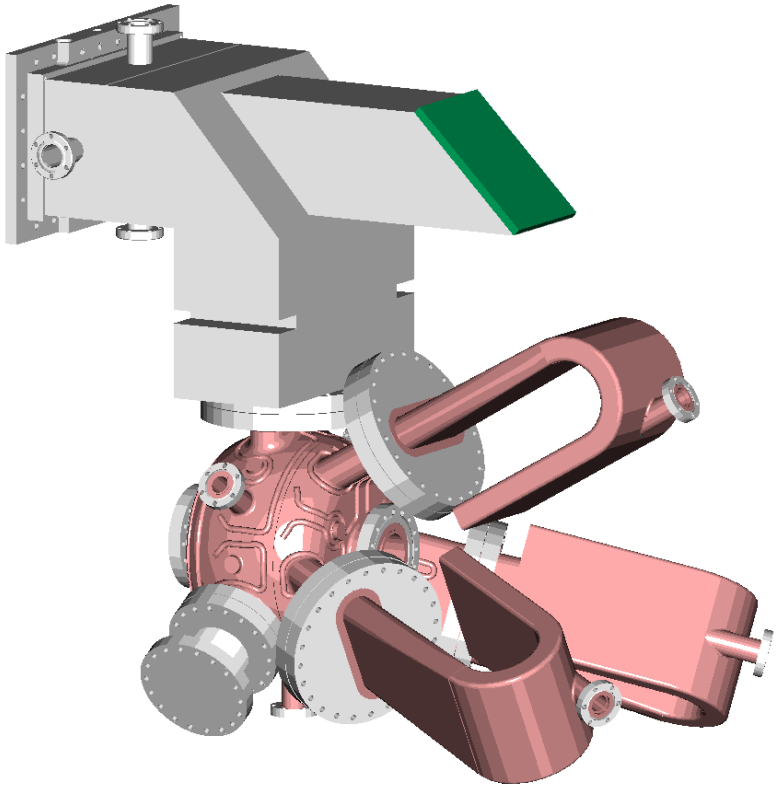

Figure 32. Lid/HOM-side view of full cavity assembly.

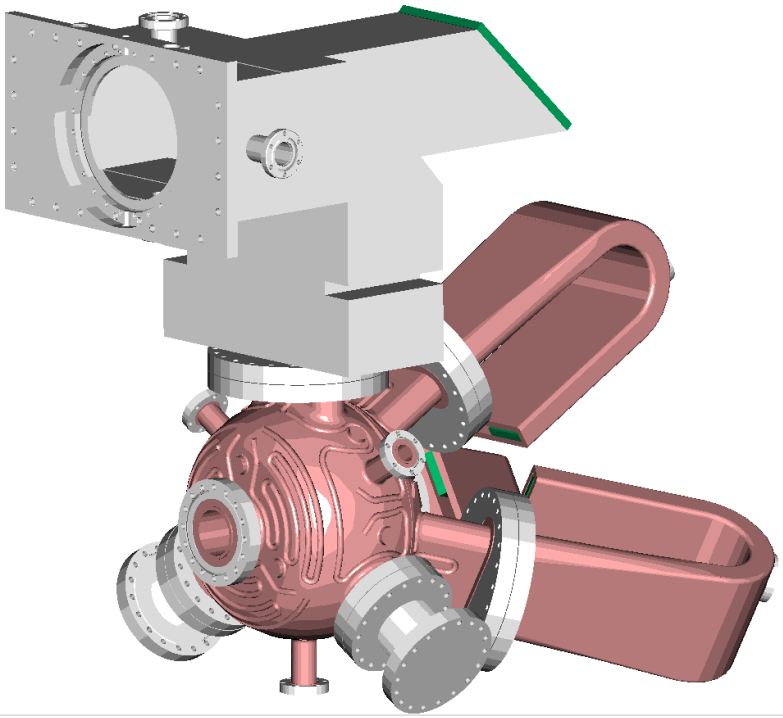

Figure 33. Body-side view of full cavity assembly.

4 HOM waveguides and loads

The HOM load layout is similar to the PEP-II design [8], see figure 34. Two tapered sections of lossy dielectric tiles (SiC + 40% AlN), are mounted at the end of the HOM waveguide. The compact dumbell waveguide cross section used in the cavity is continued through the flanges. Beyond the flange the section is gradually tapered to a shallow rectangular profile with the same cut-off frequency (900 MHz). The HOM load tiles are assembled in the rectangular section for simplicity and the wedges are gradual enough to give a good match (VSWR < 2:1) for all of the HOMs below cut off.. The waveguide is folded inwards for compactness, although it could be straight or folded outwards if required. Figure 35 shows a section through the folded HOM load assembly. Figure 36 shows a perspective view in which the smooth taper in both height and width can be seen. A viewport is included which can be used for inspection of the tiles, in case a failure is suspected, or can be used for a pick-up antenna to monitor HOM transmissions.

Figure 37a shows a snapshot of the MAFIA simulation for an incoming wave at 1 GHz in the TE_{01} waveguide mode. The VSWR at this frequency is less than the 2:1 requirement and most of the energy is absorbed at the front of the load. Figure 37b shows the same view at 3 GHz; the wave penetrates further into the load and the energy is dissipated towards the back of the tapers but the VSWR is still good, see figure 38. The loads continue to have a good response well above cutoff.

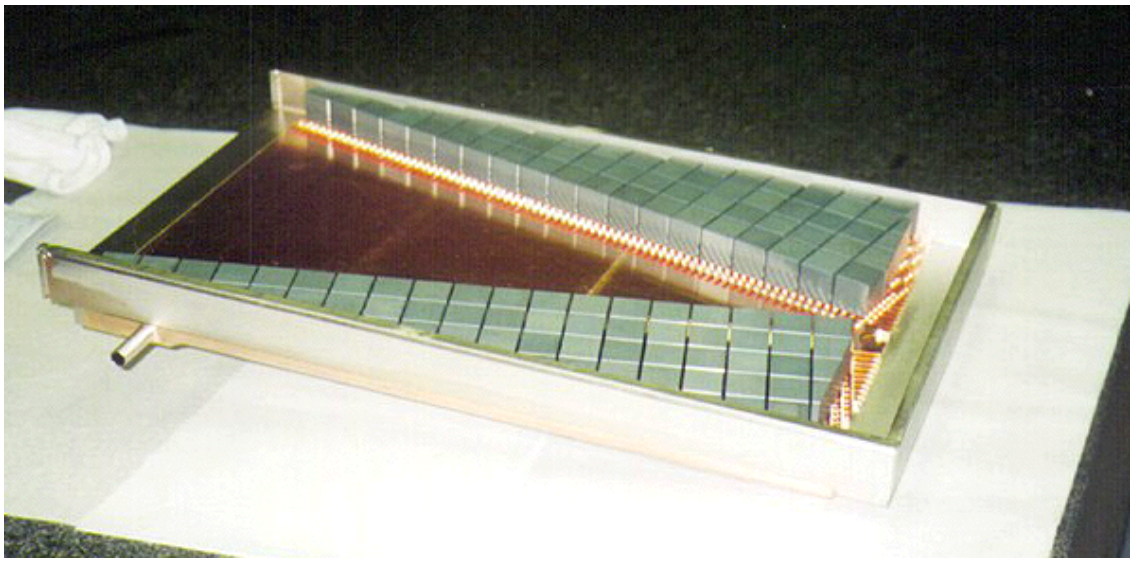

Figure 34. PEP-II HOM load absorbing tile array.

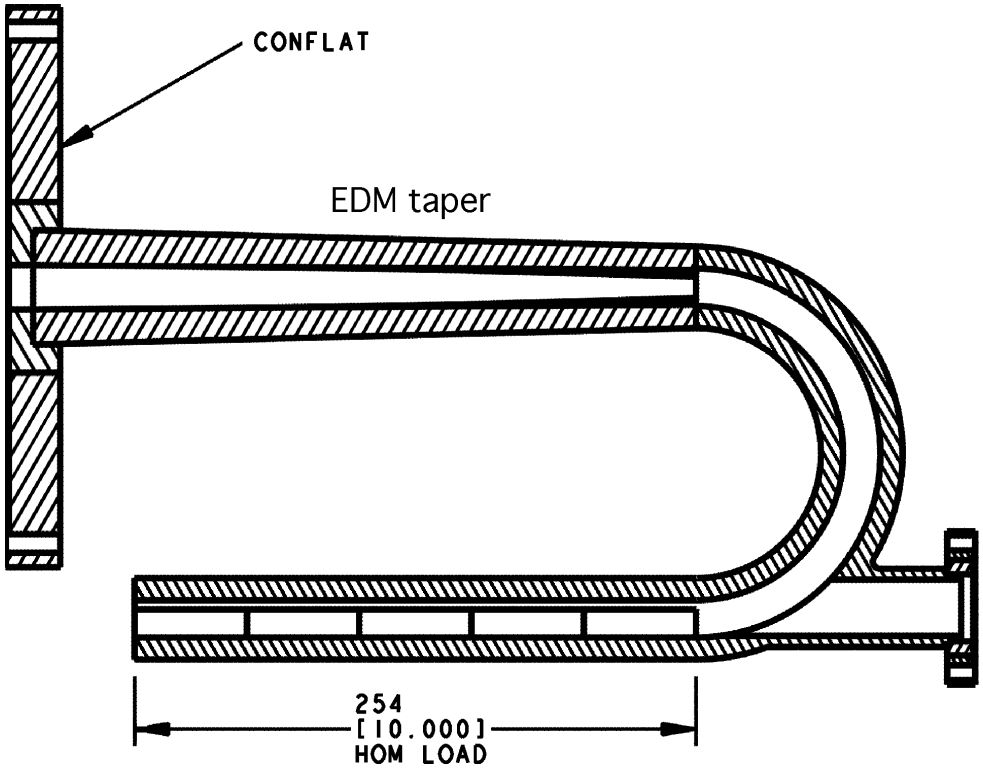

Figure 35. Section through HOM load.

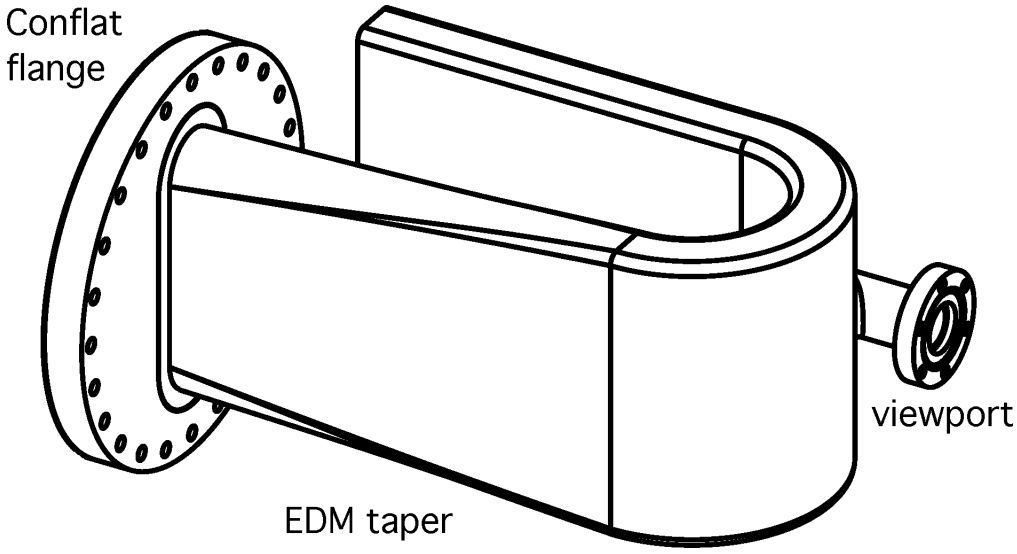

Figure 36. HOM load assembly.

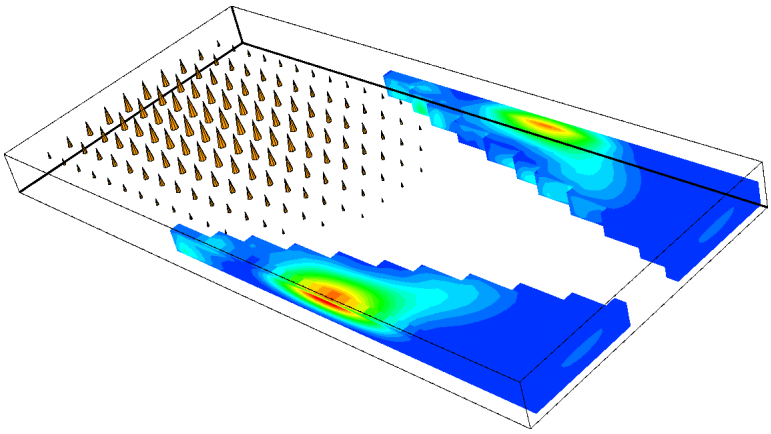

Figure 37a. MAFIA incoming wave at 1 GHz and losses in ceramic.

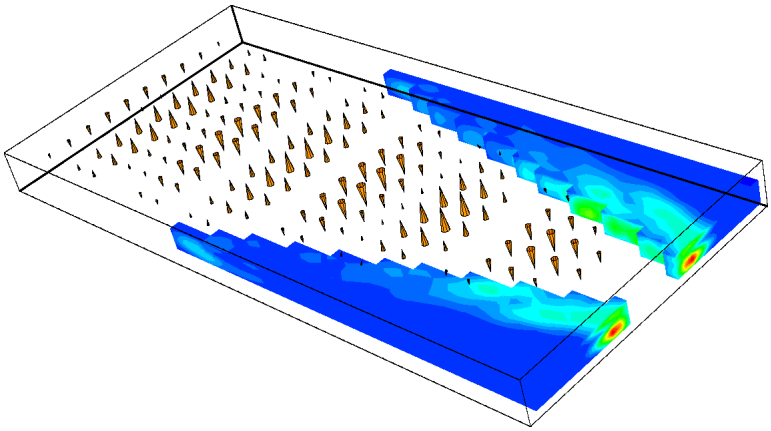

Figure 37b. MAFIA incoming wave at 3 GHz and losses in ceramic.

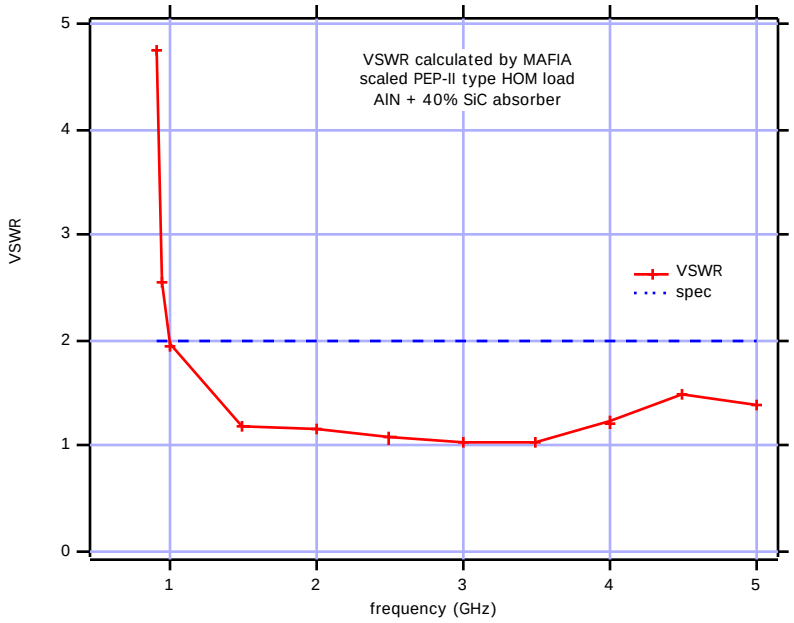

Figure 38. VSWR of scaled PEP-II type HOM load.

5 Window and coupler

The window design, figure 39, has been studied using the MAFIA time domain module T3 with the S-parameter macro, which can calculate steady state reflection and transmission coefficients, VSWR etc. The basic design work was reported in the FY99 report [1]. This design has been developed to be tunable to other frequencies besides the NLC operating frequency of 714 MHz, and a version has been made for Los Alamos that has been tested at 700 MHz [9,10]. Sections 5.1, 5.2 and 5.3 describe the design and development of these prototypes. Section 5.4 describes the manufacturing and 5.5 describes the testing of the first prototypes. The same materials and processes would be used for NLC damping ring windows.

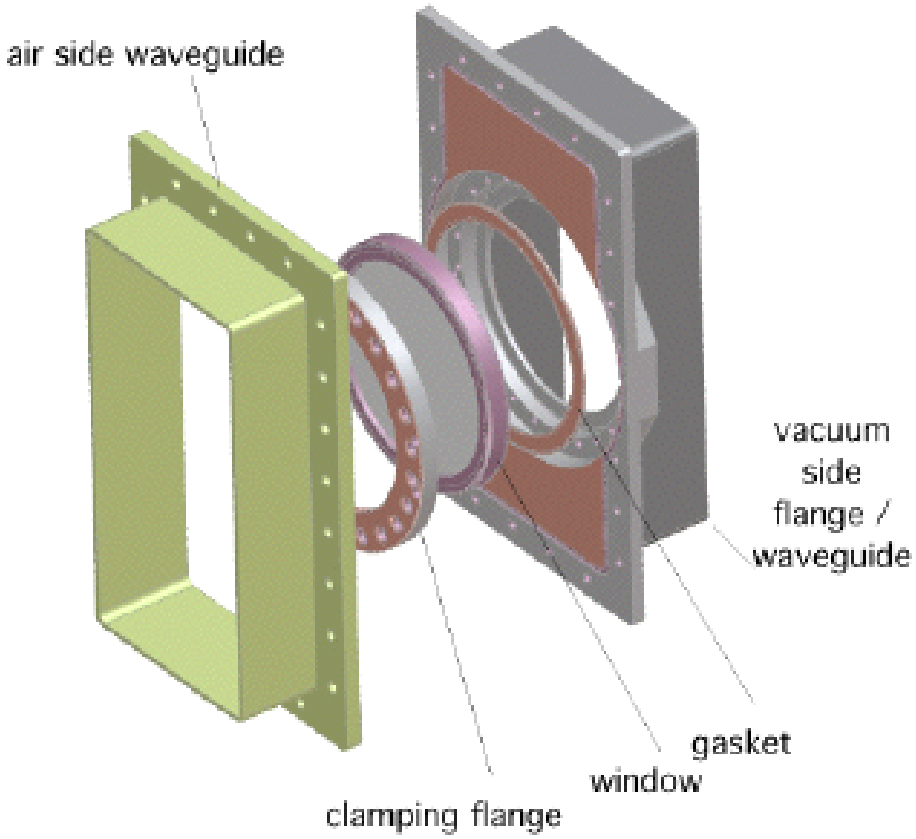

Figure 39. RF window assembly.

5.1 Window analysis in MAFIA

Figure 40 shows the MAFIA model of the window with the TM_{01} waveguide mode propagating. Figure 41 shows the reflection coefficient close to the matched frequency (700 MHz for LANL).

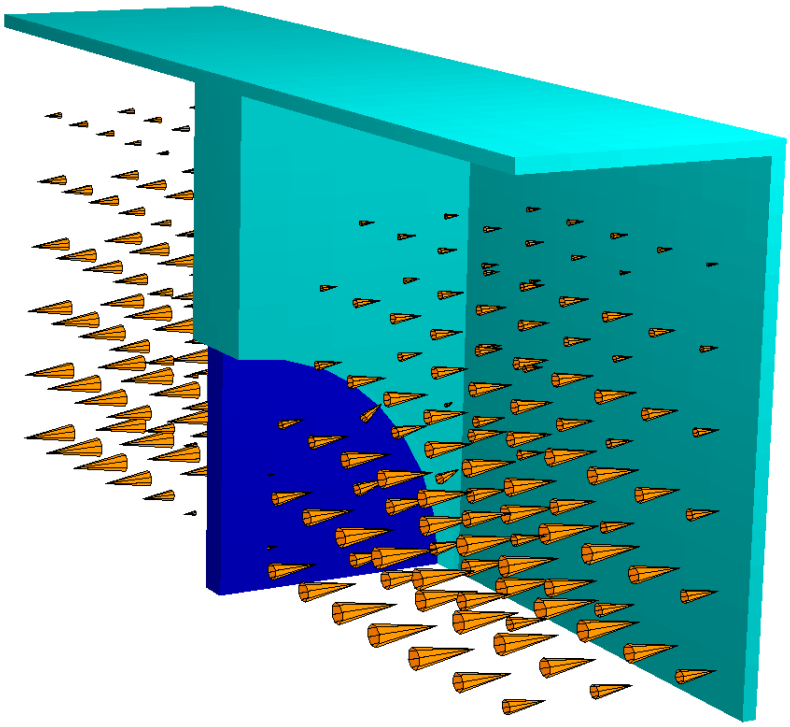

Figure 40. Window with normal TM_{01} waveguide mode propagating.

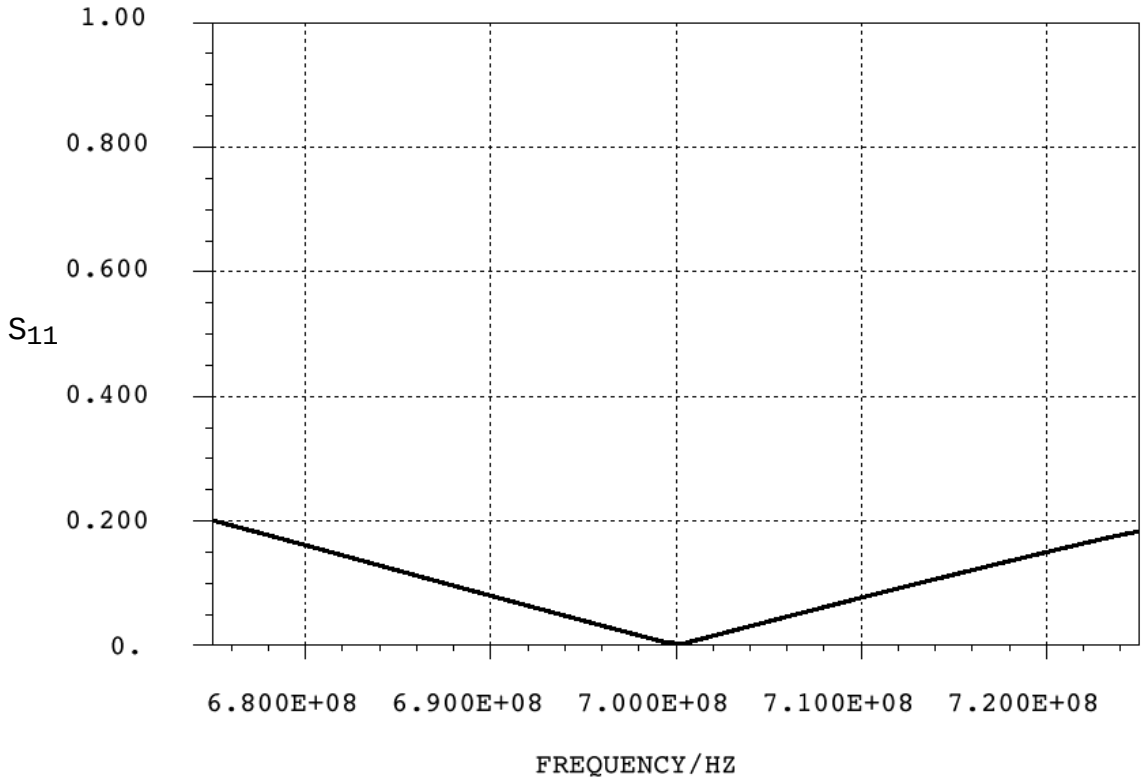

Figure 41. S_{11} of waveguide window.

Figure 42 shows how the frequency varies with ceramic thickness and iris length for the chosen geometry. To allow for manufacturing tolerances the window match frequency can be fine tuned by trimming the thickness of the flange in the last step of the manufacturing sequence when the knife edge is cut. Brazed assemblies were made slightly oversize on the flange thickness to allow them to be cut to final size after the frequency is measured in the cold-test fixture. The ghost modes are resonances in the iris that are orthogonal to the propagating mode and therefore confined.

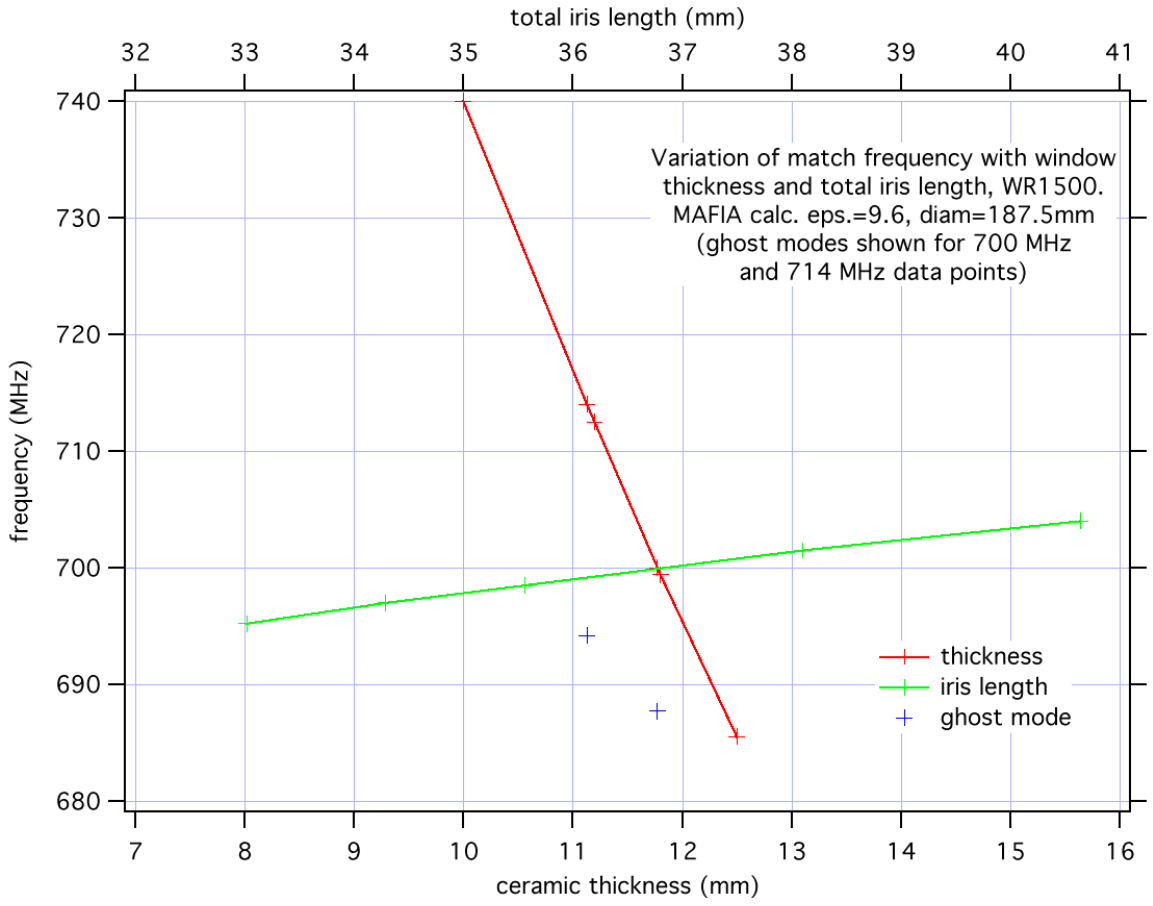

Figure 42. Tuning of window assembly.

5.2 Cold-test measurements

In order to specify the thickness of the windows for production the dimensions of the ceramic were fine tuned by RF measurements in a cold-test model of the iris, figure 43. Two ceramics were initially ordered, one at the thickness estimated from the MAFIA runs and one a little thicker. The two ceramics were measured in a simple

fixture and the frequencies compared with the MAFIA predictions. Figure 44 shows the calculated and measured match frequency verses ceramic thickness. There is a small offset between the two curves, which can be accounted for by the actual dielectric constant being slightly different from that assumed in the MAFIA calculations. The slope of the curve predicted by MAFIA is -19.9 MHz/mm, while that from the measurements is -19.5 MHz/mm. The slope of the measured data was used to extrapolate to estimate the ceramic thickness which should yield a match frequency of 700 MHz. Note that there is a second slight offset in the plots because the simple fixture was slightly thicker than the final flange thickness. This was accounted for in the tuning and the ground ceramic when remeasured came out very close to the expected frequency (701.1875 measured vs 700.537 expected). Figures 45,46 show the measured transmission and reflection coefficients for the tuned window in the simple test fixture. Figure 47 shows the reflection coefficient on a linear scale to compare with figure 41. When the ground ceramic was measured in a new fixture with the correct thickness the frequency dropped to 699.6875, which is acceptably close to the desired value.

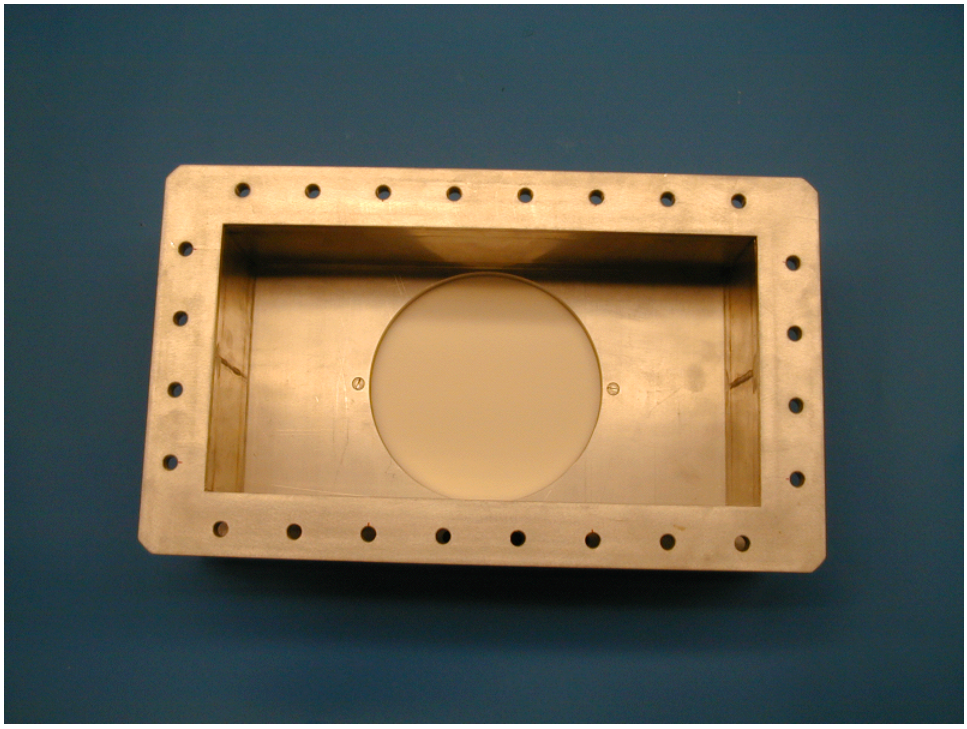

Figure 43. Simple cold test fixture.

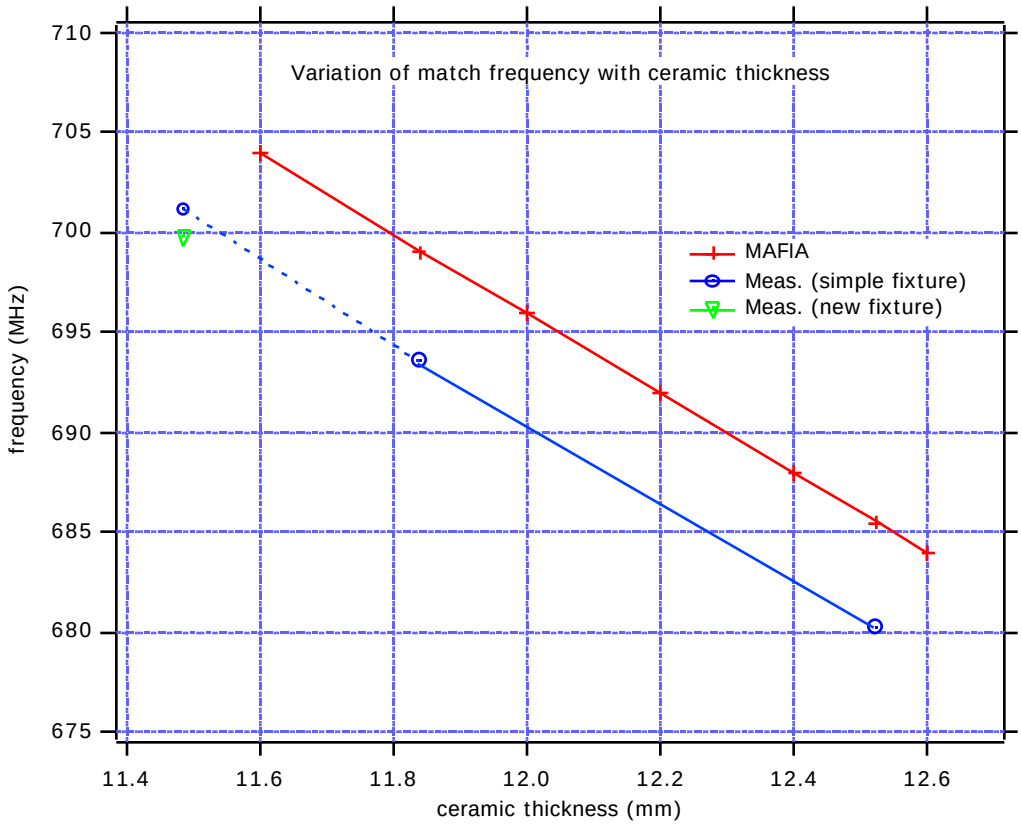

Figure 44. Variation of match frequency with ceramic thickness.

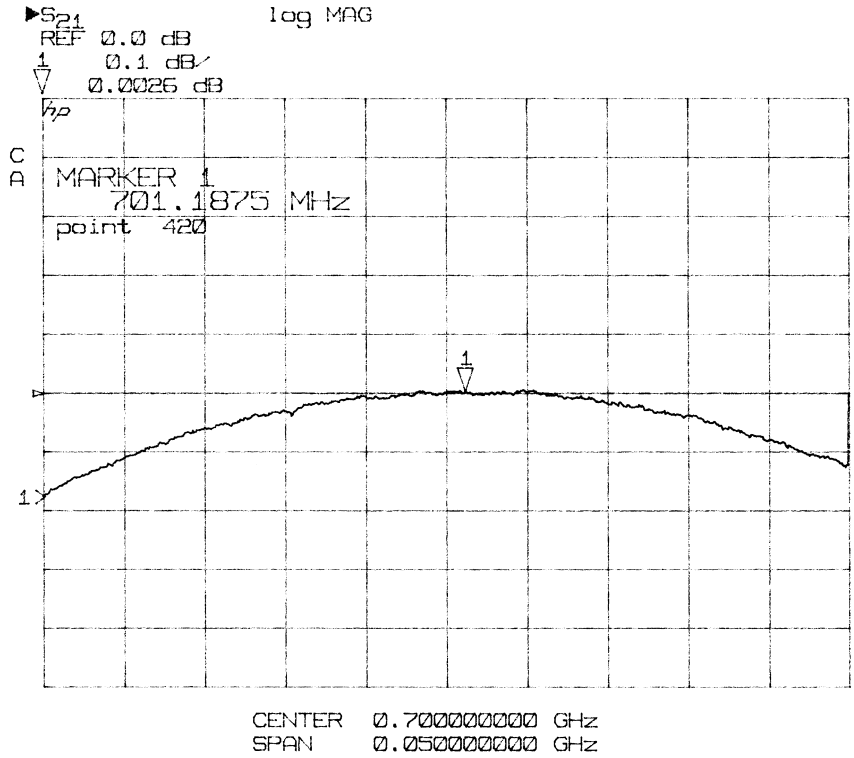

Figure 45. S_{21} of tuned ceramic in simple cold-test fixture.

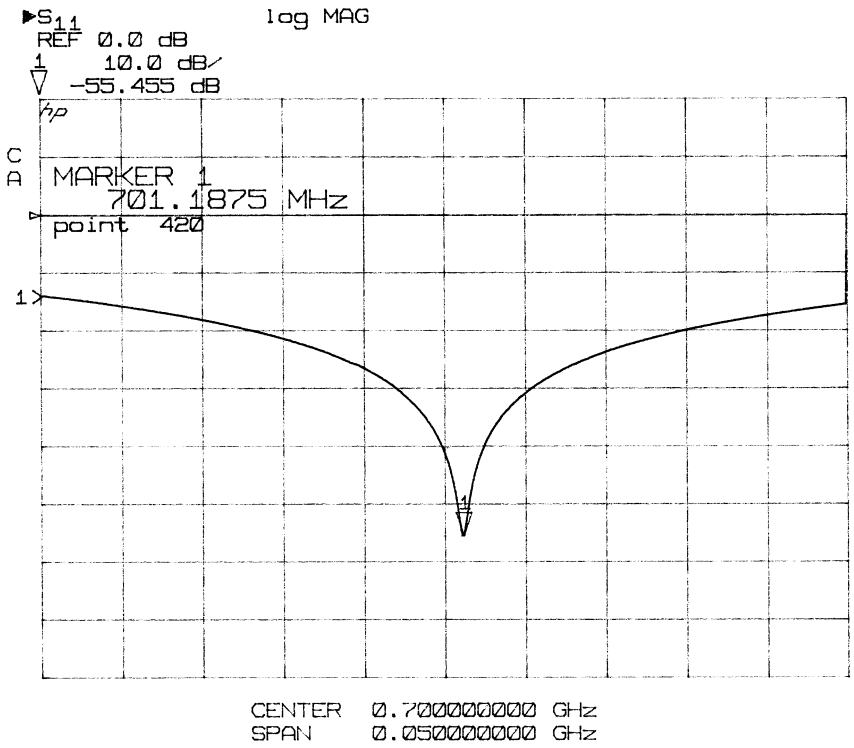

Figure 46. S_{11} of tuned ceramic in simple cold-test fixture.

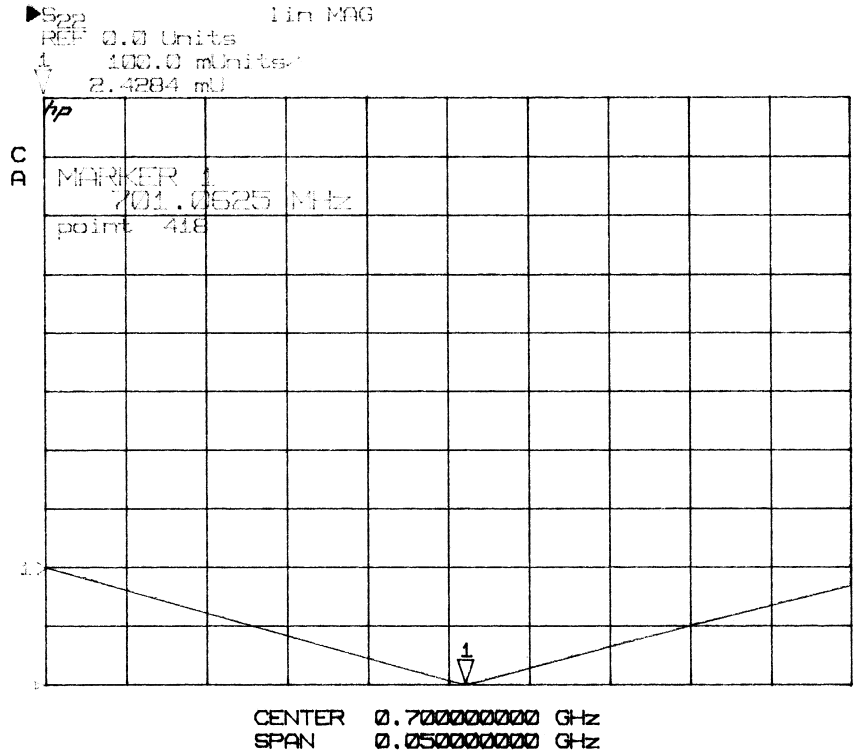

Figure 47. S_{11} of tuned ceramic, linear scale.

5.3 Window analysis in ANSYS

In service this window could see a temperature rise of up to 70°C due to RF losses in the ceramic and coating, multipactoring etc., which could cause the window to crack under thermal expansion. In order to solve this problem for the PEP-II B-Factory, a procedure was developed for creating a vacuum tight alumina window that is under compression under all operating conditions [11]. The concept and preliminary ANSYS analysis were described in detail in the previous report [1]. The full development of the window for LANL is described elsewhere [9,10].

The mechanical design follows the assembly procedure developed for PEP-II. The window is brazed into a thick stainless steel flange containing a cooling channel. The flange is initially slightly larger than the ceramic but is constrained by an even thicker molybdenum keeper ring as the furnace temperature is ramped up, see figure 48. Once the stainless steel ring reaches it's yield point it plastically deforms and is kept from expanding as much as it would otherwise. As the temperature continues to rise the alumina disk catches up to the stainless steel / molybdenum combination, until the desired brazing gap is attained at brazing temperature. On cooling down the stainless ring tries to contract more than the alumina putting the ceramic into compression. The outside of the stainless ring is "green" fired (in wet hydrogen), and the molybdenum keeper is titanium nitrided to prevent sticking. Careful control of the room temperature clearances and the use of shims allows the optimum brazing gap of 0.001" - 0.003" (25 - 76 μm), to be obtained each time. The furnace cycle contains a long hold period during the cool down to allow local stresses between the ceramic and the cooling ring to be relieved. Table 7 and figure 49 give the furnace temperature profile. Figure 53 shows a window assembly ready for brazing. The process was simulated in ANSYS to fine tune the scaled dimensions and several ring tests were performed without ceramics first to check the parameters.

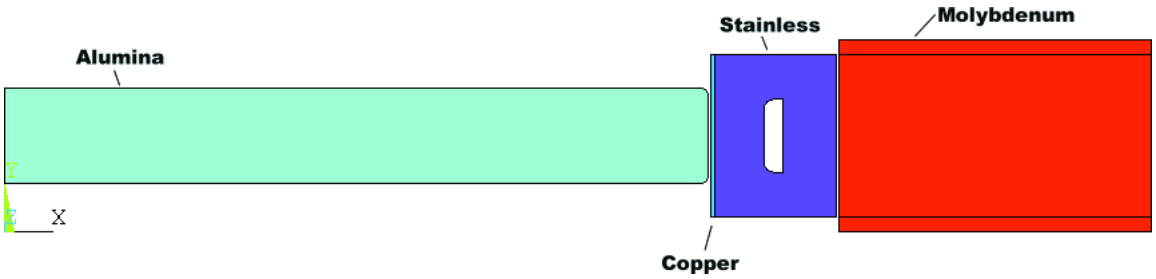

Figure 48. Material configuration for 700 MHz window braze.

Table 7. Braze furnace temperature set points.

Temperature	rate	Hours
℃	deg/min	
23		0
960	10	1.6
960	hold, 1hr	2.6
1025	15	2.6
1025	hold 5 mins	2.7
440	1	12.5
440	hold, 10hr	22.5
40	1	29.1

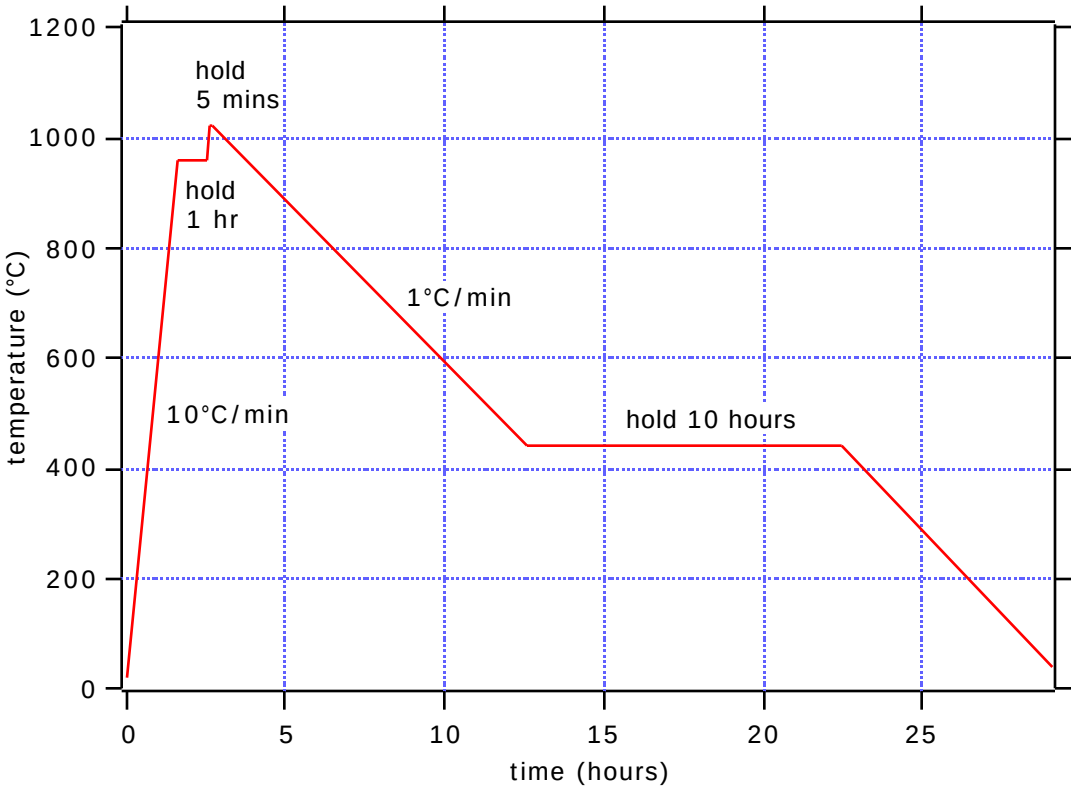

Figure 49. Braze furnace temperature profile.

5.4 Fabrication

The ANSYS calculations were fine tuned by doing a few "bimetallic" ring tests in which the stainless / molybdenum combination was tested without ceramic. Figure 50 shows the assembly and figure 51 shows the combination in the furnace at temperature.

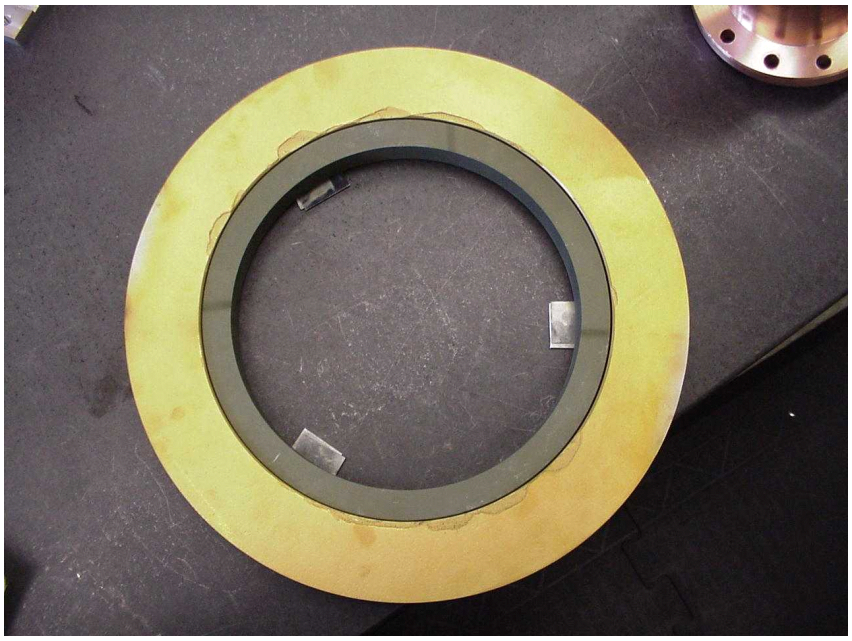

Figure 50. Molybdenum and stainless rings prior to furnace test.

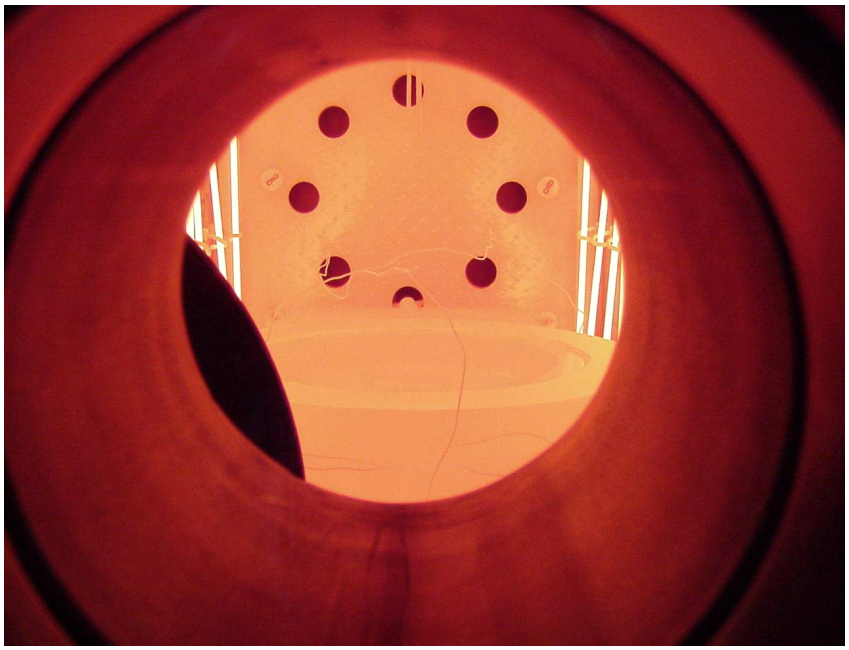

Figure 51. Stainless steel and molybdenum rings at 1025°C through the window of the furnace.

After the ANSYS calculation was calibrated we moved on to the full window braze tests. The real windows use a ring containing the cooling water channel and this was accounted for in the simulations. The hollow stainless steel ring is made from two pieces brazed together at a higher temperature than the window braze, see figure 52. Figure 53 shows a window braze assmbly ready to go in to the furnace. The furnace temperature cycle was as shown in figure 49.

Unfortunately the first brazement ended with a cracked alumina window. The braze looked smooth and uniform, but there was a crack running from the braze interface into the window. The first centimeter of he crack was relatively straight and went through the entire thickness of the alumina. The crack continued from there in an almost complete circle along one of the surfaces. After some investigation it was concluded that the most likely cause was direct and uneven heating by the infrared radiation from the unbaffled heating elements. SLAC had some experience with this problem when baking out ceramics during the PEP-II project. The fact that the Vacuum Industries furnace had a rectangular element profile, figure 54, could have added to the uneven heating. Putting a stainless steel baffle, figure 55, around the braze assembly was successful in eliminating the problem. Figure 56 shows the first successful window brazement. The remaining three prototype brazes were all successful.

Figure 52. Hollow cooling ring parts ready for brazing.

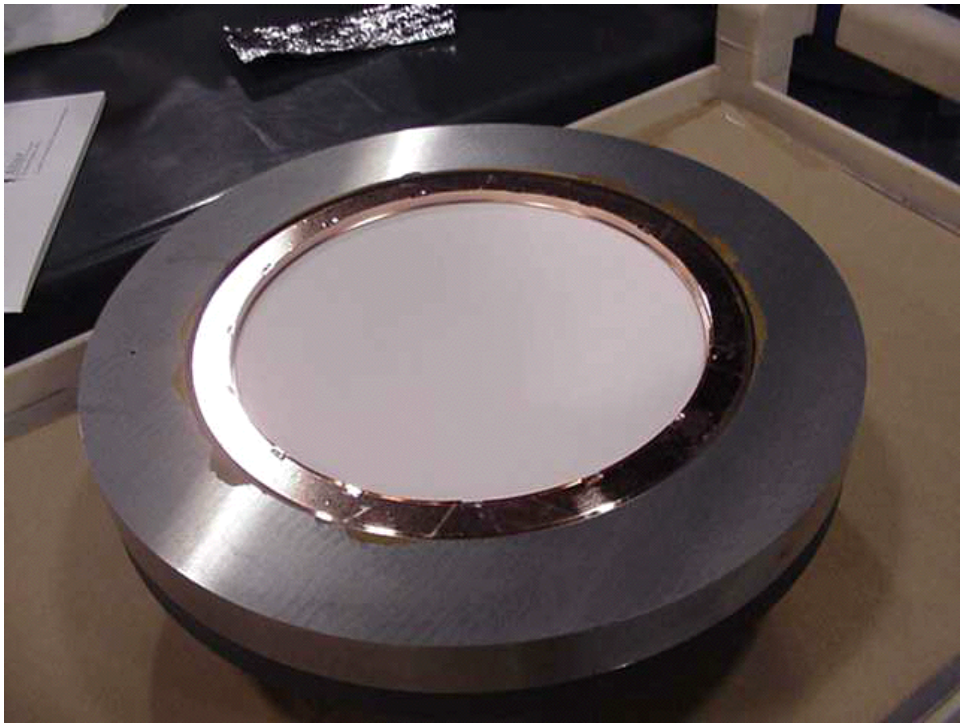

Figure 53. Fixtured window assembly ready for braze.

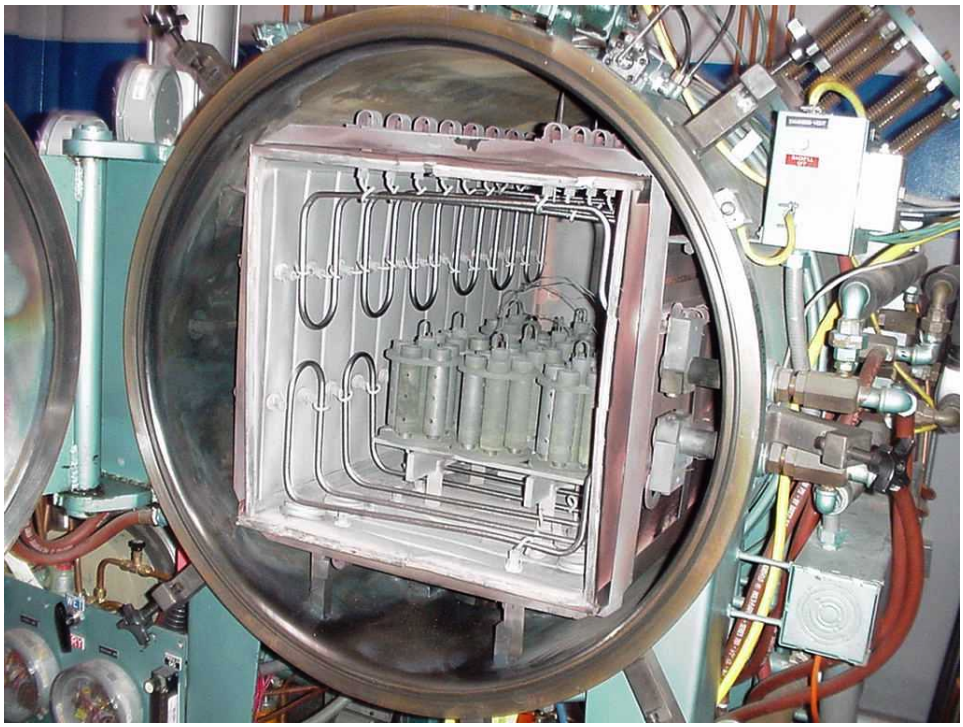

Figure 54. Square furnace with exposed heating elements.

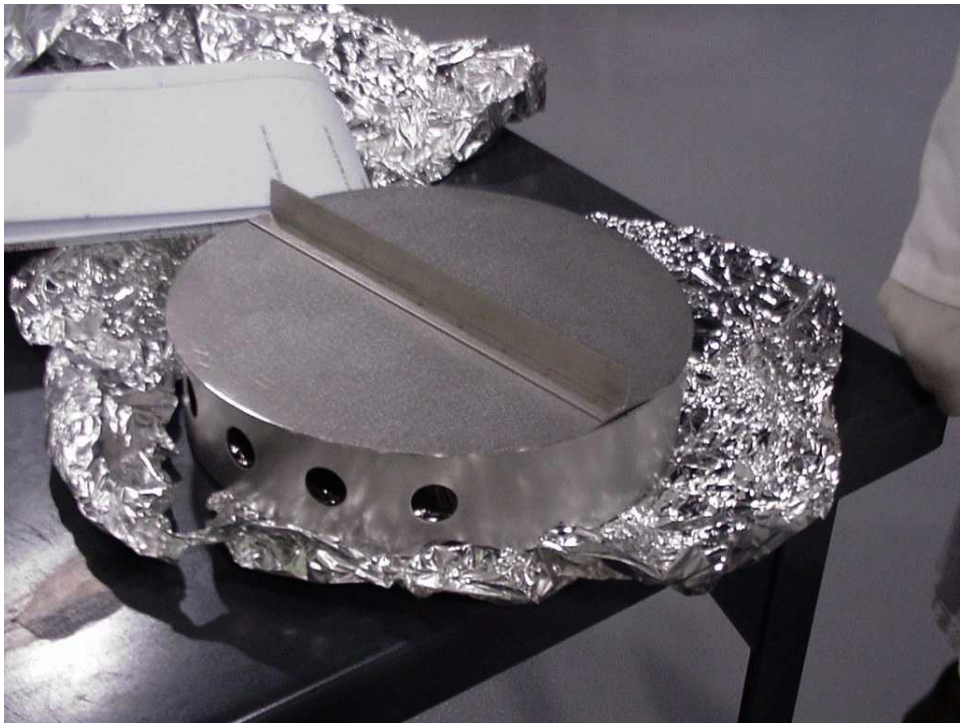

Figure 55. Sheet metal baffle used to shield braze assembly #2-5.

Figure 56. Window #2 as brazed.

The rule of thumb for a successful window braze using a ceramic of this size (O.D. approx. 7.375”) and the molybdenum ring currently being used (I.D. approx. 8.742”) is to have a total gap of 0.0250-0.0265”. The gap between the alumina and the stainless steel ring should be about 0.010” and the gap between the stainless steel and molybdenum ring should be about 0.015”. This rule of thumb, developed by simulation and experiment, appears to work well if the gaps are fairly well balanced in this proportion. Aiming for this total gap value at room temperature should give a 0.002-0.003” gap between the alumina and stainless steel ring at the 1025°C brazing temperature. Table 8 shows the dimensions of the first 5 brazes.

From the first ring test onwards the inner diameter of the molybdenum ring expanded with each cycle, possibly due to densification of the material in the area of contact. The ring grew 0.001-0.002” with each of the first three bimetallic ring tests. After a few cycles the ring appeared to stabilize. Table 9 and figure 57 show how the ring grew after each furnace run. The ANSYS analysis, figure 58, predicted the peak stresses in the molybdenum ring to be on the order of 74MPa, far below the expected 160MPa yield of molybdenum at 1000°C.

We experienced some problems with copper plating of the rings. We saw occasional blistering during the wet-hydrogen firing and some of the rings were damaged by etching when cleaning acid became trapped behind some loose masking, figure 59.

Table 8. Dimensions of the first 5 braze assemblies.

	#1 actual	#2 actual	#3 actual	#4 actual	#5 actual
Moly ID"	8.7411	8.7417	8.7417	8.7420	8.7407
Stainless OD"shim incl.	8.7100	8.7140	8.7140	8.7070	8.714
Stainless ID"	7.3945	7.3990	7.3990	7.3917	7.3990
Window D"	7.3756	7.3754	7.3754	7.3763	7.3753
Gap A-S	0.0094	0.0118	0.0118	0.0077	0.0118
Gap S-M	0.0155	0.0139	0.0139	0.0175	0.0133
Total Gap cold	0.0250	0.0257	0.0257	0.0252	0.0252
Estimated Gap at Temp	0.0017	0.0022	0.0022	0.0020	0.0020

Table 9. ID of molybdenum keeper ring.

date	cycle#	half-height	average	OD
31-Jan	0-initial	8.7343	8.7343	12.0520
7-Feb	1-ring test	8.7354	8.7355	
6-Apr	2-ring test	8.7355	8.7355	
11-Apr	3-ring test	8.7370	8.7371	
27-Apr	4-braze 1	8.7372	8.7372	12.0339
15-May	5-braze 2	8.7407	8.7407	12.0367
18-Aug	6-braze 3	8.7405	8.7405	12.0368
26-Sep	7-braze 4	8.7407	8.7408	12.0374
31-Oct	8-braze 5	8.7412	8.7412	12.0372

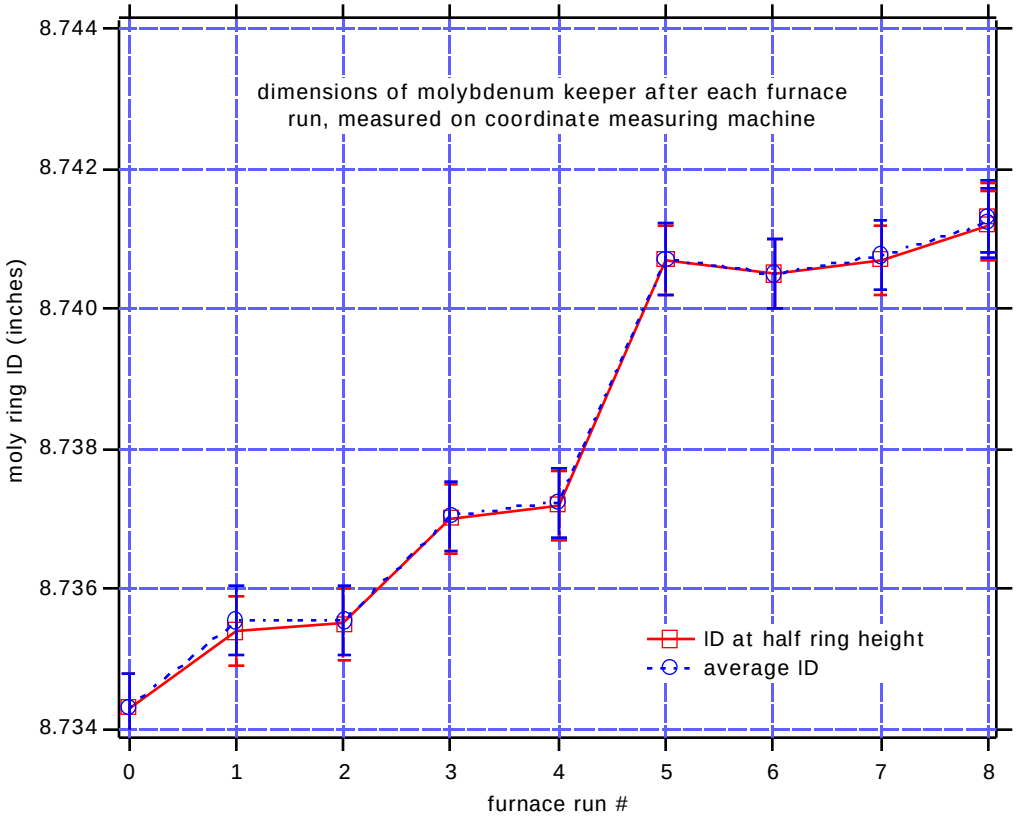

Figure 57. ID of molybdenum keeper ring after each furnace run.

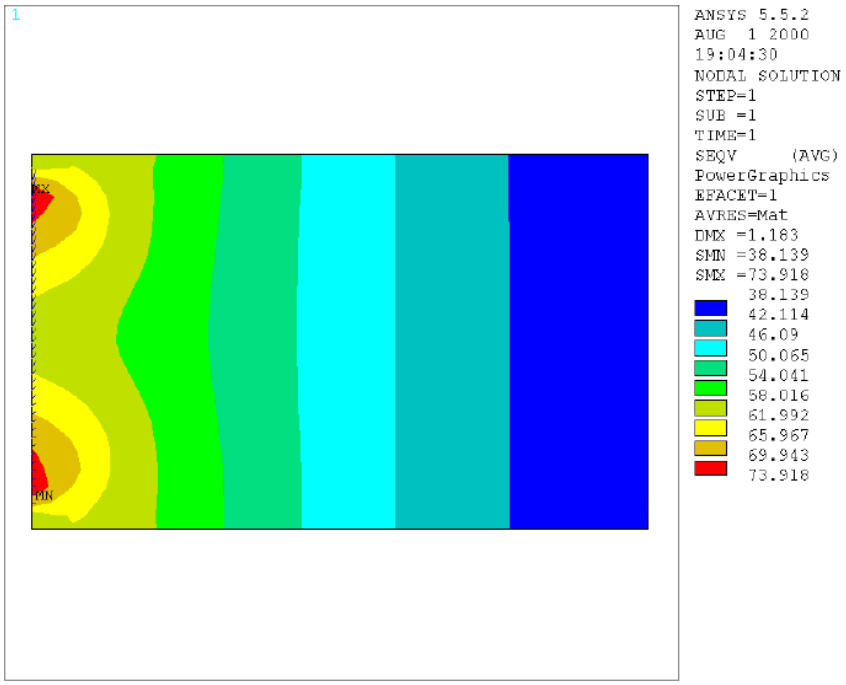

Figure 58. Stresses in the molybdenum ring at brazing temperature.

Figure 59. Etching damage in the stainless steel ring.

After brazing the frequency of the windows was once again checked in the cold-test fixture. The frequencies were consistently slightly lower than expected, although well within an acceptable range for high power testing. The final frequency determination was taken as the average of several measurements. Shims were used to adjust the length of the iris to optimize the frequency prior to final machining. The measurement proved to be insensitive to whether the shims were placed above or below the flange.

Figure 60 shows the reflection measurement of window #2, the first good window, which is slightly lower than the design frequency. Despite the frequency offset the match at 700 MHz is almost -35dB (the best match is almost -47 dB). Figure 61 shows how the match frequency varies with iris thickness as spacers are inserted to raise the window or the clamping ring.

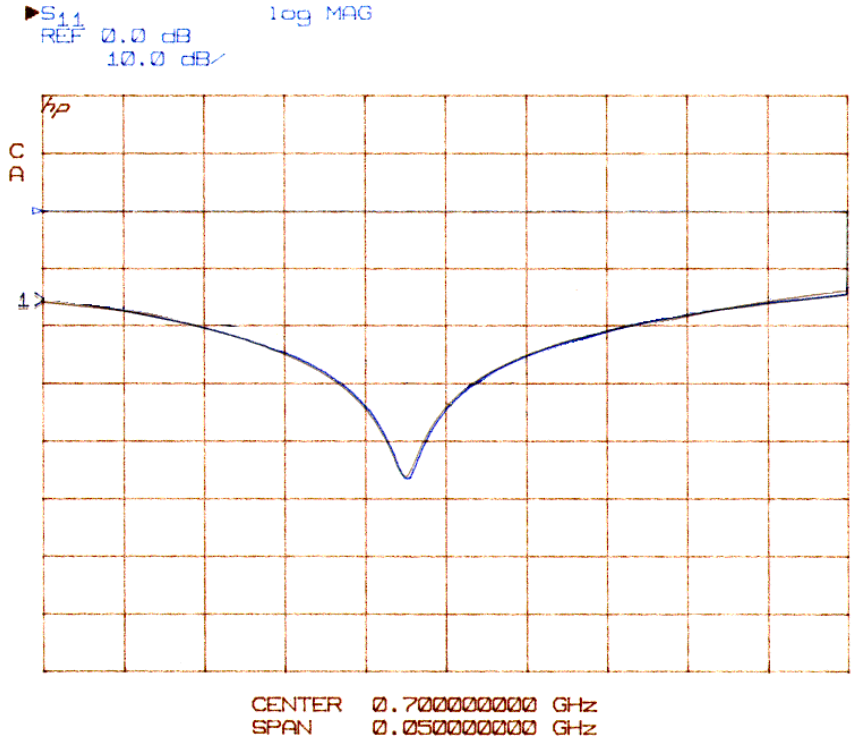

Figure 60. Window #2 as brazed (5 spacers underneath).

The graph shows four data points at each height; two reflection measurements and two in transmission (all using TRL-type calibration), along with the average. The average value seems to vary as expected with thickness, the deviation of individual data points gives an idea of the measurement uncertainty. Note that even at the full height the frequency does not quite reach the ideal value (700 MHz) expected from previous cold-test measurements. This could

easily be corrected in series production by a small change in the ceramic thickness.

Window #3 could not be cold-tested after brazing because in this furnace run the atmosphere dried out, the braze material ran and the molybdenum buttons used to support the stainless ring became brazed to the underside of the stainless ring. Window #4 showed a similarly good match to window #2 at full height, also at slightly lower frequency. Window #5 was measured quickly before the windows were dispatched to the machine shop for final machining. The frequency was acceptable although also on the low side.

The frequencies of windows 2 through 5 were very consistent and these all used ceramics from the same batch. A small thickness adjustment would be appropriate for future ceramics from the same batch.

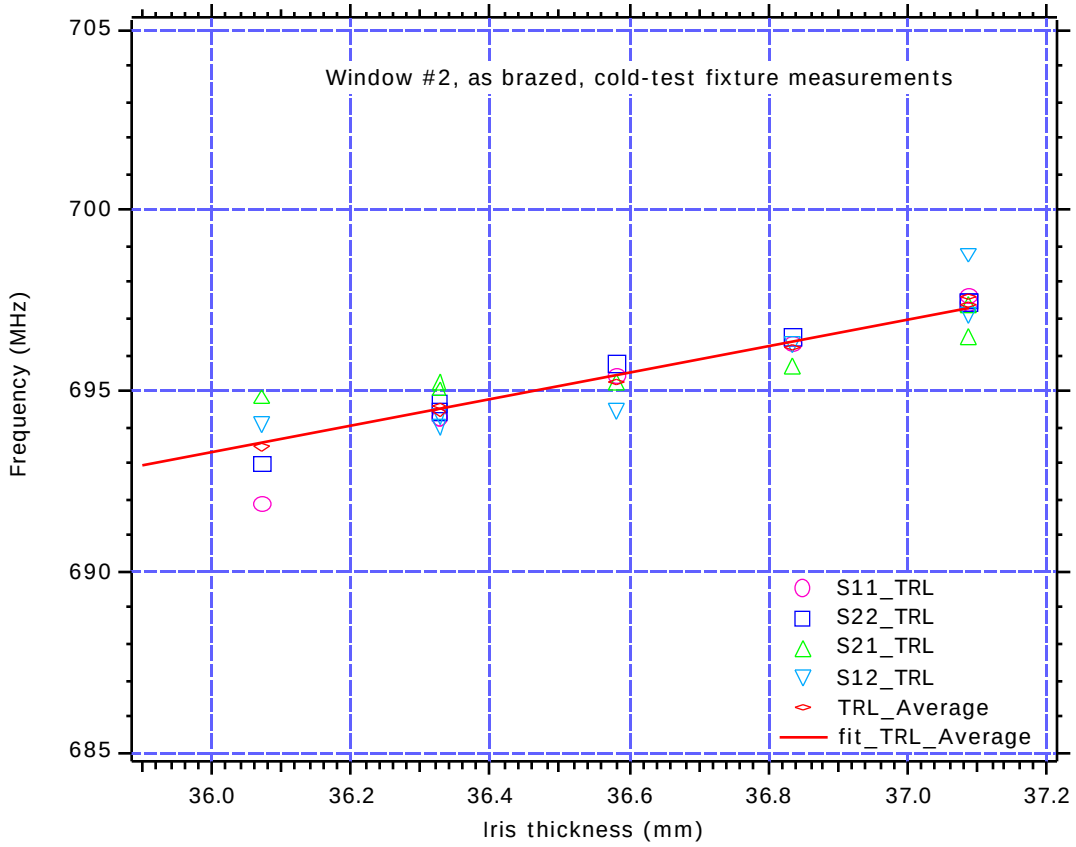

Figure 61. Window #2, frequency dependence on iris thickness.

After brazing and leak checking, the windows were machined to final dimensions. At this point they were considered clean assemblies and were handled only with lint-free gloves and only alcohol was used as a cutting fluid/coolant. The knife edge was cut first, using the cooling channel holes as a reference to gauge the

center of the cooling ring. Finally the copper layer on the air side surface was faced off to provide the final thickness.

The first window to be cut to final size, window #4 was fitted to the real spool box with the customized waveguide spacer and torqued down using a spare RF gasket, see figure 62. This was the first frequency measurement of the final configuration. The match was good (better than -47 dB) and the frequency was 697 MHz (0.4% low), see figure 63. The match at 700 MHz was about -33 dB, which was acceptable for high power testing. The other windows were also tested before shipment. Window #1, the cracked window, was also tested in the spool to add a further data point. Ironically it had the closest frequency and best match at 700 MHz. The results are summarized in table 10. The average frequency from all the reflection measurements of the first 5 windows was 696.625 MHz, which is 3.375 MHz below the desired operating frequency. This would require a 0.169 mm (0.0066") reduction in the ceramic thickness to correct for future windows and a further 0.702mm (0.0276") to tune the window up to 714 MHz for NLC. This would make the final thicknesses 11.31 mm (0.4454") and 10.78 mm (0.4244") respectively. The measurements are summarized in table 10.

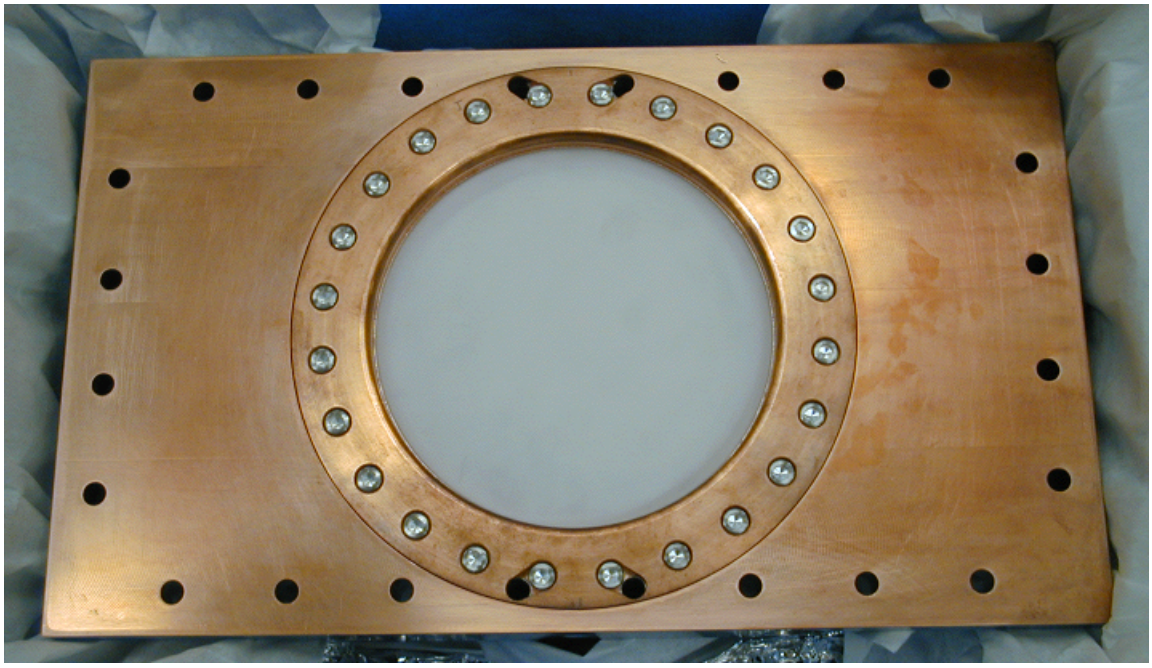

Figure 62. Finished window in spool for final frequency check.

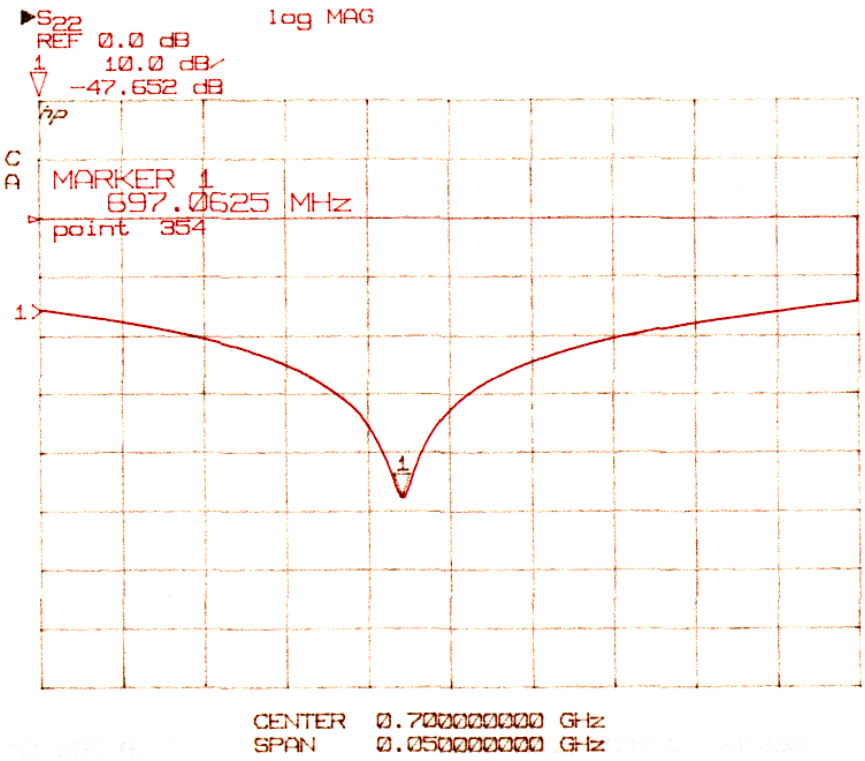

Figure 63. Window #4, final frequency measurement in spool.

Table 10. Summary of final frequency measurements.

window#	final freq S_{11} (MHz)	match S_{11} dB	S_{11}@ 700 MHz, dB	final freq S_{22} (MHz)	match S_{22} dB	S_{22}@ 700 MHz, dB
1	697.8125	-43.148	-35	697.5625	-50.368	-34
2	696.1250	-48.437	-30.618	695.8125	-53.781	-29.777
3	696.2500	-49.506	-31.086	696.0000	-43.326	-30.16
4	n.m.	n.m.	n.m.	697.0625	-47.652	-33
5	696.6875	-35.23	-30.34	696.3125	-37.813	-30.061
average	696.7188	-44.0803	-31.7610	696.5500	-46.5880	-31.3996
average of all meas.	696.6250	-45.4734	-31.5602			

(n.m.= not measured)

5.5 First prototype tests

The windows were titanium nitride coated with approximately $6x10^{15}$ atoms/cm^2 and the vacuum chamber assembly was baked to over 150°C before high-power testing. Only two of the four windows have been tested so far, but preliminary results are good [10]. The windows were tested in transmission at LANL. The windows conditioned fairly quickly with moderate outgassing at each new power level. The full power of the test stand was reached within 20 hours of processing, corresponding to just over 800 kW CW forward power, see figure 64. The power density in the ceramic is three times

higher than the PEP-II windows. The windows were operated at between 750 and 800 kW for about 8 hours before the test was terminated. The window temperatures reached equilibrium after about an hour, see figure 65, and the chamber vacuum stabilized at about $8x10^{-8}$ Torr at full power. There were a number of arcs and vacuum bursts during processing, possibly because of the somewhat aggressive schedule dictated by the limited duration of the test. However after these events the vacuum recovered quickly and there was no glowing, indicating that the TiN coating was effective.

Lifetime testing of the first pair of windows is presently underway in the LEDA facility at Los Alamos.

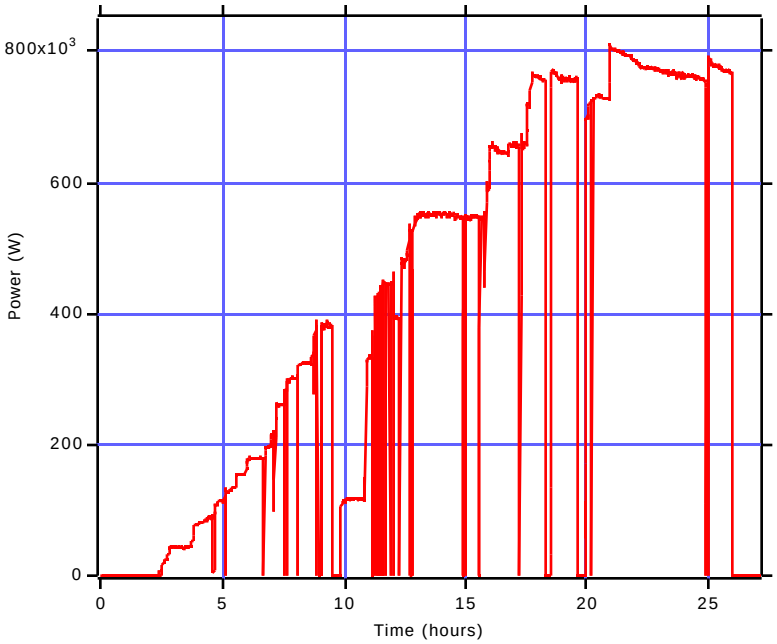

Figure 64. RF power during preliminary test.

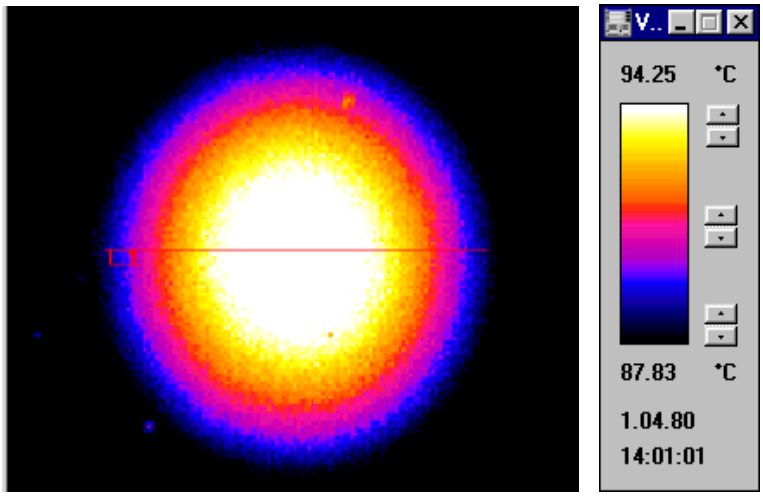

Figure 65. Window IR image at 770 kW.

6 Tuners

It is proposed to use two tuners in each cavity, with one fixed and one movable. The fixed tuner will be a simple plunger and will be used to correct for manufacturing variations such as weld shrinkage in the post-tuning e-beam welding. It will also allow the "home" position of the movable tuner to be adjusted if this is desirable for HOM tuning or to avoid tuner resonances. The movable tuner is proposed to be a simple plunger with a motorized bellows actuator, see figure 66. An important question is whether spring finger contacts are required to prevent RF heating of the tuner bellows. Careful analysis of the ALS 1.5 GHz cavities and arrangement of the tuner resonances to avoid all RF harmonics has allowed operation without spring fingers. If required fingers could be placed in the spacer ring between the cavity and the bellows. If fingers are found to be necessary it is proposed to use the same silver coated Glidcop fingers and rhodium plated tuner combination used in PEP-II [12]. The tuner plungers will be exposed to high surface currents when inserted into the cavity so they will be well cooled. Figure 67 shows a view of the proposed NLC tuner in which the spiral cooling channel is visible.

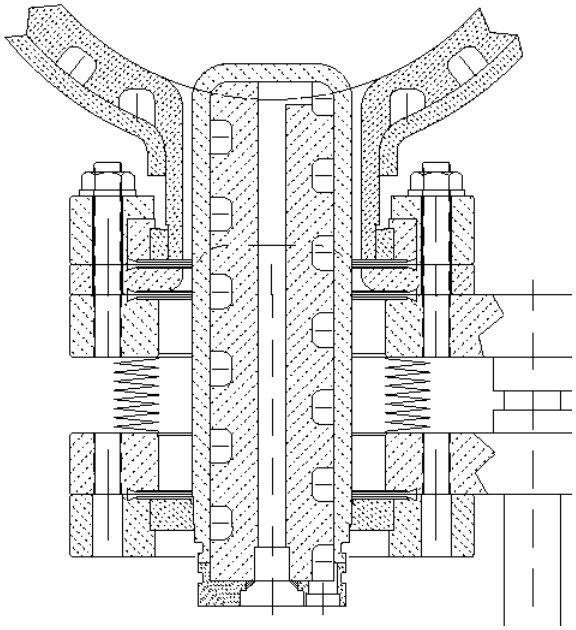

Figure 66. NLC tuner concept based on ALS design.

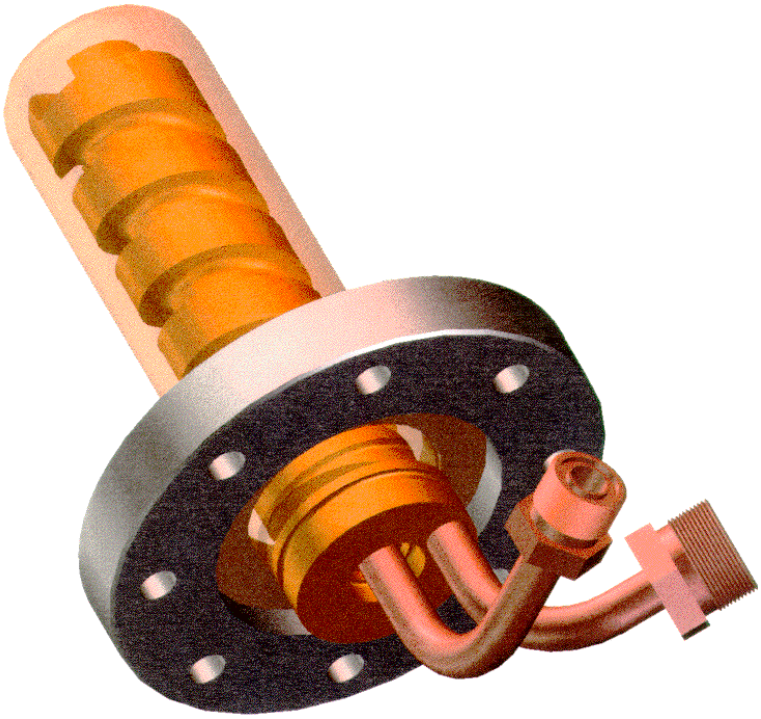

Figure 67. Tuner plunger with spiral cooling channel.

6.1 Tuning range

The tuner proposed is simply scaled from the PEP-II cavity. The plunger diameter is approximately 66.7 mm and the gap between it and the port wall is about 4.5 mm. Figures 68a and b show the 3D MAFIA mesh used for the calculations. Figures 69a and b show the electric and magnetic field vectors for the fundamental mode. Figure 70 shows the longitudinal electric field on axis. Note that it is perturbed by the HOM ports on one side of the cavity. Several runs were made for different tuner positions to calculate the frequency sensitivity and losses on the tuner. The tuner plunger was moved up or down by a whole number of mesh planes to minimize effects of the mesh geometry. The calculations show that the frequency range of a single tuner is from -350 KHz fully extracted to + 1.17 MHz 2 cm inserted, figure 71. This gives about 1.5 MHz of tuning range for each tuner which is sufficient to detune the cavity up or down one half of the revolution frequency (1.37 MHz PDR, 1.01 MHz DR), for parking purposes.

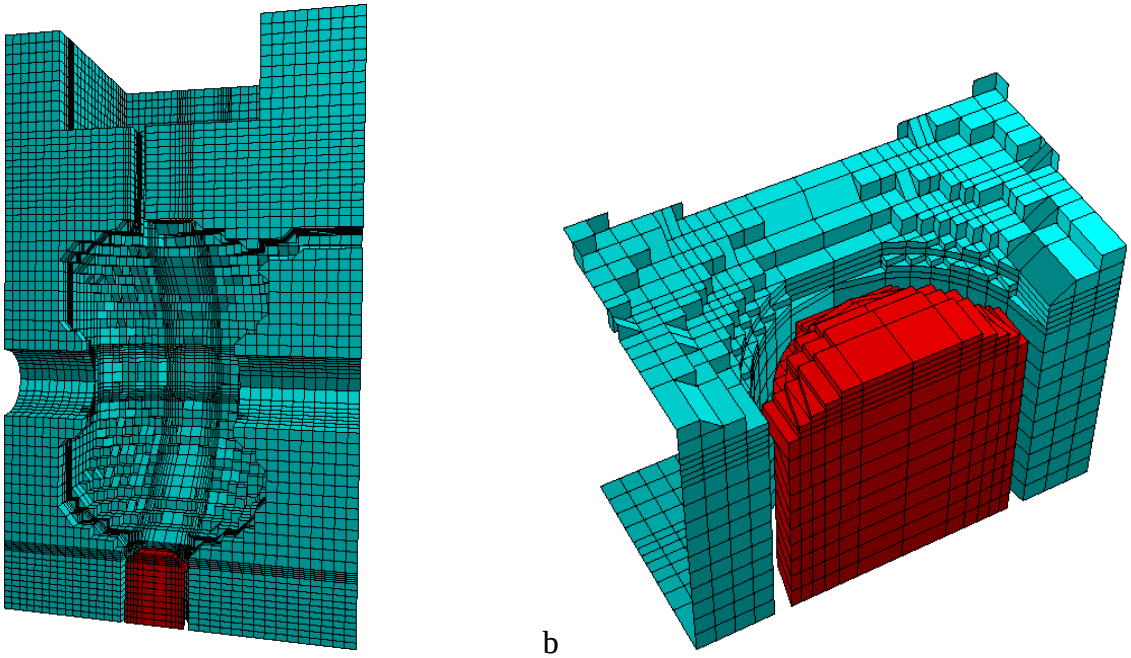

a b

Figure 68. 3D MAFIA model including a single tuner port.

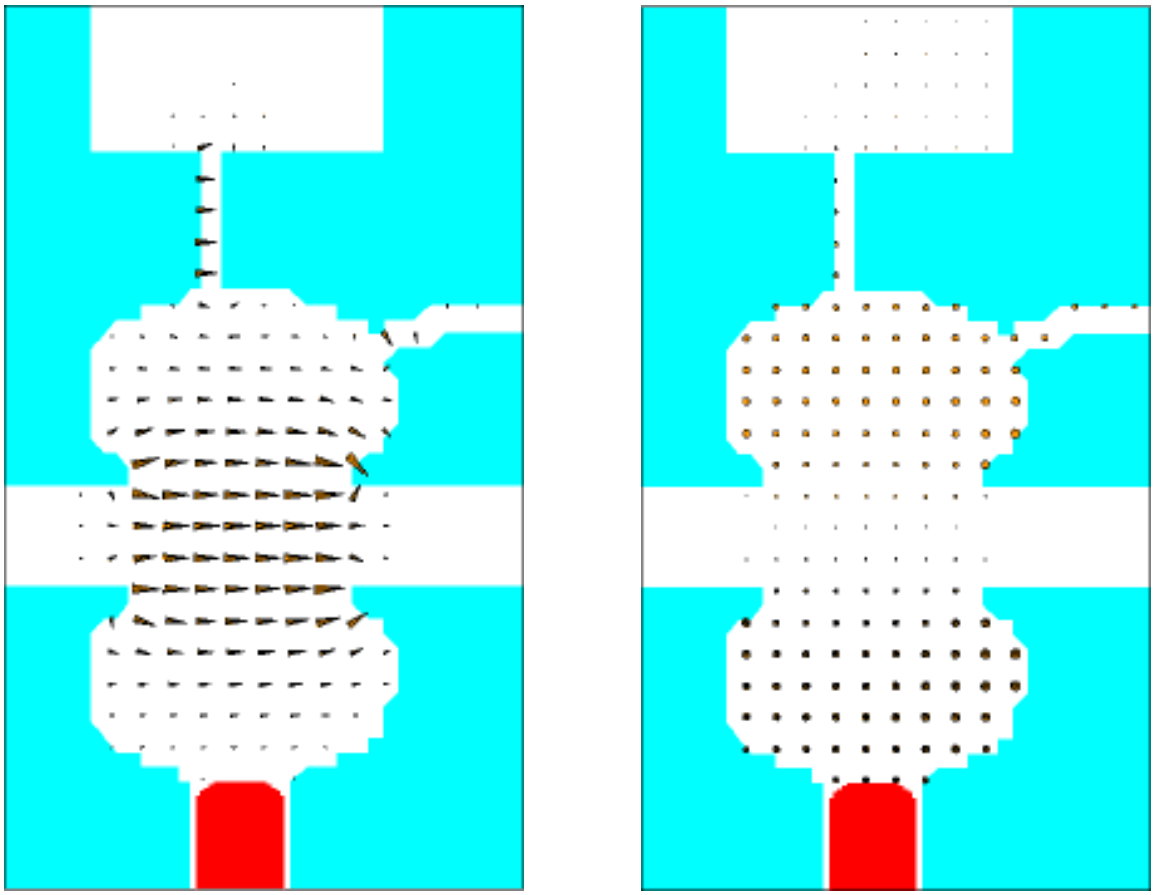

a b

Figure 69. Electric and magnetic field vectors for fundamental mode.

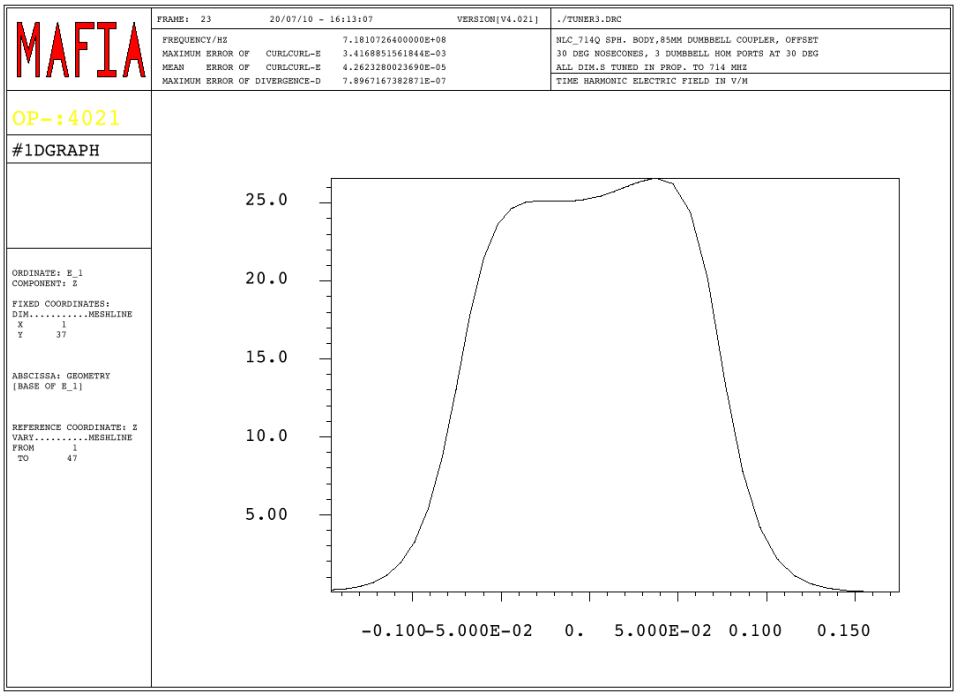

Figure 70. Longitudinal electric field on axis.

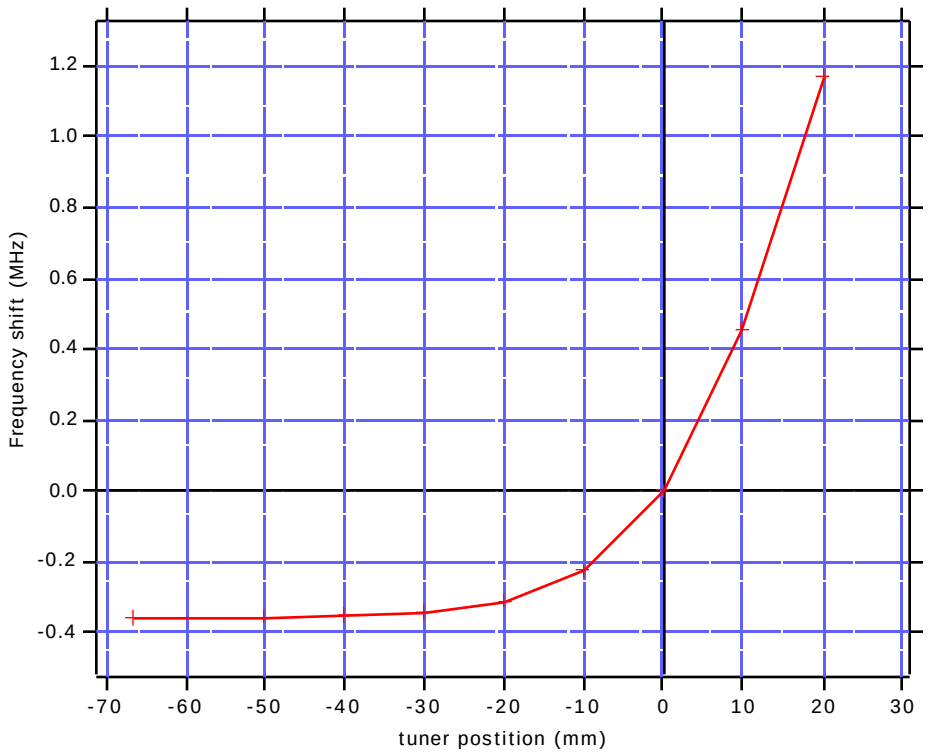

Figure 71. Calculated tuner range for one tuner (0 = flush).

6.2 Spring finger placement

The runs also give the frequency of the first coaxial mode in the tuner, figure 72, assuming that the port is shorted by a ring of spring fingers at the position of the flange. Figure 73 shows how the frequency of this mode varies with tuner position. Note that over the expected tuning range the coaxial resonance is safely between the fundamental frequency and the first beam harmonic so resonant heating should not be a problem for uniform or near-uniform fills. However if a 357 MHz bunch spacing is used the coaxial mode could be excited at 1071 MHz at close to the flush tuner position. These details and the locations of higher order resonances will be studied more closely before the final position of the spring fingers is determined, if any are needed at all.

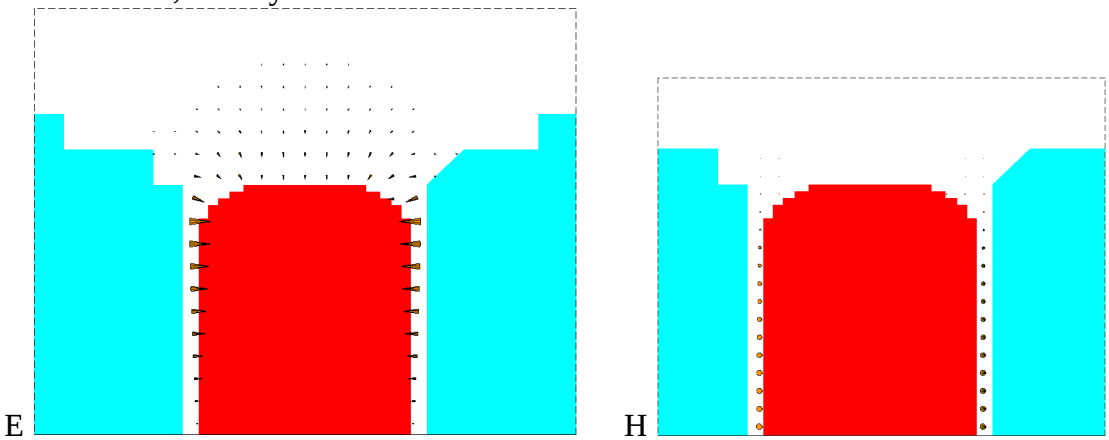

Figure 72. MAFIA solution for first coaxial resonance in tuner.

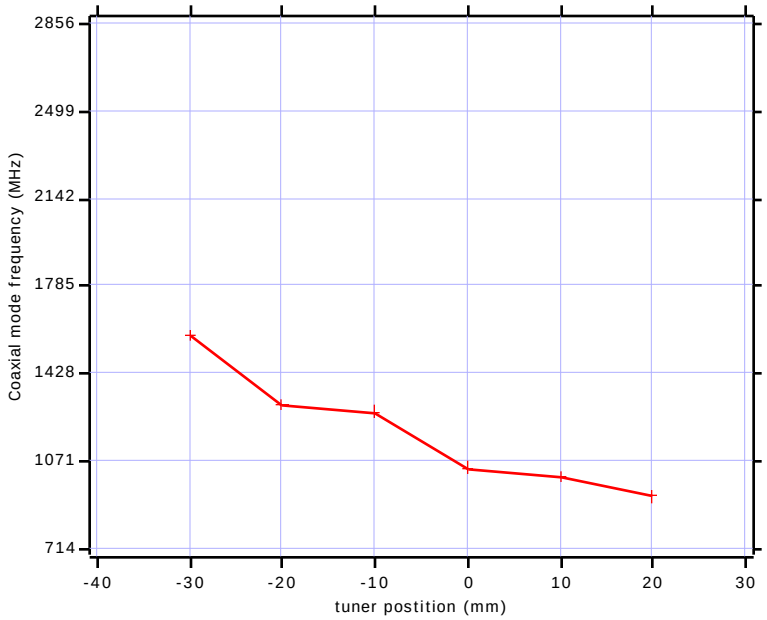

Figure 73. Frequency of first coaxial resonance in tuner vs position.

6.3 Wall currents

Figure 74 shows the calculated losses on the tuner plunger and figure 75 shows the current density on the end plane of the model, where the tuner fingers might be. Note that the tuner plunger is primarily heated on the end where it is exposed to the full cavity fields. There is some enhancement on the corner of the tuner and of the tuner port (not shown), and these will be given a generous radius. The current at the end of the tuner port is the sum of the evanescent mode penetrating into the gap plus the current in the coaxial mode caused by the longitudinal asymmetry of the cavity. Figure 76 shows how the cavity Q and the shunt impedance change with tuner position. Clearly the R/Q does not change much and the increased losses on the tuner at large penetrations causes the slight reduction in shunt impedance. Figure 77 shows how the power on the tuner and the current in the fingers change with tuner position. At 20 mm penetration the losses on the tuner total about 1 kW or about 2.5 % of the total.

Figures 78 through 81 show a similar analysis in ANSYS for the tuner flush with the cavity wall. The magnetic field distribution at the shorted end of the tuner port shows the same distribution as the MAFIA models. The maximum H field (in line with the beam axis) corresponds to about 1214 A/m (0.5 W/cm2) at 42 kW total cavity power, while the minimum (perpendicular to the beam axis), is about 405 A/m (0.055 W/cm2). Using the same spring finger configuration as PEP-II (3 finger contacts per cm), would give a maximum current of 4 A/finger. This can be compared to an estimated maximum of 8.8A/finger in PEP-II (4.14 A/finger operating) [12].

If the power were all in the evanescent mode the azimuthal distribution of current would be approximately sinusoidal. If in the coaxial mode it should be uniform. The sinusoidal component of the actual distribution suggests about 90% of the field is from the evanescent mode, the remainder in the coaxial mode. This suggests that if resonant excitation can be avoided the current flowing in the external part of the tuner *without spring fingers* would be manageable.

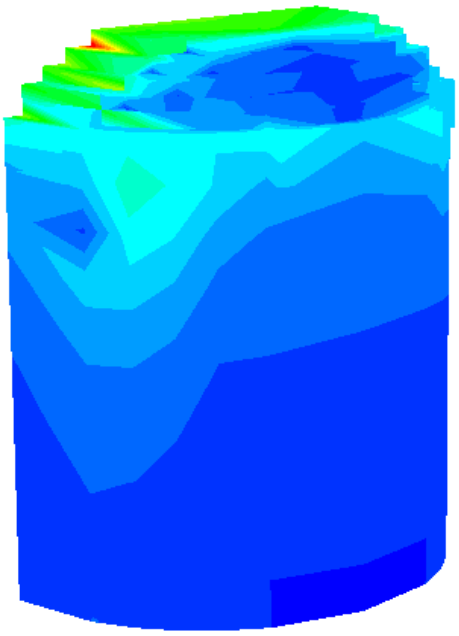

Figure 74. MAFIA calculation of wall losses on tuner plunger.

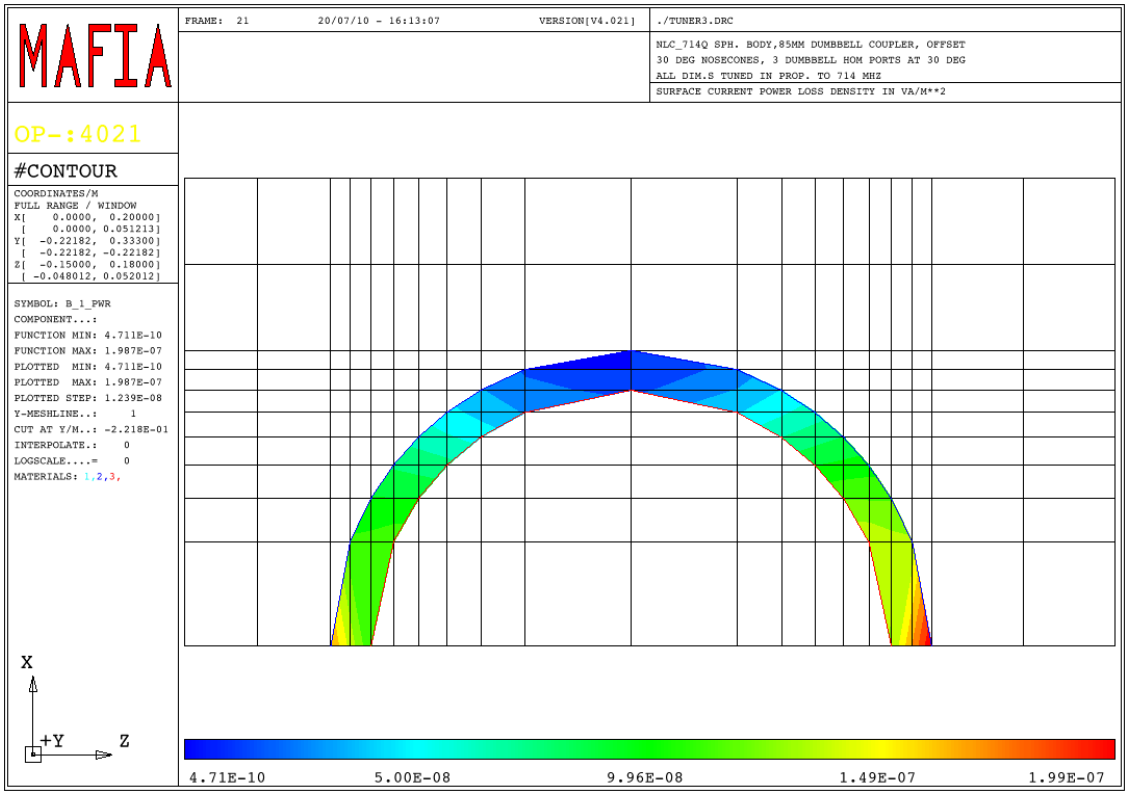

Figure 75. MAFIA calculated distribution of wall power density on end mesh plane of tuner port (arbitrary units).

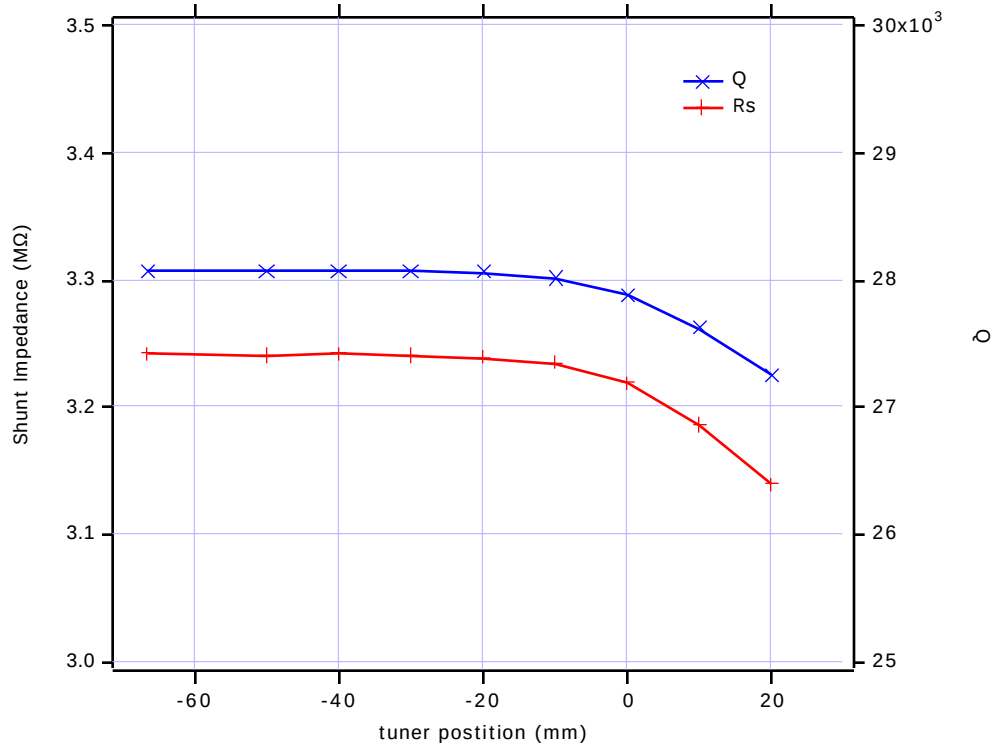

Figure 76. Change in Q and shunt impedance with tuner position.

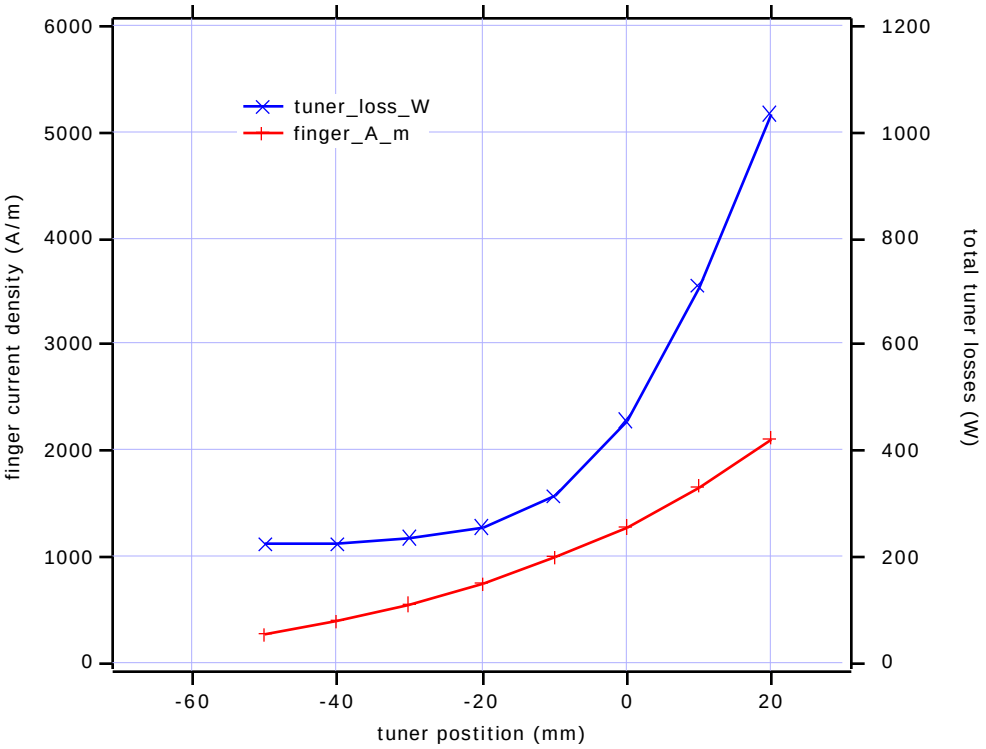

Figure 77. Change in total tuner losses and spring finger current density with tuner position.

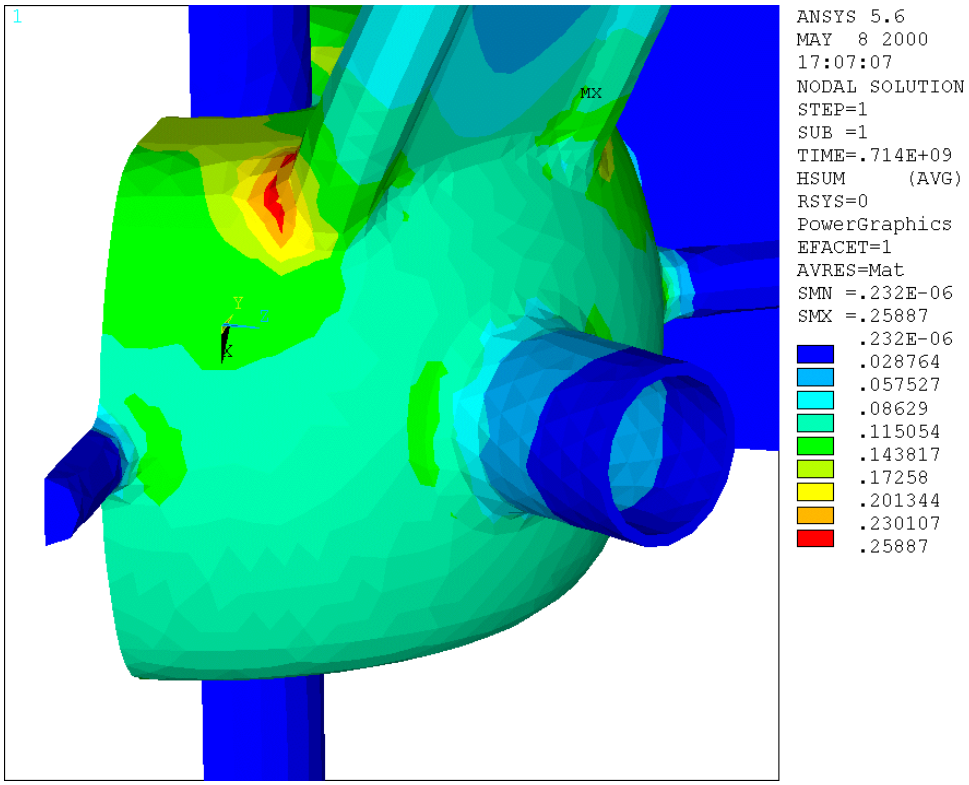

Figure 78. ANSYS calculation of surface magnetic field (arbitrary units).

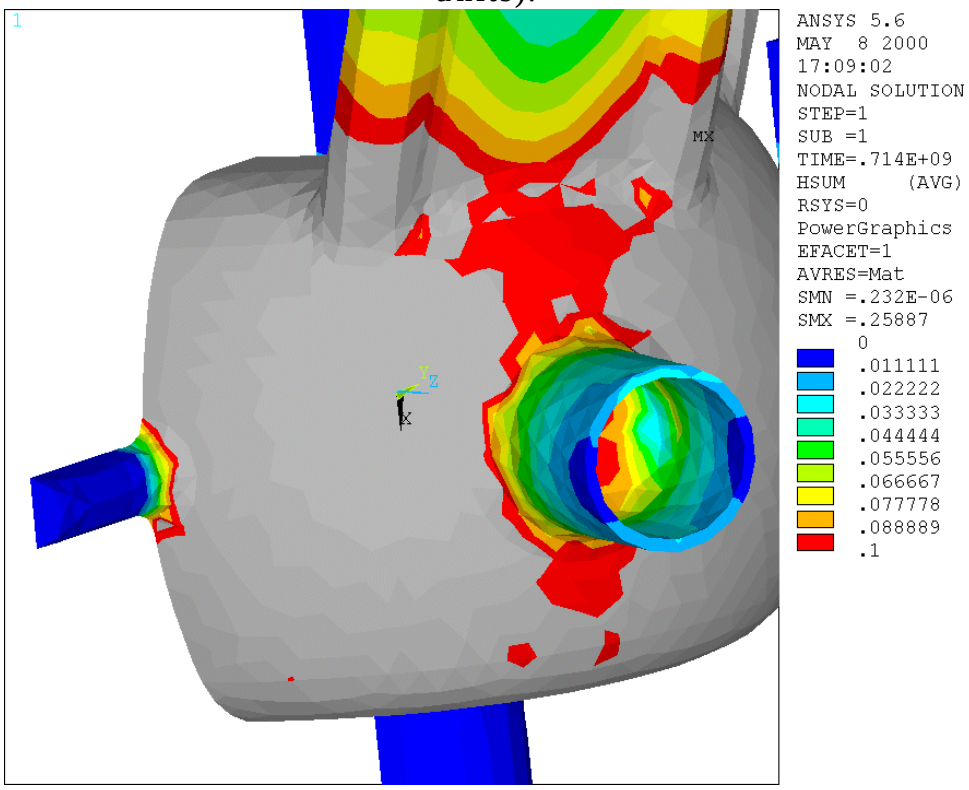

Figure 79. ANSYS calculation of surface magnetic field (arbitrary units), contours chosen to show details in the tuner port.

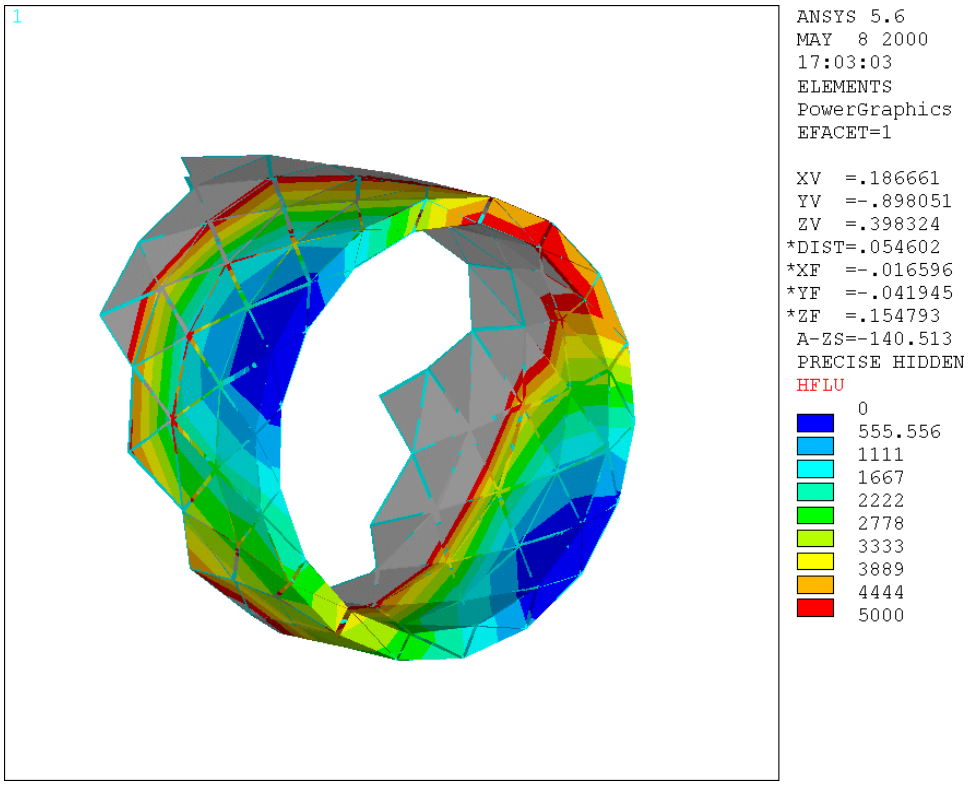

Figure 80. ANSYS calculation of surface losses normalized to 42 kW total, contours scaled to show tuner variation, close up.

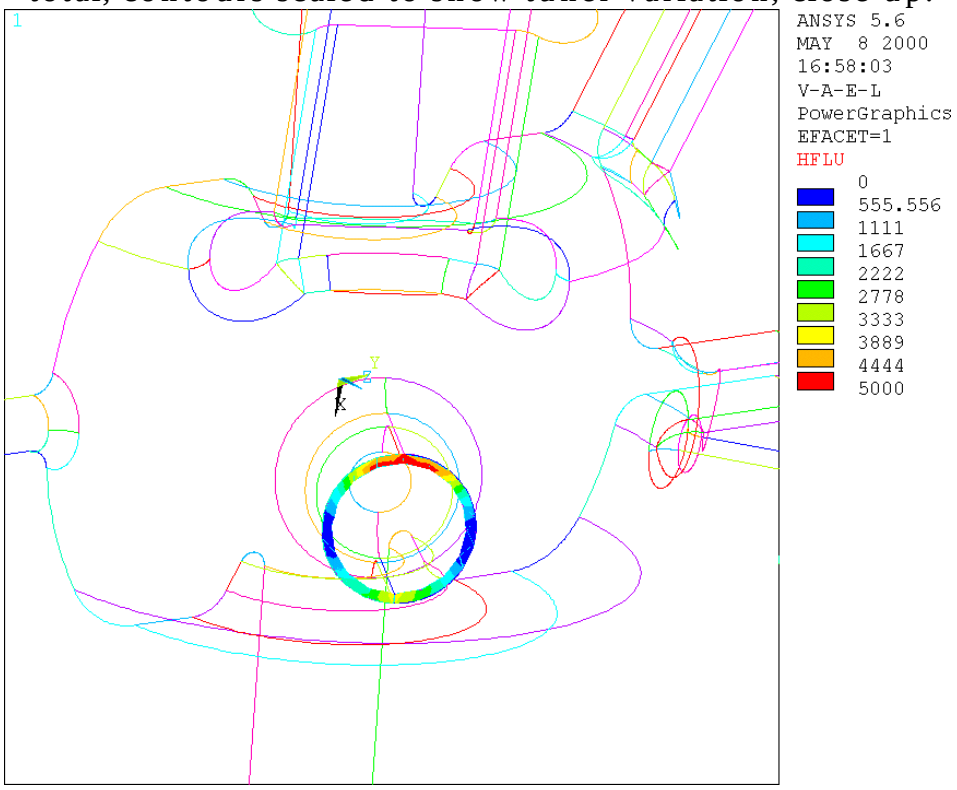

Figure 81. ANSYS calculation of surface losses normalized to 42 kW total, contours scaled to show tuner variation, close up of tuner end.

7 Options and future work

With the present damping ring lattice parameters the proposed HOM damping is adequate to supress longitudinal instabilities and keep the growth rates of transverse coupled bunch modes comparable to or less than those from the resistive wall [7]. In the pre-damping ring the present lattice requires a high RF voltage and hence more cavities and some longitudinal HOMs are therefore close to threshold or slightly above. It is hoped that continued work on the pre-damping ring lattice will restore the RF voltage requirements to the previous lower levels avoiding this problem. If this should not prove to be the case the instabilities may be controlled by a bunch-by-bunch feedback system or the HOM damping could be strengthened to further lower the residual impedance. This could be achieved by increasing the size or number of the HOM damping apertures, or moving to a different shape.

The magnitude of RF transients induced by the gaps between bunch trains is inversely proportional to the stored energy, so a low R/Q shape may be beneficial. The R/Q can be lowered by using a different shape with lower R and / or higher Q or by adding an external energy storage cavity.

For comparison we have looked at a Cornell-type cavity shape with large "fluted" beam pipes which has a low R/Q (~45 Ω) and very good HOM characteristics.

7.1 Lower HOM options

We have looked at cavities with four or six HOM waveguides instead of the nominal three see figures 82 and 83, and a different approach using much larger apertures. With four waveguides, two in the vertical orientation and two in the horizontal plane, the worst residual modes are reduced approximately 29% longitudinally and 44% in the transverse plane. Going to three waveguides on each side gives a 53% improvement longitudinally and 66% transversely, see figures 84 and 85. In both cases the longitudinal symmetry of the damping ports (compared to the three on one side of the baseline design), probably helps to maximize the damping. In previous studies making the apertures larger on only one side prompted the fields to move towards the other side of the cavity. In the four and six waveguide MAFIA models a simple circular coupler was used and an additional circular side port was added to capture the last horizontal dipole mode. This port could also be used for pumping, having a good conductance into the cavity.

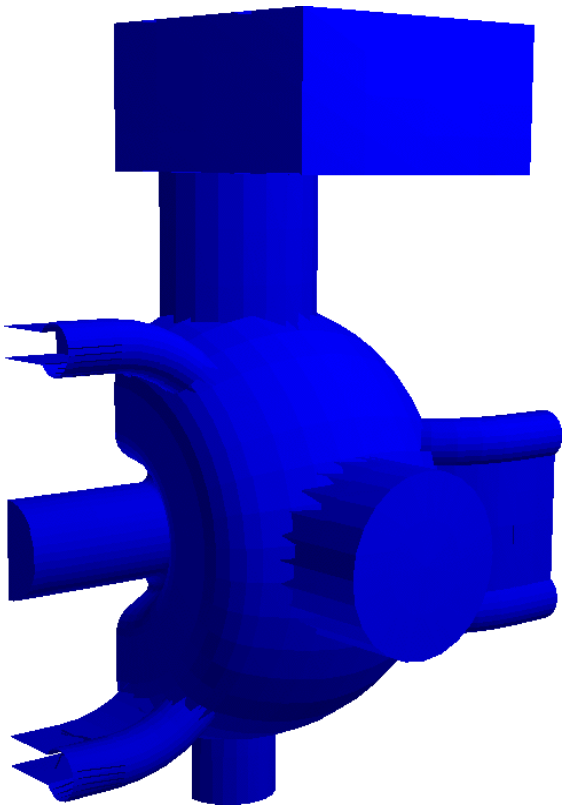

Figure 82. Four-waveguide cavity.

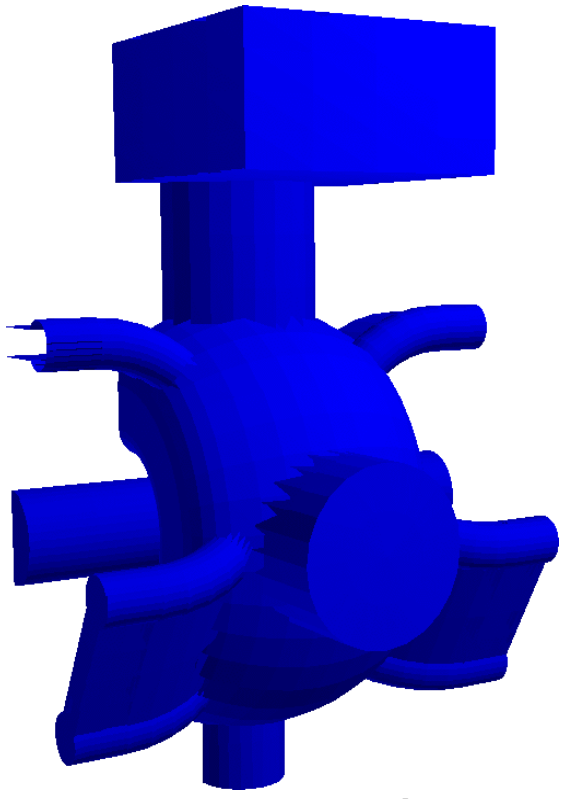

Figure 83. Six waveguide cavity.

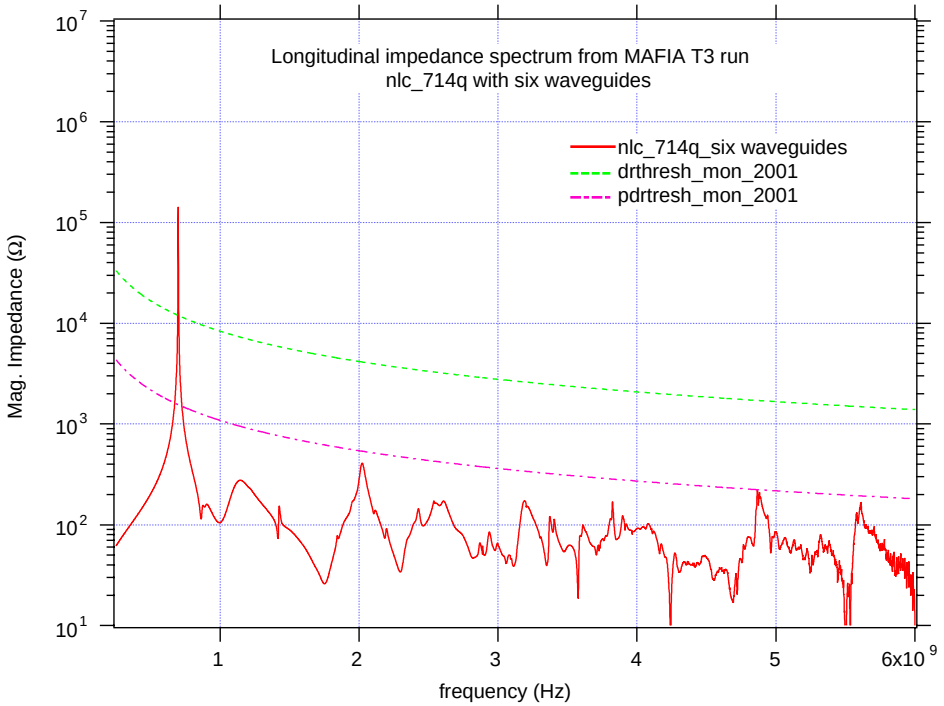

Figure 84. Longitudinal impedance of NLC type cavity with 6 HOM waveguides.

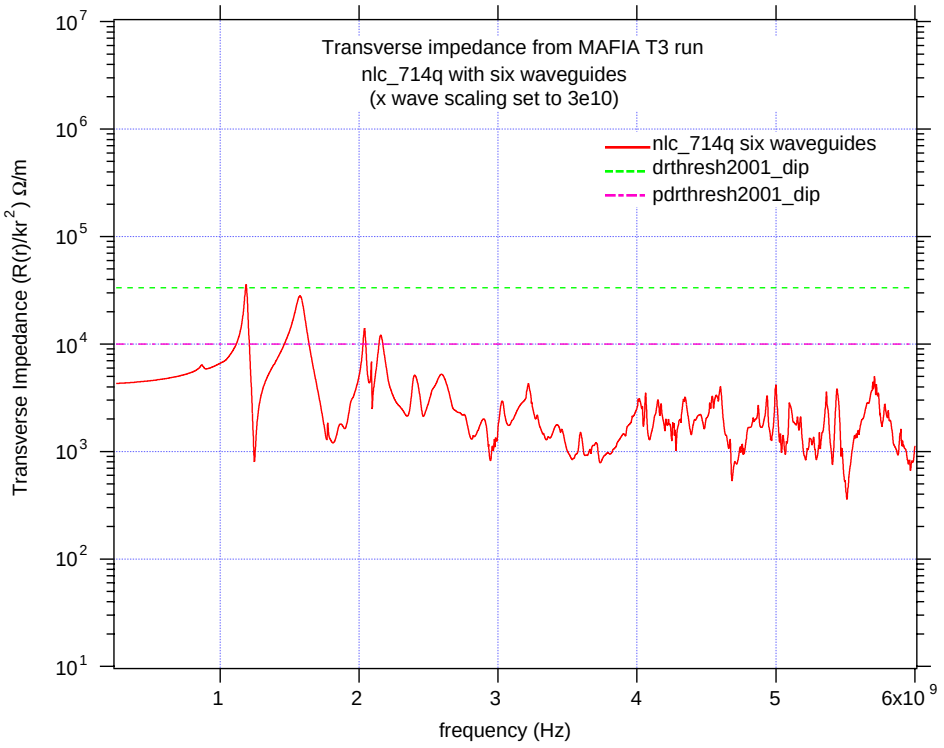

Figure 85. Transverse impedance of NLC type cavity with 6 HOM waveguides.

In order to investigate the limits of damping with increasingly large apertures a model was constructed in which the "cavity" was formed by the intersection of two circular waveguides, see figure 86. This shape also has a lower R/Q (62% of the baseline design). Due to the perturbed volume at the intersection a single mode is trapped there, below the cutoff frequency of the pipes. In order to minimize the persistent wakefield at the pipe cut-off frequency the pipes are enlarged slightly a short distance from the cavity, but not so much as to allow the fundamental mode to propagate. Small beam pipes are cut in the direction orthogonal to the plane of intesection. Figure 87 shows the electric field distribution of the trapped mode, which is similar to the accelerating mode in a normal cavity. Figures 88 and 89 show the longitudinal and transverse impedance spectra of this structure calculated in MAFIA. The highest residual impedance of this cavity is less than half the baseline design longitudinally and more than a factor of ten down transversely. This cavity would also have a lower R/Q for reduced transients. The penalty is a lower shunt impedance (55% of the baseline design), which would require a higher dissipated power. Table 11 lists the basic parameters for this cavity. The relative strengths of the residual modes in each type of cavity are summarized in tables 12 (longitudinal), and 13 (transverse).

Table 11. Parameters of "two-cylinder" cavity.

R/Q	73.6 Ω
Qo (MAFIA)	30277
Rs ($V^2/2P$)	2.229 MΩ
Rs x 80%	1.783 MΩ
V	500 kV
P	70.1 kW

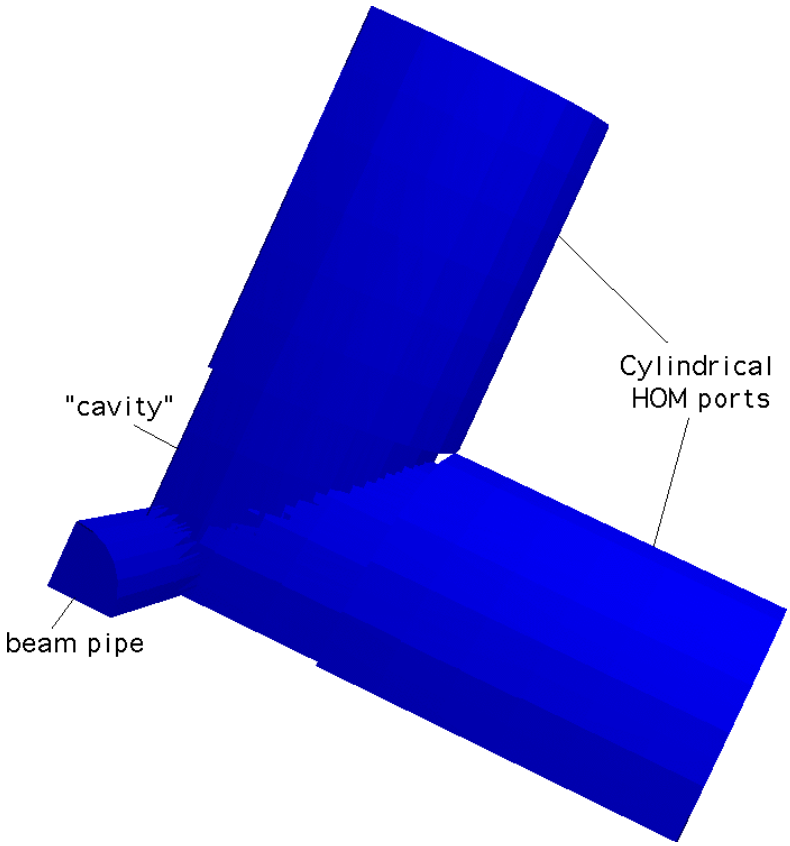

Figure 86. Simple test cavity formed by two intersecting cylinders.

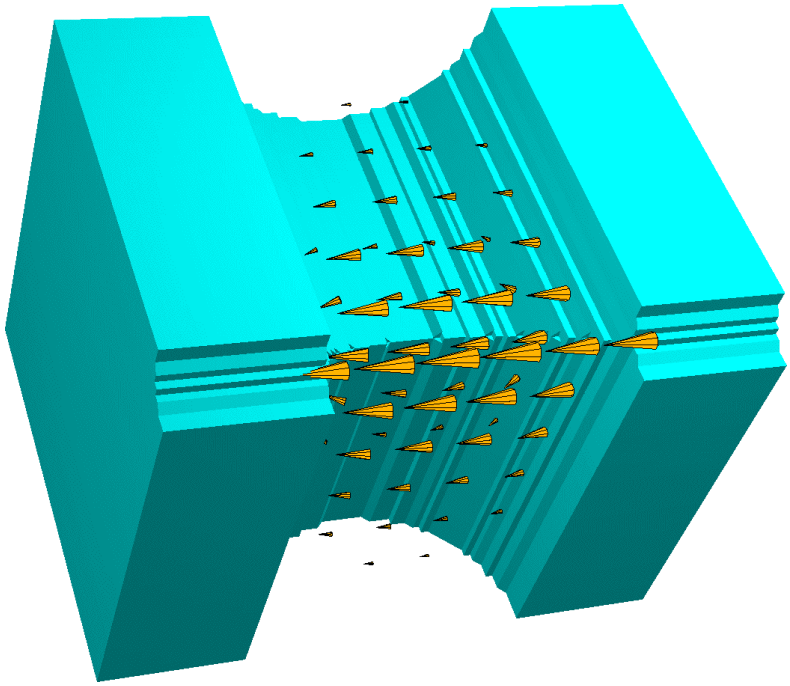

Figure 87. Electric field of fundamental trapped mode.

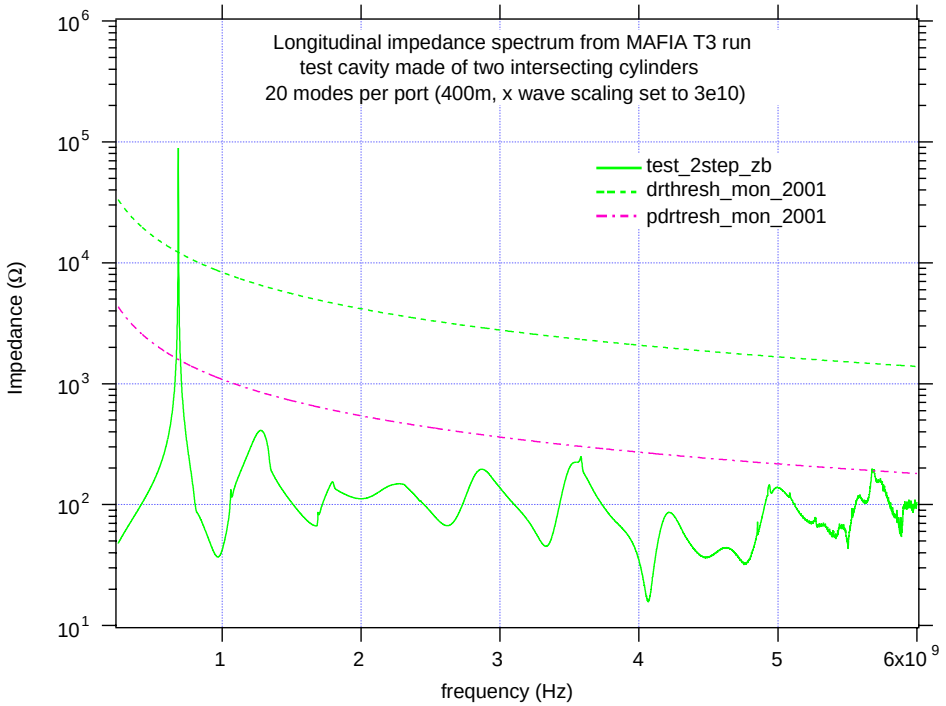

Figure 88. Longitudinal impedance spectrum of intersecting cylinders (note that the strongest residual mode may not be the one closest to threshold).

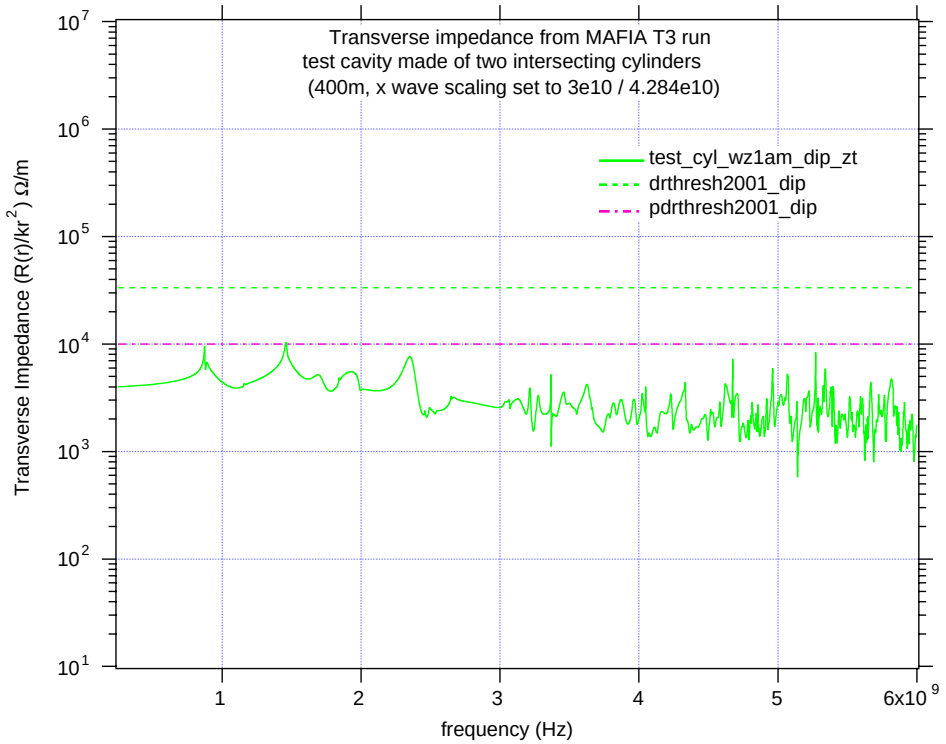

Figure 89. Transverse impedance spectrum of intersecting cylinders.

Table 12. Frequency and strength of highest remaining longitudinal modes in various cavity types.

cavity type	freq. (MHz)	highest resid. imp (Ω)	DR thresh Ω/cell	% of thresh.	PDR thresh Ω/cell (7 cells)	% of thresh.	fund. Imp** MΩ, 80% MAFIA
3wg	2026	876	4113	21%	535.9	163.5%	3.25
4wg	1892	624	4405	14%	573.8	108.7%	3.16
6wg	2022	409	4121	10%	537.0	76.2%	2.99
2cyl	1277	411	6526	6.3%	850.2	48.3%	1.78
Cornell	3016	181	2763	6.6%	840.0*	21.5%	44900†

*3 SCRF cells in PDR. **$V^2/2P$. †assuming $Qo=1x10^9$

Table 13. Frequency and strength of highest remaining transverse modes in various cavity types.

cavity type	freq. (MHz)	highest resid. imp. (kΩ/m)	DR thresh (kΩ/m/ cell)	% of DR thresh.	PDR thresh (kΩ/m /cell) (7 cells)	% of PDR thresh.	R/Q of fund. **(Ω)
3wg	2219	105	33.3	318%	10	1050%	117
4wg	1186	58.6	33.3	176%	10	586%	119
6wg	1187	35.8	33.3	107%	10	358%	119
2cyl	1458	10.3	33.3	31%	10	103%	73.6
Cornell	964.2	7.63	33.3	23%	23.3*	32.7%	44.9

*3 SCRF cells in PDR. **$V^2/2P$.

7.2 Energy storage cavities

An alternative way to lower the R/Q and increase the stored energy is to increase the Q by adding an external energy storage cavity. This has been used successfully to reduce the beam loading detuning in the KEK-B factory [13]. Figure 90 shows the KEK ARES concept in which a large energy storage cavity operating in a low-loss mode is coupled to the accelerating cavity. An intermediate coupling cavity is used to allow damping of unwanted modes (two out of the three modes close to the operating frequency have field in the coupling cell and can therefore be damped). Figure 91 shows an early model of the scheme applied to the HOM-damped choke mode cavity. A similar system (ARES-2), using a more conventional accelerating cavity, is now operating successfully in KEK-B. Figure 92 shows a full size high power cavity system.

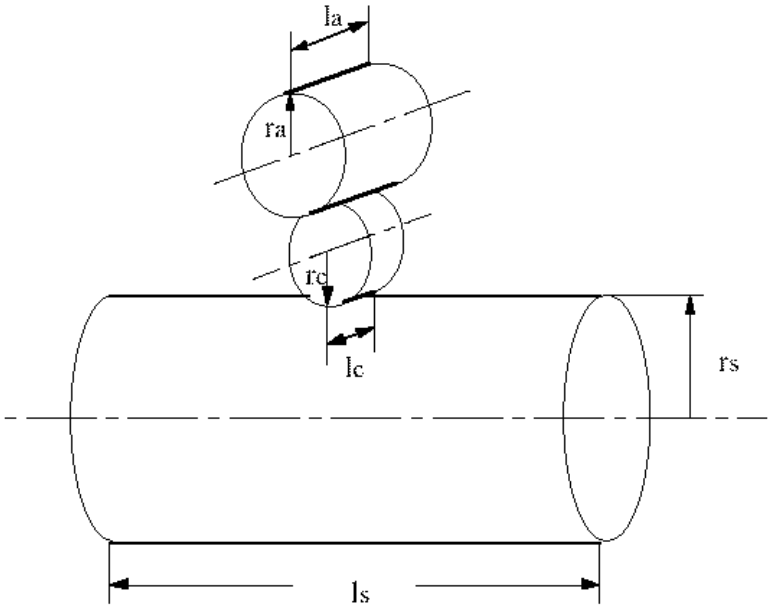

Figure 90. KEK ARES cavity concept.

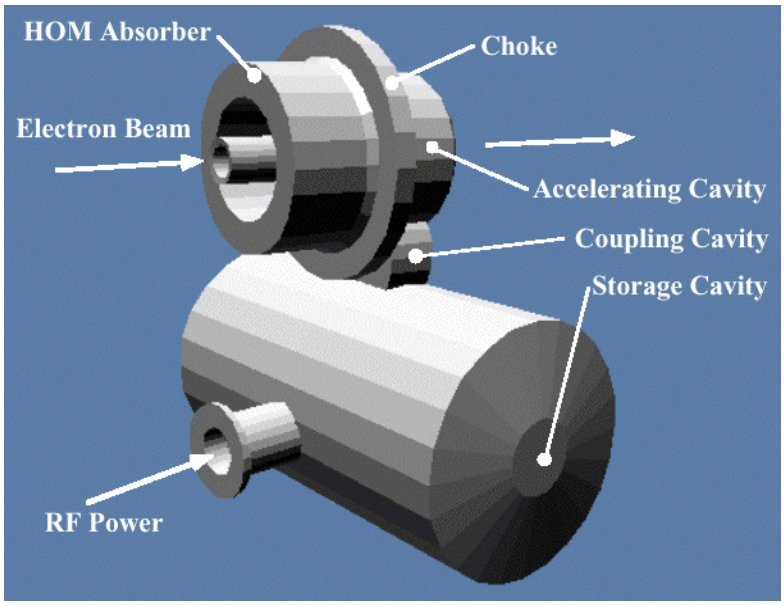

Figure 91. KEK ARES with choke mode cavity concept.

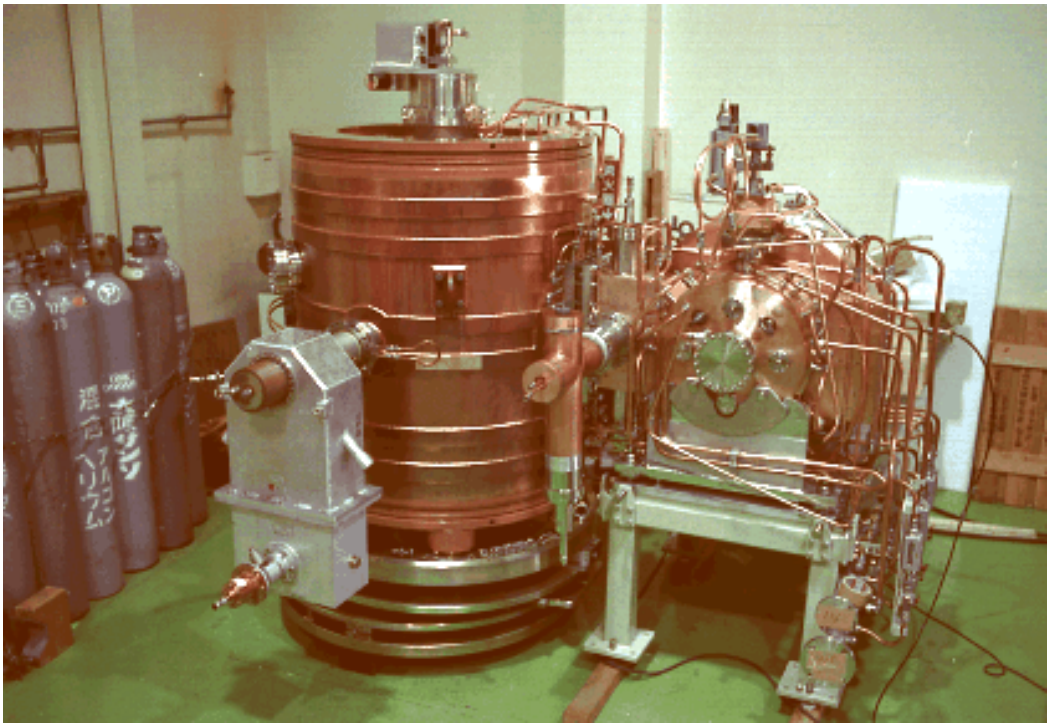

Figure 92. KEK ARES cavity system.

7.2.1 A simple 2-cavity model

In order to evaluate this concept we made a simple model using an aluminum storage cavity coupled directly to a spare 1.5 GHz cavity from the ALS third harmonic RF system. No intermediate coupling cavity was used. The storage cavity was designed to operate in the TE_{015} mode with a calculated Q of about 106,000. The same configuration was simulated in MAFIA, figure 93, and the coupling adjusted by tuning the frequency of the small cavity with one tuner. Figure 94 shows how the frequency of the accelerating cavity and energy storage cavity modes vary with tuner position. Note that there are three modes around 1.5 GHz; the accelerating cavity TM_{010} mode, and the storage cavity TE_{015} and TM_{111} modes. The latter does not interact with the accelerating cavity mode. As the cavity resonance is moved through 1.5 GHz these modes interact resulting in coupled modes in which the energy is shared between the accelerating and storage cavities. The "avoided crossing" pattern of figure 94 is typical of strongly coupled cavities. Figure 95 and 96 show the calculated Q and shunt impedance of the coupled modes as a function of tuner position. The shunt impedance is calculated using the effective voltage in the accelerating cavity and the total wall power (taking into account all symmetries). Figure 97 shows the resulting R/Q for the two modes. Clearly the energy is exchanged

between the cavities and the nature of the modes change from being separated at large tuner offsets to being coupled in the center. The R/Q can be adjusted continuously between the original accelerating cavity value (~80) down to below 10. In the middle case, where the uncoupled frequencies are approximately equal, there is strong field in both cavities. The shunt impedance is aproximately the same as the natural cavity impedance but the Q is at least double. The R/Q can thus be lowered by a factor of two with almost no power penalty and by larger factors with less penalty than using an inherently low R/Q shape.

The calculated shunt impedance of the cavity branch with the tuner out (-10mm) does not seem to be as high as with the tuner in (+10mm). This disparity is not understood, it might be due to an error in the MAFIA analysis or perhaps the influence of another nearby mode.

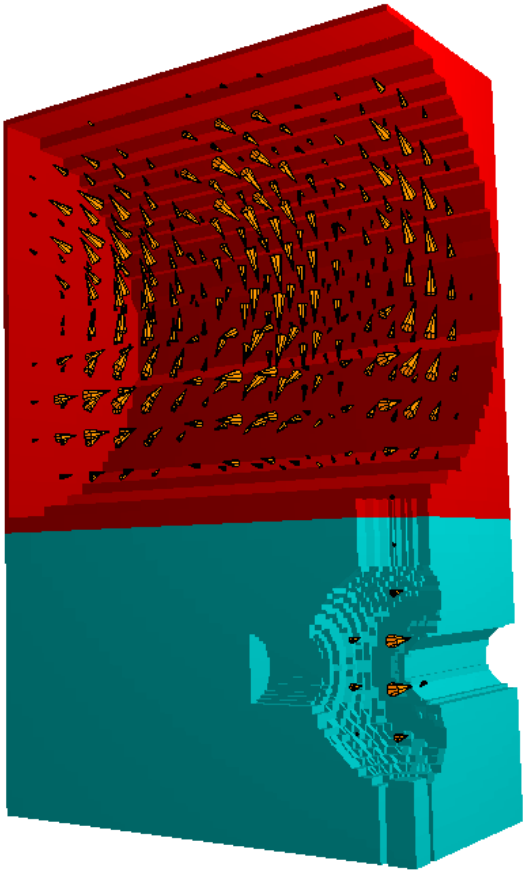

Figure 93. MAFIA model of one quarter of the geometry showing the electric field of the TE_{015} mode in the energy storage cavity and the TM_{010} mode in the accelerating cell.

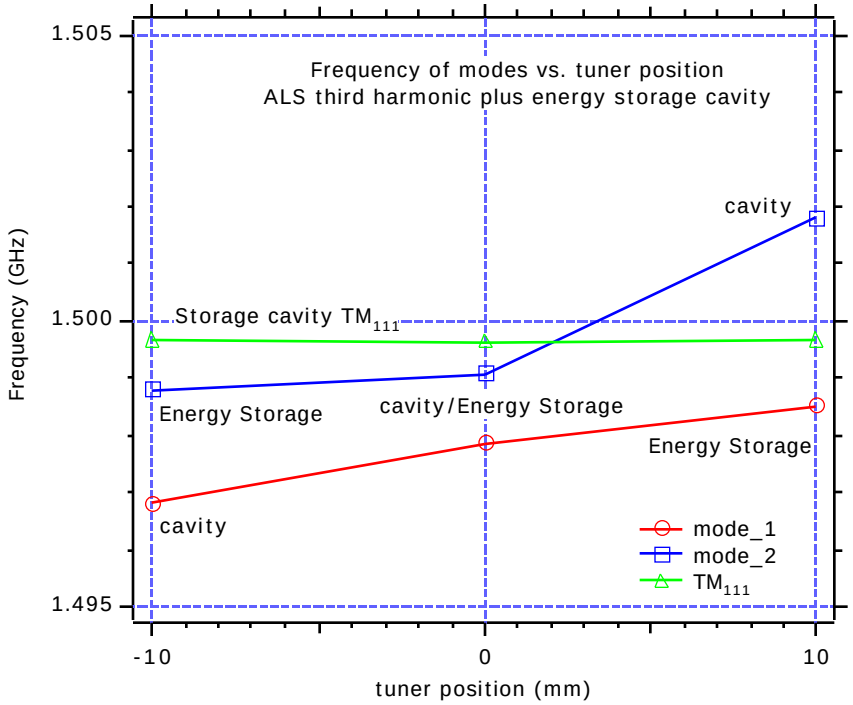

Figure 94. Variation of mode frequencies with tuner position. Labels show where the field is strongest in each branch.

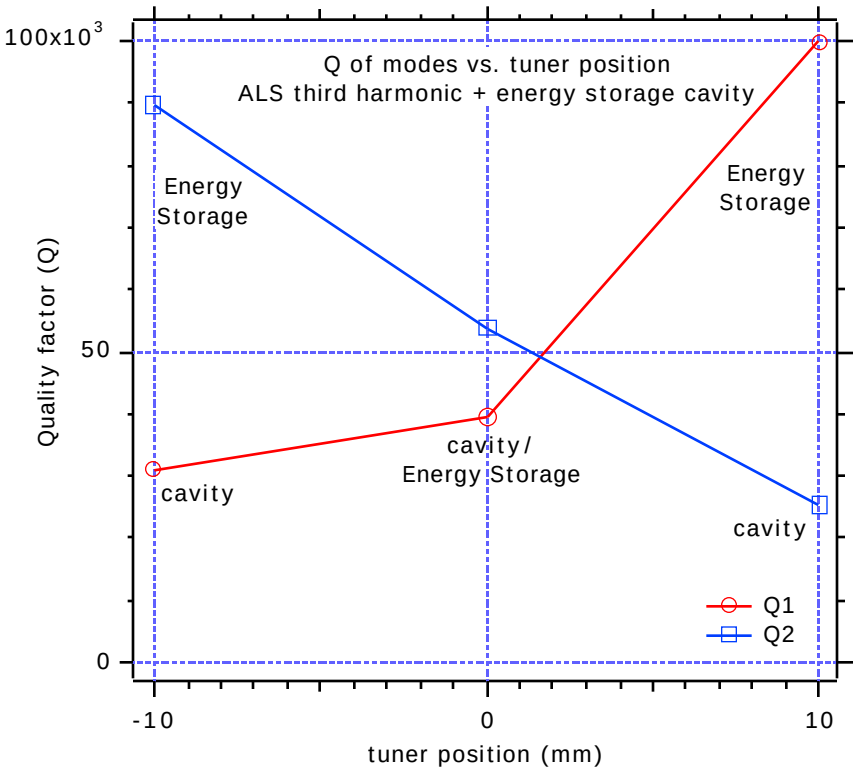

Figure 95. Variation of Q with tuner position. (positive displacement is into the cavity).

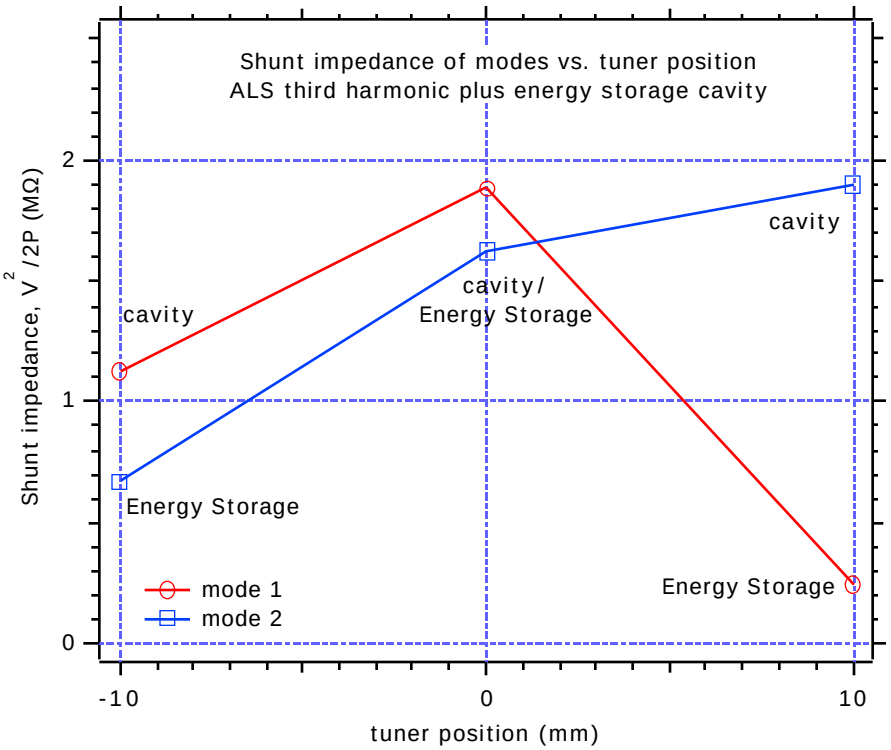

Figure 96. Variation of shunt impedance with tuner position.

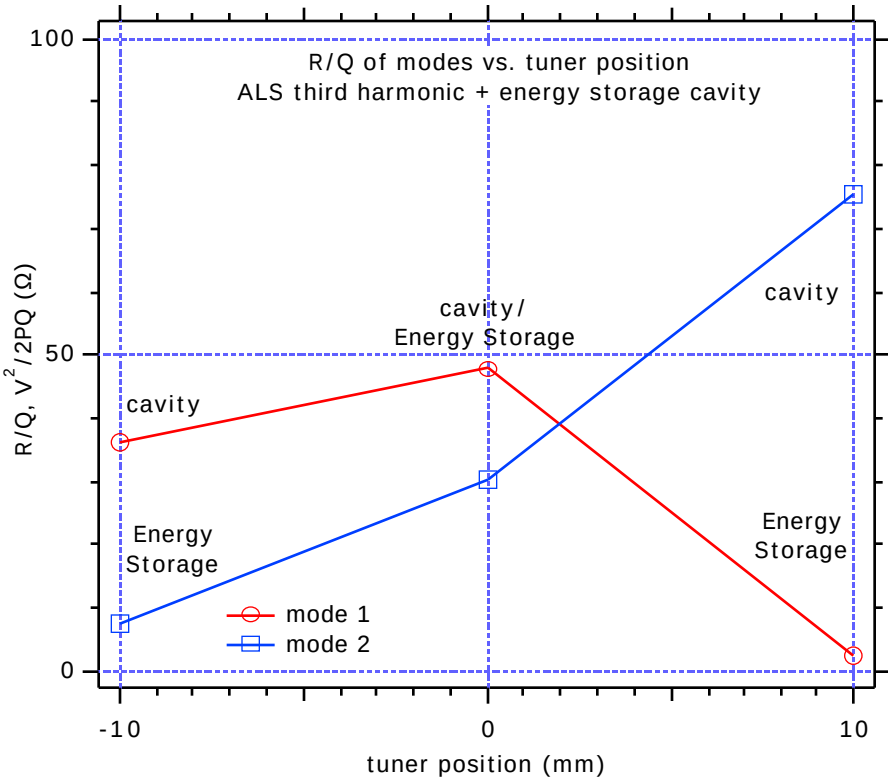

Figure 97. Variation of R/Q with tuner position.

7.2.2 Measurements on ALS third harmonic cavity

The measured Q of the storage cavity was about 80651 without any special surface preparation. The third harmonic cavity had a measured Qo of 14576. The coupled system, figure 98, showed an effective Q of 61583, more than a factor of 4 improvement over the basic cavity. The measured case in figure 99 probably corresponds to the simulation case with the tuner slightly withdrawn. The Q is about four times higher than the standard cavity and the shunt impedance would probably be about half, giving a factor of 8 lower R/Q. Time did not permit a bead-pull to verify this value.

Figure 98. ALS third harmonic cavity with energy storage cavity.

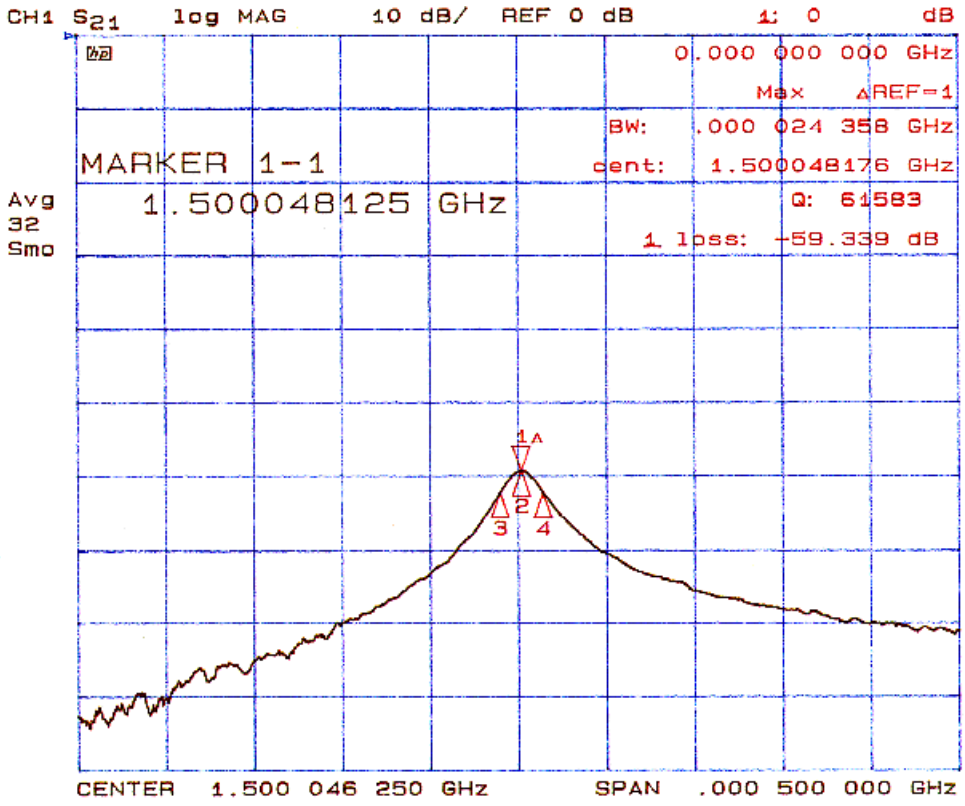

Figure 99. Measured Q with energy storage cavity (normally ~14500).

7.3 Superconducting option

This cavity type uses a negligible amount of RF power and can operate at higher voltage, requiring fewer cells. In practice the number of cavities would be limited by the window throughput. Given the state of the art in operating machines it would be prudent to use at least three cells in each ring so the window power would be less than or equal to one third of the 1 MW output of the klystron. A scaled Cornell type cavity could comfortably operate at the 1.13 MV required for the pre-damping ring or 500 kV of the damping rings. The lower R/Q would reduce the beam-induced gap transient by about a factor of 2.6 in the damping rings compared to the baseline design. The small number of superconducting cavities needed in the PDR would increase this to a factor of about six compared to the baseline design. The Cornell cavity shape has a typical peak magnetic field on the wall that is about a factor of 4 lower than the theoretical limit for pure niobium [14]. In our case the R/Q could be lowered until this limit was approached, further improving the transients at the cost of increased cryogenic losses. If the cavities are operated at less than typical voltage, as in our case, then the scope for

improvement would be even higher. An R/Q of 10 or lower should be achievable by these methods.

Figure 100 shows a MAFIA model of the elliptical single-cell cavity with a simplified "fluted" beam pipe on one side and a large circular bore on the other. The dimensions are scaled from the Cornell 500 MHz cavity. Figure 101 shows the trapped accelerating mode. Table 14 lists the basic parameters for this cavity. The MAFIA model was run in the time domain to get the broad band impedance spectra, figures 102 and 103. Both the longitudinal and transverse spectra are comfortably below threshold in all cases.

An interesting alternative might be to use a cornell-type cavity shape in copper. This would have good HOM properties and an R/Q about half the baseline design. The Qo calculated for copper by MAFIA is 37648 giving a shunt impedance of 1.69 MΩ. Allowing 80% of Qo for a realistic cavity gives 1.35 MΩ, requiring 92.5 kW for 500 kV, see table 15. This level of power dissipation could probably be handled with careful engineering.

Table 14. Parameters of superconducting Cornell-type cavity.

R/Q	44.5 Ω
Qo (est.)	1E9
Rs ($V^2/2P$)	44500 MΩ
V_{DR}	500 kV
P_{DR} (cryo)	2.8 W
V_{PDR} (3 cells)	1133 kV
P_{PDR} (cryo)	14.3 W

Table 15. Parameters of copper Cornell-type cavity.

R/Q	44.5 Ω
Qo (est.)	37648
Rs MAFIA,($V^2/2P$)	1.69 MΩ
Rs x 80%	1.35 MΩ
V	500 kV
P_{wall} (Cu)	92.5 kW

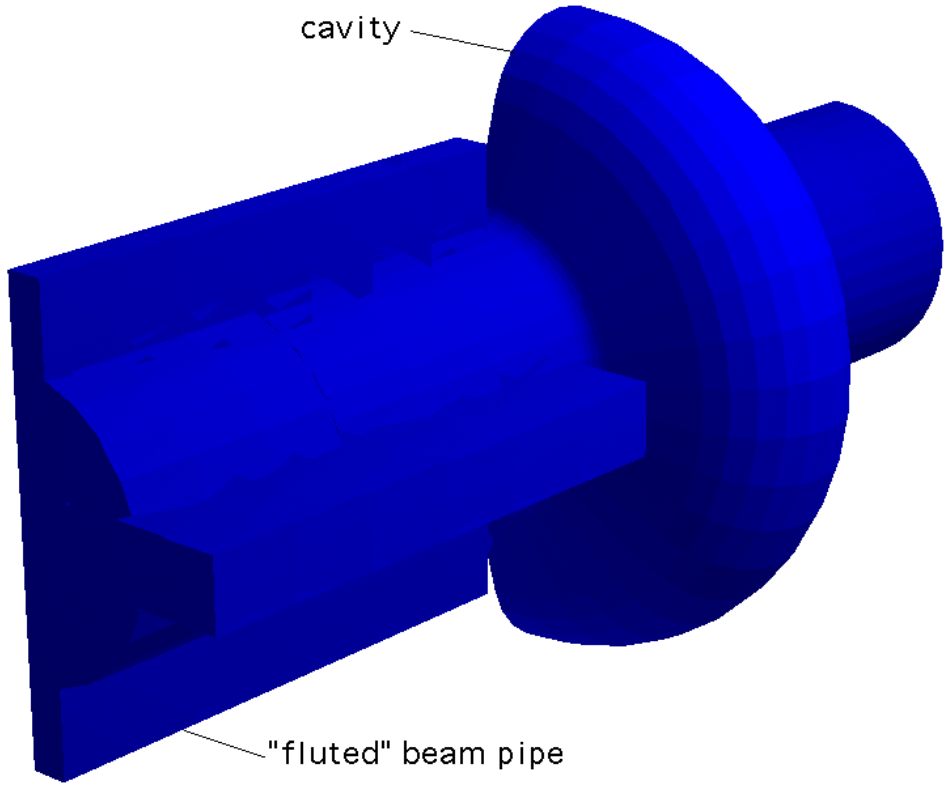

Figure 102. Model of Cornell-type cavity with "fluted" beam pipe.

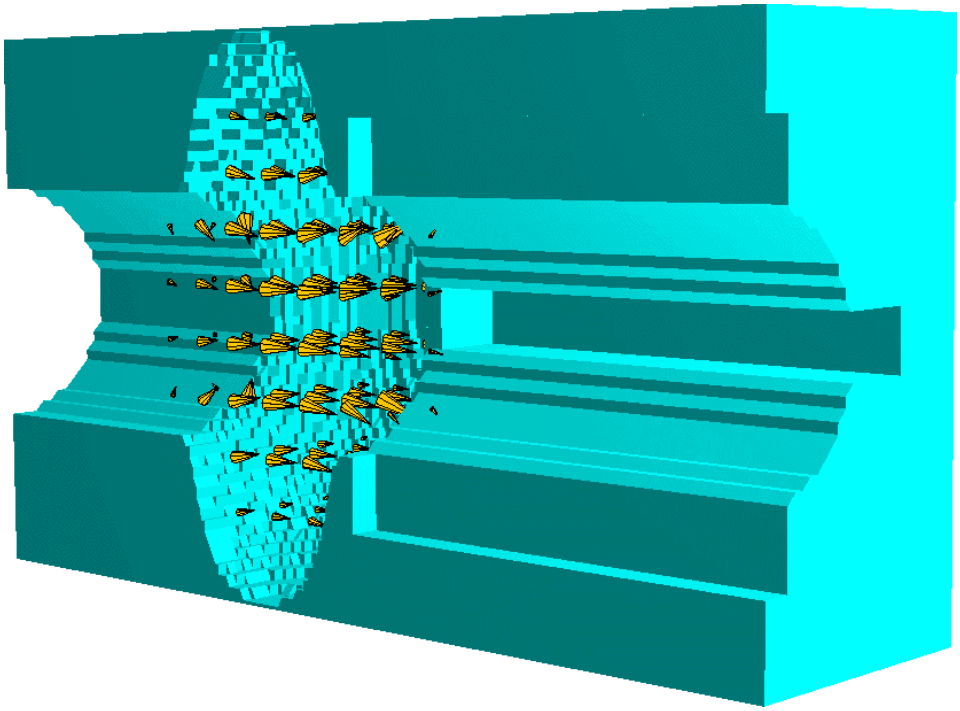

Figure 103. Fundamental mode.

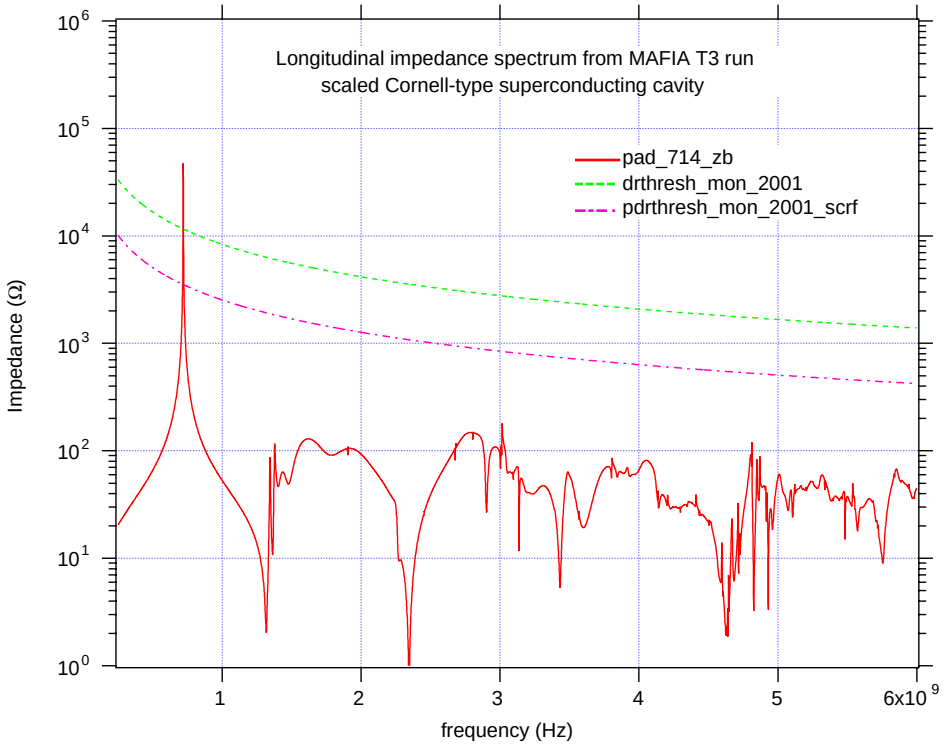

Figure 104. Longitudinal impedance of scaled Cornell-type SC cavity.

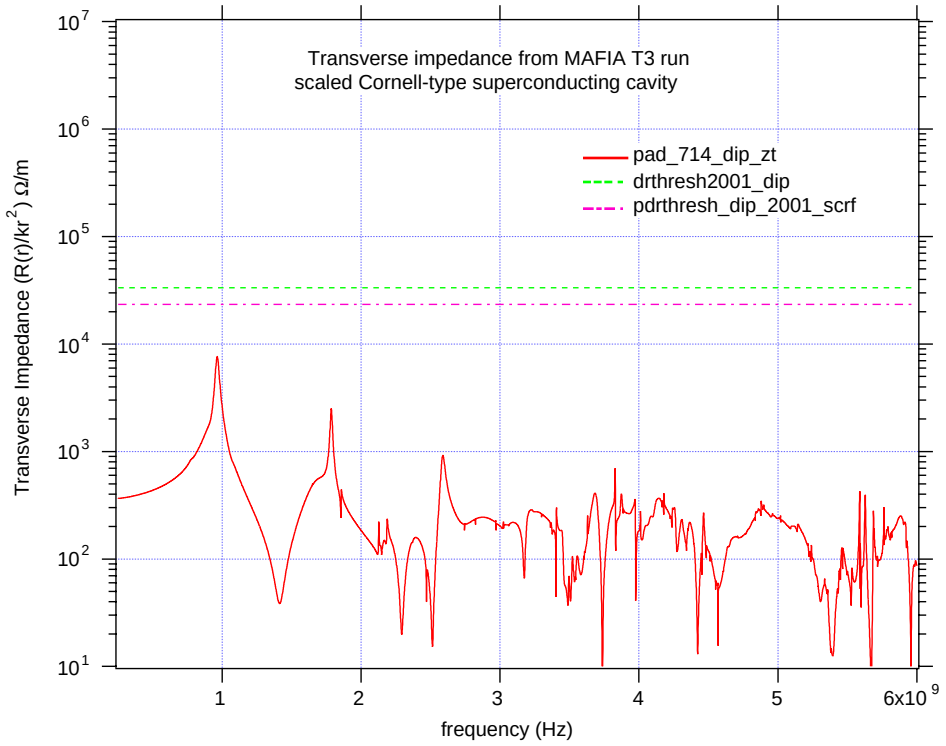

Figure 105. Transverse impedance of scaled Cornell-type SC cavity.

7.4 Future work

We have shown the feasibility of alternative cavity designs that offer still lower HOM impedances, increased stored energy or both. The current pre-damping ring voltage requirement has driven us to use a large number of cavities. Ongoing work on the predamping ring lattice is expected to reduce this in the future so the HOM impedance of the basic cavity should suffice. If for some reason this does not happen and the voltage required remains high then one of the low-HOM options may be advantageous. The alternative design with very large circular ports may offer the lowest HOM impedance of the normal-conducting options. It has only been studied briefly and is far from optimised. Variation of the beam pipe diameter and the addition of nosecones may increade the fundamental mode efficiency of this design.

Phase transients in the extracted beam can be reduced by increasing the stored energy in the cavity system. We have shown that a factor of 10 improvement is probably achievable, but at some cost. The external storage cavity appears to be the best option for increasing the stored energy of the copper system. If significant reduction in beam transients is required a full three-cavity system analysis should be performed.

If very low HOM impedance and increased stored energy are required a modified Cornell-type superconducting cavity system might be a possible solution. This low R/Q shape would be a departure from normal practice and would need to be investigated fully.

8 Conclusions

We have taken the conceptual design outlined in the first phase of the NLC damping ring study and developed it to the point where prototyping would now be possible. The cavity dimensions have been fine tuned by finite element analysis in ANSYS. The heat loads and thermal stresses are expected to be well within manageable limits and in fact below the operating conditions of the existing PEP-II cavities. The HOM impedance spectrum has been checked after frequency tuning and is within acceptable limits. The larger number of cavities in the pre-damping ring for the NLC-2001 parameter set may make the longitudinal impedance marginal, but this is expected to be corrected in the next iteration of the PDR lattice design. In any case options have been investigated for further reducing the HOM impedance if necessary. The HOM-driven transverse instability growth rates are small compared to the resistive wall modes.

Conceptual designs have been developed for all major ancillary components. The RF window design has been fully engineered and high power prototypes have been tested to more than double the required operating power. The coupling box is based on the proven PEP-II layout and has been matched in simulations by small capacitive bars in the waveguide. The HOM loads are based on the existing PEP-II concept with some simplifications. Simulations indicate good absorbtion over a very broad frequency range. The tuners are based on existing ALS and PEP-II experience and calculations show that spring fingers could be used to protect the bellows if necessary without incurring excessive RF currents.

Options for further reducing the HOM impedance or increasing the stored energy have been considered. Reduction of the beam-induced transients by an order of magnitude looks feasible, at some penalty in complexity or RF power.

The mechanical assembly of the baseline design is mostly the same as previously described. Appendix A shows an estimate of the costs, updated to include the higher number of cavities in the pre-damping ring.

The next stage in development of the RF cavity would be the construction of a prototype. In view of the detailed analysis already performed and of the similarity to the PEP-II design a cold model may not be necessary and a full power first article could be constructed.

9 References

[1] "RF cavity R&D at LBNL for the NLC Damping Rings, FY1999", R.A. Rimmer, J.N. Corlett, G. Koehler, D. Li, N. Hartman, J. Rasson, T. Saleh, CBP Tech Note 196, LCC-0033, November 1999.

[2] "Commissioning Results Of The KEKB And PEP-II B-Factories", J.T. Seeman, Proceedings of the 1999 Particle Accelerator Conference, New York, 1999.

[3] "DAΦNE Operating Experience", S. Guiducci, Proceedings of the 1999 Particle Accelerator Conference, New York, 1999.

[4] "A Third-Harmonic RF Cavity for the Advanced Light Source", R.A. Rimmer, EPAC98, Stockholm, Sweden.

[5] "Design Considerations for a Second Generation HOM-Damped RF Cavity", R. A. Rimmer, Proceedings of the 1999 Particle Accelerator Conference, New York, 1999.

[6] "Comparison of calculated, measured, and beam sampled impedances of a higher-order-mode-damped rf cavity", R.A. Rimmer, J.M. Byrd, and D. Li, Physical Review Special Topics - Accelerators and Beams, Vol. 3, 102001 (2000).

[7] "Coupled bunch instabilities in the NLC damping rings", S. De Santis, LCC-0069, May 2001.

[8] "PEP-II B-Factory Prototype Higher Order Mode Load Design", R. Pendleton et. al., Proc. PAC 95, Dallas, TX.

[9] "700 MHz Window R&D at LBNL", R. Rimmer et. al., 11/2000. LBNL-47939, CBP tech note 230.

[10] "A High-Power L-Band RF Window", R.A. Rimmer et. al., Proc. PAC 2001, Chicago., LBNL-47968, LAUR 01-2574., CBP note 384.

[11] "High-Power RF Window and Coupler Development for the PEP-II B Factory", M. Neubauer et. al., Proc. PAC 95, Dallas, TX, SLAC PUB 95-6894, LBNL-37250.

[12] "Development of a Movable Plunger Tuner for the High-Power RF cavity for the PEP-II B Factory", H. D. Schwarz et. al., Proc. PAC 97, Vancouver , Canada, 12-16 May, 1997, pp 3039-41. SLAC-PUB-7502.

[13] "KEKB B-factory design report", Toge, N.(ed.), KEK Report 95-7 Aug 1995, ch. 8.

[14] "RF Superconductivity for Accelerators" H. Padamsee, J. Knobloch, T. Hays, Wiley, New York, 1998.

Appendix A. Estimates of materials, fabrication, procurements and engineering.

Table A1 represents a preliminary estimate of the major components, operations and processes, based on the fabrication method outlined in [1] and a total of 13 cavities. The estimate is divided into separate sections for materials and procurements, lid and body machining (the two major components), integration and assembly, outsourced operations, and non-recurring costs. Note that these estimates do not include contingency. The total cost will depend on the hourly rate which will vary with location and vendor.

Table A2 shows a summary of approximate costs of PEP-II RF station equipment including cavity ancillary items such as windows, HOM loads and tuners. This equipment was constructed or purchased between 1994 and 1998 and costs are in "then-year" dollars. These costs, suitably adjusted, may be used as approximate guides for the NLC cavity ancillaries and RF station equipment until improved estimates are developed.

Table A1. Summary of preliminary estimates.

Estimate is based on 13 assembled cavities,	**$**	**Hours.**
Materials, Procurement	$251,228	
Lid Machining	TBD	2,662
Body Machining	TBD	2,527
Integration, Assembly	TBD	1,401
Outsourcing	TBD	6,000
NRE	TBD	3,912
Total		16,501

Table A2. Approximate cost of PEP-II RF station equipment . (Note: these items were constructed or purchased between 1994 and 1998).

Item	approx. cost per item (then year k$)
Klystron (Phillips, 1.2 MW)	335
Cavity	150
HOM loads (3 per cavity)	16
Coupler box (1 per cavity)	26
500 kW Window (1 per cavity)	24
Fixed tuner (1 per cavity)	3
Variable tuner (1 per cavity)	9
Raft (1 per cavity)	14
Circulator (AFT)	155
Waveguide network (per 4-cavity station)	68
Low-level RF (per 4-cavity station)	85
HV power supply	375
Cooling system (per 4-cavity station)	40
Cables (per 4-cavity station)	35
Misc., installation etc. (per 4-cavity station)	60